Numerical and experimental study of turbulent drop breakup in high--pressure homogenizers

Olad, Peyman

2024

Document Version:
Publisher's PDF, also known as Version of record

Numerical and experimental study of turbulent drop breakup in high-pressure homogenizers

Numerical and experimental study of turbulent drop breakup in high-pressure homogenizers

by Peyman Olad

LUND
UNIVERSITY

Thesis for the degree of Doctor of Philosophy
Thesis advisors: Assoc. Prof. Andreas Håkansson, Prof. Luca Brandt, Assoc. Prof. Maria Glantz, Prof. Fredrik Innings
Faculty opponent: Prof. Karsten Köhler

To be presented, with the permission of the Faculty of Engineering of Lund University, for public criticism in KC:A lecture hall at the Department of Food Technology, Engineering and Nutrition on Friday, the 19th of January 2024 at 9:00.

Organization
LUND UNIVERSITY

Department of Food Technology, Engineering and Nutrition
Box 124
SE–221 00, Lund, Sweden

Document name
DOCTORAL DISSERTATION

Date of disputation
2024-01-19

Sponsoring organization
Swedish research council (Vetenskapsrådet), Tetra Pak AB

Author(s)
Peyman Olad

Title and subtitle
Numerical and experimental study of turbulent drop breakup in high-pressure homogenizers

Abstract
Emulsification is the process of making stable mixture of two or more immiscible substances (typically oil and water). The product of this process, the emulsion, is found in various applications and industries such as food (milk and other dairy products, non-dairy alternatives, mayonnaise, salad dressing), cosmetics and pharmaceuticals (creams, lotions, intravenous medications), chemical (paints, cleaning products), etc. To have a stable mixture of the disperse phase (substance with lower volume fraction) inside the continuous phase (substance with higher volume fraction), one should use a third substance called an emulsifier. The emulsifier forms a layer around the disperse phase drops decreasing their tendency to coalesce with their neighbors. Furthermore, breaking the disperse phase into smaller drops increases the stability of the emulsion. The emulsifier decreases the energy needed for this breakup. High-pressure homogenizers (HPHs) are one of the most effective ways to create more stable emulsions through breaking the disperse phase drops.

Drop breakup mechanisms are still debated. But, the majority of the literature agrees on turbulence to be a dominating factor. Therefore, investigating the turbulence inside an HPH geometry is an essential step to improve the understanding of breakup mechanisms in these devices.

Investigations of the flow field and drop breakup phenomenon inside HPHs have been limited to experimental (PIV and drop visualizations) and CFD turbulence models. Direct numerical simulation (DNS) resolves the turbulence to the smallest scales (Kolmogorov-scales), providing information which none of the other tools are able to achieve. In this study, a simplified scale-up HPH geometry is designed to provide similar flow conditions as in a real HPH and DNS is performed on this geometry to describe flow field and turbulence properties to the smallest possible spatial and temporal scales. The results of industrially-favored CFD tools are also compared to the DNS results to provide best-practice recommendations.

Finally, drop breakup studies are carried out using experiments and numerical simulations and the results are compared. The validation of the numerical results through experiments provided the opportunity to use high-resolution data (particularly the dissipation rate of turbulent kinetic energy field as an important parameter in drop breakup) for further investigations on understanding turbulent drop breakup mechanisms.

Key words
High-pressure homogenizer (HPH), Turbulent drop breakup, Computational fluid dynamics (CFD), Direct numerical simulations (DNS), Experiments

Classification system and/or index terms (if any)

Supplementary bibliographical information

Language
English

ISSN and key title

ISBN
978-91-8096-016-8 (print)
978-91-8096-017-5 (pdf)

Recipient's notes

Number of pages
204

Price

Security classification

Signature _____ Date 18th December 2023

Numerical and experimental study of turbulent drop breakup in high-pressure homogenizers

by Peyman Olad

LUND
UNIVERSITY

A doctoral thesis at a university in Sweden takes either the form of a single, cohesive research study (monograph) or a summary of research papers (compilation thesis), which the doctoral student has written alone or together with one or several other author(s).

In the latter case the thesis consists of two parts. An introductory text puts the research work into context and summarizes the main points of the papers. Then, the research publications themselves are reproduced, together with a description of the individual contributions of the authors. The research papers may either have been already published or are manuscripts at various stages (in press, submitted, or in draft).

Cover illustration front: Illustration of the instantaneous streamwise velocity field (in the back), Q-critertion iso-surfaces colored by the streamwise velocity (in the middle), and different snapshots of the drop interface represented by VOF $= 0.5$ iso-surfaces (in the front), inside the outlet chamber of the high-pressure homogenizer scale-up model of this study.

Cover illustration back: Illustration of the trajectories and deformations of two drops (one numerical and one experimental drop) inside the outlet chamber of the high-pressure homogenizer scale-up model of this study. This picture represents the validation studies of the numerical simulations through the experiments (Adopted and modified from the graphical abstract for **Paper IV**).

Funding information: The thesis work was financially supported by Vetenskapsrådet and Tetra Pak AB.

Faculty of Engineering, Department of Food Technology, Engineering and Nutrition

ISBN: 978-91-8096-016-8 (print)
ISBN: 978-91-8096-017-5 (pdf)

Printed in Sweden by Media-Tryck, Lund University, Lund 2024

Dedicated to my parents
My dear sister, Elham
Love of my life, Hedieh

Contents

List of publications

This thesis is based on the following publications, referred to by their Roman numerals:

I **A direct numerical simulation investigation of the one-phase flow in a simplified emulsification device**
P. Olad, M. Crialesi Esposito, L. Brandt, F. Innings, A. Håkansson
Journal of Fluids Engineering 144 (8), 081209
https://doi.org/10.1115/1.4053896

II **Towards best practice recommendations for turbulence modelling of high-pressure homogenizer outlet chambers – Numerical validation using DNS data**
P. Olad, M. Crialesi Esposito, L. Brandt, F. Innings, A. Håkansson
Chemical Engineering Science 258, 117748
https://doi.org/10.1016/j.ces.2022.117748

III **Comparison of turbulent drop breakup in an emulsification device and homogeneous isotropic turbulence: Insights from numerical experiments**
P. Olad, F. Innings, M. Crialesi Esposito, L. Brandt, A. Håkansson
Colloids and Surfaces A: Physicochemical and Engineering Aspects 657, 130569
https://doi.org/10.1016/j.colsurfa.2022.130569

IV **Turbulent drop breakup in a simplified high-pressure homogenizer geometry: A comparison of experimental high-speed visualization and numerical experiments based on DNS and interface tracking**
P. Olad, F. Innings, A. Håkansson
Chemical Engineering Science 282, 119274
https://doi.org/10.1016/j.ces.2023.119274

V **Single drop turbulent breakup in the anisotropic turbulence inside a high-pressure homogenizer scale-up model**
P. Olad, A. Håkansson
Manuscript to be submitted

Publications not included in this thesis:

VI **Identification and Mapping of Three Distinct Breakup Morphologies in the Turbulent Inertial Regime of Emulsification—Effect of Weber Number and Viscosity Ratio**
A. Håkansson, **P. Olad**, F. Innings
Processes 10 (11), 2204
https://doi.org/10.3390/pr10112204

Acknowledgements

First, I would like to express my gratitude to my supervisor, Andreas Håkansson, who walked me through this journey. He was always there, offering a hand to help, keeping me on track but letting me test new things even though they might not have made much sense at the time. I would also like to pay my tribute to the late Fredrik Innings, whom I learned a lot from. Having the audacity to question the most basic notions and learning from it was one of the many things I admired in him. Also, I would like to thank Luca Brandt who was one of the reasons I started this journey. Meeting him nine years ago and seeing his energy in what he does made me more fond of fluid mechanics.

I am grateful to everyone at the department of food technology, engineering, and nutrition. Over the course of the past five years, many people have left and many others have joined the department. The list is very long, but I appreciate working alongside everyone I have met during these years.

I extend my thanks to Marco Crialesi Esposito and Marco Rosti for their support and help with the numerical studies. I would also like to thank Professor Karbstein's group in the food process engineering at Karlsruhe institute of technology, specially Eva Rütten, for providing the camera I used in the experimental studies. Special thanks to Dan Johansson, Rickard Terfelt, Alexander Taramanidis, Hans Bolinsson, and Olexandr Fedkiv for their help in setting up the experimental setup.

I am grateful of the friends I made during my time in Lund: Ali, Ashkan, Azin, Hesam, Ken, Mohammad Reza, Mostafa, Negin, Niloufar, Saeed, Shaghayegh, Shirin, Shiva, and many others who shared their time with me. I will always keep fond memories of the times we spent together.

I would not have been here without the unconditional support of my family: My parents, who always sacrificed their present for a better future for me. My brother, Iman, for always putting up with his little brother all these years, and his wife, Somayeh, for her kindness. My sweet nephew, Maneli. My aunt, Fariba, for being my last resort whenever I felt hopeless. My cousin, Mohammad, and her wife, Naghmeh, for their support and companionship, especially when I first moved to Sweden. My cousin, Masih, for the sweet memories from childhood to the backpacking trips we had together. Finally, for my role model, my dear sister, Elham, who was and will always be the strongest person I have ever seen in my life, and always supported me in whatever I did. Also, my heart goes to the memory of my dear Mamanjoon, my uncle, and my aunt who passed away during the writing of this thesis. My life will never be the same without them.

I also feel blessed to have another lovely and supportive family by my side: My dear Father- and mother-in-law; my sisters, Fereshteh, Elaheh, and Elham; my brothers, Amir, Mo-

hammad, Mehrbod, Alireza, and Mohammad Jr.; and the little ones, Kiarash and Karina.

I cannot put this into words, but I want to express how grateful I am to have the most considerate and supportive companion by my side: Hedieh. You amaze me everyday by your intelligence, maturity, and kindness. I wish I have the ability to cherish every moment I spend with you since, as you always say, that is all we have.

This study was financed by the Swedish Research council (VR), grant number 2018-03820 and Tetra Pak Processing Systems AB. The computations and data handling were enabled by resources provided by the National Academic Infrastructure for Supercomputing in Sweden (NAISS) at PDC and NSC, partially funded by the Swedish Research Council through grant agreement no. 2018-05973.

Popular science summary in English

Emulsification is the process of mixing two or more immiscible substances (typically liquids) to produce a stable mixture called an emulsion. Emulsions are ubiquitous in different products such as milk, mayonnaise, cosmetic creams and lotions, topical products, intravenous emulsions, paints, etc. The emulsification process affects the quality of the product in terms of texture and consistency, appearance, and taste.

An emulsion includes three main ingredients including two immiscible liquids which are usually oil and water and a surface active agent, called an emulsifier. Oil is almost non-soluble in water. Since the density of oil is less than water, the oil droplets tend to move toward the surface. This is due to the upward buoyancy forces exerted on oil droplets. The buoyancy force is directly related to the volume of the oil droplets. Therefore, the smaller the oil droplets, the smaller the buoyancy forces and therefore, the slower the movement of the oil droplets toward the surface. The accumulation of the oil on the surface is called creaming and is not generally favorable in the industry. To have a stable mixture i.e., emulsion, one should decrease the size of the oil droplets to delay the creaming process. In other words, the larger oil droplets should be broken into smaller droplets. High-pressure homogenizers are one of the most effective tools to achieve this.

The French inventor, Auguste Gaulin, presented one of the first successful homogenizer devices at the turn of the 20th century and the first "homogenized milk" was introduced at the World's Fair in Paris in 1900. Others tried to introduce new homogenizer machines in the following years, but almost all of them were based on Gaulin's main idea, even in the recent modern machines.

A pre-emulsion (oil and water mixture) is fed to the machine at a low pressure. The pressure of the mixture is increased to high pressures and the high-pressure flow of the mixture is forced through a narrow gap and then expands into a relatively large outlet chamber. This process leads to intense shear forces and turbulence to be exerted on the oil droplets, breaking them into smaller droplets.

What essentially happens during the homogenization process is using mechanical energy to break down the oil droplets into smaller fragments. But, how efficient this conversion of energy is handled is the big question in the world we live today where energy is expensive, either money-wise or in consideration of environmental impacts. From previous studies, we know that creating turbulence in the flow is an effective way of increasing the breakup efficiency of the droplets. But, we still lack the fundamental understanding of why and how the turbulence interacts with the droplets which leads to breakup. If we answer this question, then we can help the industry to design machines which provide the conditions for the maximum breakup efficiency, or in other words, saving energy, and with better control of emulsification processes, design better products.

In this thesis work, an enlarged (scale-up) model of a high-pressure homogenizer (HPH) was first designed to mimic the flow conditions in a real homogenizer. The scale-up process ensures that the physics of the problem do not change while increasing the sizes and decreasing the velocities compared to those in an industrial machine enable us to visualize the phenomenon inside the laboratory. In **Paper I**, the flow field and turbulent structures inside the HPH model were simulated and visualized with no modeling assumptions, also known as direct numerical simulation (DNS). This study provided a detailed understanding of the flow field behavior and turbulent properties. Due to high computational costs and therefore being time-consuming (needed 230 hours using 1000 CPUs to get a converged flow field), DNS is usually not preferred in the industry where reliable results are required within a reasonable time. Instead, turbulence models which decrease the number of required computations and therefore the computational time are used. **Paper II** presented the best-practice recommendations for industrial CFD of homogenization devices based on the unprecedented and unique validation data provided by the DNS.

Having the turbulent flow field ready, it was time to inject the drops and investigate their breakup characteristics. This was investigated in **Paper IV** in two ways: i) Experiments, where the images of the drops were captured through high-speed photography and then the images were processed to analyze the breakup events, and ii) Numerical simulations where the governing equations of the flow and drop interface were resolved to the smallest relevant scales. The results obtained from the two approaches were used complementarily. The resolution of the data obtained through numerical simulations cannot be obtained through any experiments i.e., the flow field information such as velocity are obtained at positions with microscopic distances. However, numerical simulations always need validations through experiments. To the best of the author's knowledge, this was the first study comparing high-speed breakup experiments and numerical drop breakup simulations under the same setting. As a result of this validation, the vast information provided by the numerical simulations were used for further analyses of the impact of the flow field on the drop breakup. Such an information in an industrially relevant emulsification device is unprecedented and is of great value. The findings of these investigations are found in **Paper V**.

Paper III, provided an insight into the similarities and differences of the breakup of drops in ideal turbulent conditions (which is not usually the case in an industrial application) and the real turbulent field in the HPH model. The majority of researches in the literature on the drop breakup are focused on ideal turbulent conditions. This comparison study provided information on how much of the previous knowledge of breakup in ideal conditions is extendable to the conditions closer to real industrial setups.

Populärvetenskaplig sammanfattning på svenska

Emulgering är processen där två eller fler oblandbara ämnen (vanligtvis vätskor) blandas för att producera en stabil dispersion, en så kallad emulsion. Emulsioner finns överallt runt omkring oss i produkter så som mjölk, majonnäs, kosmetiska krämer och lotioner, samt i intravenösa emulsioner och färger med mera. Emulgeringsprocessen är viktig för att få rätt kvalitet på dessa produkter – exempelvis i form av konsistens, utseende och smak.

En emulsion innehåller tre huvudingredienser. Förutom de två oblandbara vätskorna – vanligtvis olja och vatten – ett ytaktivt medel, kallad emulgator. Oljan är nästan olöslig i vatten. Eftersom oljans densitet är lägre än vattnets, tenderar oljedropparna att röra sig upp mot ytan. Detta beror på de lyftkrafterna som vätskan utöver på oljedropparna. Lyftkraften beror på oljedropparnas volym. Därför kommer dropparna att röra sig långsammare mot ytan ju mindre de är. Ansamlingen av oljan på ytan av en emulsion kallas gräddsättning och är generellt sett något man vill undvika. För att få en stabil blandning, det vill säga för att få en stabil emulsion, vill man därför minska storleken på oljedropparna för att därigenom fördröja gräddsättningen. Med andra ord vill man bryta upp de större oljedropparna. Högtryckshomogenisatorer är ett av de mest effektiva verktygen för att uppnå detta industriellt.

Den franske uppfinnaren, Auguste Gaulin, presenterade en av de första framgångsrika homogeniseringsanordningarna vid 1900-talets början. Med denna introducerade Gaulin den första 'homogeniserade mjölken' på världsutställningen i Paris 1900. Andra har försökt introducera nya homogeniseringsmaskiner, men i huvudsak bygger de på Gaulins idé: En föremulsion (en grov blandning av olja och vatten) matas till maskinen. Trycket ökas med en pump. Föremulsionen tvingas därmed genom en smal spalt. Efter spalten expanderar flödet ut i en stor utloppskammare. Denna process ger upphov till intensiva skjuvkrafter och turbulens, vilket bryter upp oljedroppen i mindre fragment.

Det som sker i homogenisatorn är således att mekanisk energi bryter ner oljedropparna. Men detta kan göras med olika effektivitet. Och hur detta kan göras mer effektivt är en viktig fråga, inte minst i en värld med höga energipriser och stor oro över hur vi ska åstadkomma en miljömässigt hållbar produktion. Från tidigare studier är det välkänt att turbulens kan vara en effektiv metod att bryta sönder droppar. Men vi saknar fortfarande den grundläggande förståelsen för hur turbulensen interagerar med dropparna i homogenisatorn, och hur detta leder till uppbrytning. Genom att bättre besvara den frågan kan vi hjälpa industrin att designa maskiner som ger förutsättningar för maximal uppbrytningseffektivitet, eller med andra ord, spara energi. Samtidigt hoppas vi då också bättre kunna kontrollera emulgeringsprocessen vilket ger oss möjligheter att designa produkter med högre kvalitet.

I denna avhandling utvecklades först en uppskalad modell av en högtryckshomogenisator. Målet var att så bra som möjligt efterlikna flödesförhållandena i en industriellt relevant

apparat. Genom ett systematiskt uppskalningsarbete försäkrar vi oss om att det är samma fysik i modellen. Samtidigt blir hastigheterna lägre vilket möjliggör för oss att filma uppbrytningsförloppet med en höghastighetskamera. I första artikeln (**I**) simulerades och visualiserades modellens flödesfält, med särskild fokus på turbulenta strukturer. Här användes en så kallad direkt numerisk simulering (DNS), en metod som inte kräver några modelleringsantaganden. Genom denna studie fick vi en detaljerad förståelse av flödesfältet och turbulensen i modellen. Men metoden är mycket beräkningsintensiv – det krävdes exempelvis 230 timmar med 1000 processorer för att få ett konvergerat flödesfält. Därför används DNS sällan för tillämpade eller industriella flöden. I stället används vanligen turbulensmodeller. Dessa minskar antalet nödvändiga beräkningar och därmed beräkningstiden. I artikel **II** jämfördes den mer rigorösa DNS-metoden med de i industrin mer vanligt förekommande metoderna. Jämförelsen användes för att ta fram rekommendationerna för hur industriella flödesberäkningar (CFD) bör göras på homogenisatorer. Detta är den första sådana valideringen av homogenisatormodeller och den bygger det unika datamaterialet som erhölls i DNS-beräkningen.

Med det turbulenta flödesfältet på plats var det dags att injicera oljedroppar och undersöka hur de bryts upp i turbulensen. Detta rapporteras i artikel **IV**. Två metoder användes: i) experiment, där en höghastighetskamera och bildanalys användes för att fånga skarpa bilder av dropparna, och ii) numeriska simuleringar där uppbrytningen simulerades genom att lösa de grundläggande ekvationerna som beskriver hur turbulenta flöden och gränsytor påverkar varandra, ner till de minsta relevanta längd- och tidsskalorna. Både metoderna behövs. De numeriska simuleringarna har unika fördelar, såsom att både flödesfältet och droppens yta beskrivs ner till mikrometernivån. Samtidigt behöver simuleringar alltid valideras experimentellt. Så vitt vi känner till är detta första gången som en studie jämför experimentella undersökningar av droppuppbrytning med numeriska simuleringar i samma uppställning.

Efter genomförd validering kunde vi också använda informationen from de numeriska simuleringarna för ytterligare analyser av hur flödesfältet påverkar droppuppdelningen. Detta har inte gjorts tidigare och har ett stort värde för ökad förståelse och framtida utveckling av emulgeringsmaskiner. Resultatet av dessa undersökningar presenteras i artikel **V**.

Artikel **III**, gav en inblick i likheter och skillnaderna mellan droppuppbrytning i mer idealiserade turbulenta flöden (ofta studerat men vanligen inte fallet i industriella tillämpningar) och det verkliga turbulenta fältet i en homogenisator. Majoriteten av den tidigare forskningen om droppuppbrytning är inriktad på idealiserade turbulenta förhållanden. Den här jämförande studien gav information om hur mycket av den tidigare kunskapen om droppuppbrytning under idealiserade förhållanden som går att överföra till mer realistiska industriella förhållanden.

Nomenclature

Abbreviations

CFD	Computational fluid dynamics
DNS	Direct numerical simulation
HIT	Homogeneous isotropic turbulence
HPH	High-pressure homogenizer
LES	Large-eddy simulation
Num	Numerical study
PBE	Population balance equation
PIV	Particle image velocimetry
RANS	Reynolds-averaged Navier-Stokes
TI	Turbulent inertial
TKE	Turbulent kinetic energy
TV	Turbulent viscous
VOF	Volume of fluid

Symbols

Latin

A	Drop interfacial area [m^2]
A_0	Initial drop interfacial area [m^2]
C	Circularity [-]
C_f	Skin friction coefficient [-]
Ca	Capillary number [-]
D	Drop diameter [m]
D_0	Initial drop diameter [m]
D_H	Hydraulic diameter [m]
d_H	Hinze drop diameter [m]
$E(\kappa)$	Energy spectrum function [J]
f	Frame number [-]
f_i	Body force vector [N]
F_i	Interfacial tension force [N]
$G(\mathbf{r}, \mathbf{x})$	LES filter [-]
H	Color function [-]
h	Gap height [m]
k	Turbulent kinetic energy [m^2/s^2]
k_r	Residual kinetic energy [m^2/s^2]
l	Eddy length-scale [m]
l_g	Gap length [m]
L_t	Integral length-scale [m]
L_x	Channel length in streamwise direction [m]
N	Number of drops [-]
N_c	Number of cells at the inlet (vortex method) [-]
n_i	Normal vector [-]
p	pressure [Pa]
P	Perimeter of drop [m]
P_f	Perimeter of drop at frame f [m]
Q	Volume flow rate [m^3/s]
Re	Reynolds number [-]
Re_d	Drop Reynolds number [-]

Re_{D_h}	Reynolds number based on hydraulic diameter [-]
S	Jet spreading rate [-]
$\langle S_{ij} \rangle$	Mean rate of strain tensor [s^{-1}]
t	Time [s]
T_{TI}	Turbulent interial regime time-scale ratio [-]
T_{TV}	Turbulent viscous regime time-scale ratio [-]
t_g	Gap time-scale [s]
t_{pass}	Passage time [s]
U_x	Streamwise velocity component [m/s]
u_i	Velocity vector [m/s]
u_i'	Velocity fluctuation vector [m/s]
u_{rms}'	Velocity fluctuations root-mean-square [m/s]
U_g	Gap bulk velocity [m/s]
u_τ	shear velocity [m/s]
We	Weber number [-]
$We_{s_{max}}$	Local maximum Weber number of the drop surface [-]
$y_{1/2}$	Jet half-velocity width [m]
x, y, z	Spatial dimensions [m]
x_i	Spatial coordinate i [m]
$x_{breakup}$	Drop centroid position at the time of initial breakup [m]
x_{C_n}	Drop centroid position at circularity level n [m]
Greek	
δ	1D delta function [-]
δ_{99}	Boundary layer thickness [m]
δ_{ij}	Dirac delta function [-]
γ	Interfacial tension [N/m]
ε	Dissipation rate of turbulent kinetic energy [m^2/s^3]
$\varepsilon_{s_{max}}$	Local maximum dissipation rate of turbulent kinetic energy on the drop surface [m^2/s^3]
η	Kolmogorov length-scale [m]
κ	wavenumber [m^{-1}]
κ_d	Curvature [m^{-1}]
κ_{LES}	LES filter cut-off wavenumber [m^{-1}]
μ	Mixture dynamic viscosity [Pa.s]
μ_c	Continuous phase dynamic viscosity [Pa.s]
μ_d	Disperse phase dynamic viscosity [Pa.s]
ν_c	Continuous phase kinematic viscosity [m^2/s]
ρ	Mixture density [kg/m^3]
ρ_c	Continuous phase density [kg/m^3]
ρ_d	Disperse phase density [kg/m^3]
σ	External stress [Pa]
σ_{stab}	Drop internal stabilizing stress [Pa]
τ_{def}	Drop deformation time-scale [s]
τ_{eddy}	Eddy lifetime scale [s]
τ_{ij}^R	Isotropic residual stress tensor [Pa]
τ_{ij}^r	Anisotropic residual stress tensor [Pa]
τ_{wall}	Wall shear stress [Pa]
τ_η	Kolmogorov time-scale [s]
ϕ	Volume of fluid function [-]
ψ	Generic variable
ω	Vorticity [s^{-1}]

Chapter 1

1 Introduction

1.1 Background

An emulsion is a dispersion of two or more immiscible liquids, such as oil and water where one substance is dispersed in the form of small droplets i.e., the disperse phase, within the other substance i.e., the continuous phase. Another substance, called the emulsifier is usually used as the emulsifying agent to reduce the interfacial tension between the two phases and facilitate the formation of a stable emulsion. The instability comes from the fact that the drops of each phase tend to coalesce with their neighbors leading to the separation of the phases (McClements, 2016). As the disperse phase usually has a lower density than that of the continuous phase, it tends to move upward to the surface. This phenomenon is called creaming which is not favorable in many applications. The rate at which the creaming occurs depends on the size of the disperse phase drops besides the density (which is a material property). Therefore, reducing the size of the drops is the solution to delay creaming. High-pressure homogenizers are an effective way to achieve this.

Homogenization process as a method for making stable emulsions was introduced and patented at the turn of the 20th century by Auguste Gaulin. The specific product of interest at that time was milk. As the arrival of industrial sterilization made it possible to transport milk over long distances, it seemed necessary to delay the creaming of milk. Gaulin introduced the first high-pressure homogenizer (HPH) which was basically a 3-piston pump and a series of capillary tubes mixing the flow of milk. This simple idea introduced the concept of industrial emulsification leading to increased shelf-life of dairy products as well as the smoothness of the final products. The first milk treated by Gaulin's machine was introduced at the World's Fair in Paris in 1900 and was called "homogenized milk" (Trout, 1950). Through the years, various homogenizer machines were introduced and patented, but they were generally based on Gaulin's basic concept.

In principle, the HPH consists of a piston pump connected to a valve. The HPH valve, as

schematically illustrated in Fig. 1.1, consists of an inlet chamber (converging at the end), a narrow gap (the space between the seat and the forcer), and an outlet chamber. The idea is to pump the pressurized disperse phase (or a mixture of the disperse and continuous phases) with pressures depending on the application e.g., typically in the range $3-20$ MPa, through the narrow gap, with typical heights $15-300\mu m$ (McClements, 2016; Rayner and Dejmek, 2015), leading to the breakup of the disperse phase droplets and efficient mixing in the continuous phase inside the outlet chamber. The typical flow rates in industrial applications vary between $100-20000$ l/h where the velocity of the emulsion flow is typically in the range $100-400$ m/s (Bylund, 2003) and could increase as high as 2000 m/s inside the gap (Rayner and Dejmek, 2015).

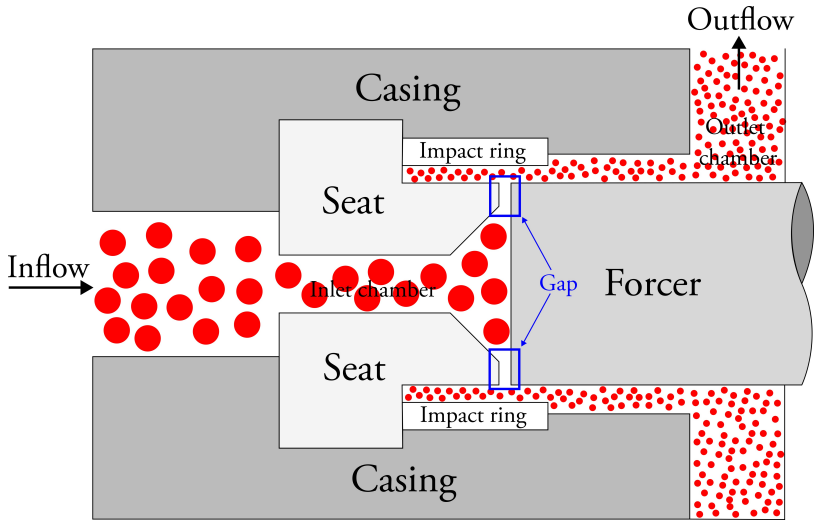

Figure 1.1: Schematic illustration of a typical high-pressure homogenizer valve

In the emulsification process, the disperse phase drops go through both breakup and coalescence events (Lobo et al., 2002; Narsimhan and Goel, 2001; Taisne et al., 1996). Tcholakova et al. (2004, 2008) proposed that the effect of coalescence in the emulsification process is dominant if the emulsifier concentration is lower than a critical value which depends on the drops surface load of the emulsifier and the volume fraction of the drops (the disperse phase). Therefore, given a very low fraction of the disperse phase (oil) and sufficient amount of emulsifier (both of which are ensured in this work), the chance of coalescence of oil drops could be effectively minimized. Consequently, breakup is often considered as the dominating mechanism which is why we focus on it in this work.

Turbulence is characterized by chaotic fluctuations in the pressure and velocity fields (Pope, 2000). In a turbulent flow regime, inertial forces are dominant over the viscous forces. The ratio of the two is defined as the Reynolds number (Re) and is a measure of the degree of turbulence in the flow.

The exact mechanism of emulsion drop breakup is disputed among researchers. Kolmogorov (1949) and Hinze (1955) attempted to describe the underlying mechanisms of drop breakup. A general conclusion of their work was that a drop breaks up when the external destabilizing stresses acting on its surface (the interface between the disperse and continuous phases) are sufficiently large to overcome the internal stabilizing stresses i.e., Laplace pressure. Walstra (1993) suggested that two dimensionless numbers could provide clues on such an information: i) Weber number defined as the ratio of turbulent inertial stresses, and ii) Capillary number defined as the ratio of turbulent viscous stresses to the internal Laplace pressure. Based on their definitions, a critical value, measured empirically, should exist for both of these numbers above which breakup events occur. This provided a theoretical estimation of the largest drop size which could survive under sufficiently long exposure to the turbulent field.

As a conclusion, two main breakup regimes called turbulent inertial (TI) and turbulent viscous (TV) are often considered as the main breakup mechanisms in a turbulent flow setup (Walstra, 1993). Based on Kolmogorov-Hinze theory, it is usually assumed that one of these regimes is the dominant mechanism while the other could be neglected (Vankova et al., 2007). Eddies with sizes comparable to the drop and smaller are responsible for TI and eddies larger than the drop are responsible for the TV breakup mechanism. Hinze drop diameter (d_H) is usually used as a parameter to distinguish between the two breakup regimes which is defined as follows:

$$d_H = \varepsilon^{-2/5} \gamma^{3/5} \rho_d^{-3/5} \tag{1.1}$$

where ε is the dissipation rate of turbulent kinetic energy, γ is the interfacial tension, and ρ_d is the disperse phase (oil drop) density. if $d_H > \eta$, TI is considered as the dominant breakup regime. Otherwise, TV is the dominant breakup regime (Håkansson, 2021a; Vankova et al., 2007). More details are discussed in section 2.1. However, a wide range of length scales are present in the highly anisotropic turbulent flow inside an HPH outlet chamber (Håkansson et al., 2011; Innings and Trägårdh, 2007) and therefore, a combination of both mechanisms is usually responsible.

Other mechanisms are also proposed in the literature as potential causes of breakup. Loo et al. (1950) was one of the first proponents of cavitation as an effective breakup mechanism in high-pressure homogenizers. They claimed superior mechanical efficiency of an HPH valve modified to produce cavitation during the homogenization compared to a regular valve. However, more recent studies oppose this claim. Gothsch et al. (2016) reported no contribution by cavitation in the emulsification process inside a high-pressure microsystem consisting of an orifice geometry. They even claimed that cavitation might result in worse emulsification efficacy. Schlender et al. (2015) reported worse efficiencies of the emulsification process in the presence of intense cavitation. They proposed that efficient emulsifica-

tion is achieved provided that no coherent vapor pockets are present in the outlet chamber. The experiments of Preiss et al. (2022) also reported smaller median size for the drops in the absence of cavitation compared to the case of intense cavitation. However, they also reported a tendency of larger drops and further downstream breakup positions even for the cases at the inception of cavitation compared to no cavitation flow.

In the context of high-pressure homogenizers, there is a general consensus in the literature, that breakup is mainly caused by turbulent interactions (Budde et al., 2002; Galinat et al., 2005; Kelemen et al., 2015b; Innings and Trägårdh, 2005; Stang et al., 2001). Innings et al. (2011) showed that the breakup of the drops only occurs in highly turbulent regions downstream of the gap exit i.e. inside the outlet chamber. Therefore, the focus in this thesis work is mainly on the turbulent breakup inside the HPH outlet chamber.

Furthermore, as the majority of the studies in the literature on the turbulent breakup phenomenon is based on ideal turbulence conditions i.e., homogeneous isotropic turbulence (HIT), the highly anisotropic turbulence in a high-pressure homogenizer outlet chamber adds more complexity to the understanding of the breakup mechanisms in such complex flows. Therefore, a more detailed investigation of the flow field and its impact on the drops deformation and breakup is needed for a better understanding of the breakup mechanisms. This is the main objective of this thesis work.

1.2 State-of-the-art evolution

The study of drop breakup inside a high-pressure homogenizer outlet chamber requires two main steps. First, we need to understand the hydrodynamics i.e., flow field characteristics, inside the HPH outlet chamber. Then, we need to study the impact the turbulent flow field has on the drop and how the drop responds to that impact.

This section provides a brief review of the state-of-the-art evolution in studying the hydrodynamics of HPH geometries (section 1.2.1) as well as turbulent drop breakup phenomenon (section 1.2.2) before the contributions made in this thesis work.

1.2.1 HPH hydrodynamics

The early interests in characterizing the flow field in an HPH geometry began in 1990s. Interestingly, CFD (Computational Fluid Dynamics), RANS (Reynolds-averaged Navier-Stokes) to be more specific, was one the the first tools to do so. This was mainly due to the limitations regarding the geometry and high velocities which made it difficult to investigate the flow field inside an HPH valve through experimental approaches. Kleinig and Middelberg (1996, 1997) used a standard $k-\varepsilon$ turbulence model to simulate the flow in

the inlet chamber, gap, and outlet chamber of a homogenizer valve. During the years, many others continued using RANS for describing the HPH flow field (Floury et al., 2004; Kelly and Muske, 2004; Miller et al., 2002; Steiner et al., 2006; Stevenson and Chen, 1997). Mainly in the late 2000s, researchers started incorporating population balance equation (PBE) into RANS to model drop breakup and predict size distributions (Becker et al., 2014; Casoli et al., 2010; Dubbelboer et al., 2014; Guan et al., 2020; Håkansson et al., 2013; Jiang et al., 2019; Köhler et al., 2008; Pang and Ngaile, 2021; Raikar et al., 2010).

However, RANS turbulence models are known for their limitations in more complex flow fields, particularly with curved streamlines (Pope, 2000) which is a typical characteristic of the HPH outlet chamber flow field. Therefore, researchers started looking for more reliable approaches to validate the results obtained by RANS. There were two main approaches to be used: i) Experiments, mainly through particle image velocimetry (PIV), and ii) high-fidelity numerical methods such as large eddy simulation (LES) and direct numerical simulation (DNS). A number of studies in both approaches will be discussed in the following paragraphs.

Innings and Trägårdh (2007) carried out one of the first experimental studies on characterizing the flow inside an HPH valve geometry. The velocity fields and turbulent properties of the flow were analyzed and described in an HPH scale-up model using 2D-PIV. They also provided an estimation of the characteristic dissipation rate of turbulent kinetic energy (TKE) which is an important parameter in drop breakup studies.

Håkansson et al. (2011) used high-resolution 2D-PIV to study the flow characteristics inside the HPH scale-up model which allowed more accurate calculation of Reynolds stresses and dissipation rate of TKE fields which the latter was only predicted before through rough global estimations (Innings and Trägårdh, 2007; Mohr, 1987). Håkansson et al. (2012) then used the experimental results to validate RANS models simulations. The results showed that RANS was able to predict the first-order statistics (e.g., velocities) by reasonable errors, but when it comes to turbulent properties e.g., TKE and its production rate, RANS is not a reliable approach. During subsequent years, more experimental studies have been carried out on the characterization of flow fields in HPH-like geometries (Kelemen et al., 2015b; Preiss et al., 2021).

But, the implications of the breakup theories regarding the importance of smaller scales (both spatial and temporal), comparable to those of the drops, and the advances in computational capacities of the modern computers convinced the researchers to employ more high-resolution numerical simulations. Taghinia et al. (2016) continued the PIV validations of Håkansson et al. (2012) using LES and a hybrid LES-RANS model and reported better predictions of the velocity and shear stress fields using LES. Bagkeris et al. (2020) also reported a good agreement of LES and PIV data on a sonolator HPH.

However, LES only resolves the larger scales of the flow and model the smaller scale struc-

tures. Those small scales (with sizes comparable to the drop, down to the lowest scales i.e., Kolmogorov-scales) are the most relevant for investigating the single drop breakup investigations (Andersson and Andersson, 2006a; Innings and Trägårdh, 2007; Karimi and Andersson, 2018) and therefore should be fully resolved. The only remaining solution would be DNS. Such a flow field resolution cannot be achieved by any experimental technique either. This thesis work is the first DNS study on an HPH geometry as an essential emulsification device in the industry.

1.2.2 Drop breakup

Kolmogorov-Hinze theory is still viewed as the basis for understanding drop breakup mechanisms. During the years, others have tried to expand this theory. Davies (1985) and Calabrese et al. (1986) suggested an extra internal stabilizing factor in addition to the Laplace pressure. They proposed that at higher viscosities of the disperse phase, rotational flows are induced inside the drops as a result of the external stresses which lead to more resistance to deformations. This introduced an extension to the original Kolmogorov-Hinze theory of breakup.

The intermittency of turbulence is another characteristic of the flow field which is not accounted for in the classic Kolmogorov-Hinze theory. Studies (Baldyga and Podgórska, 1998; Håkansson, 2021b) show that the stochastic variations in the flow field could result in considerable fluctuations in turbulent properties such as the dissipation rate of turbulent kinetic energy in different periods of times at a specific location which in turn results in quite different stress histories which different drops experience as they move through the same geometry. Attempts have been made to incorporate this phenomenon into the classic theory of Kolmogorov-Hinze. Walstra and Smulders (1998) proposed an additional condition for the prediction of breakup (in addition to the condition of time-averaged external stresses exceeding the internal stabilizing stresses i.e., $\overline{\sigma} > \sigma_{stab}$). They suggested that the eddy-drop interaction time ($\tau_{eddy} \propto D^{2/3}\varepsilon^{-1/3}$) should also exceed the time needed for the drop deformation ($\tau_{def} \propto \frac{\mu_d}{\sigma}$). Other corrections and modifications are also proposed by others (Andersson and Andersson, 2006a; Baldyga and Podgórska, 1998; Håkansson et al., 2017).

The classic Kolmogorov-Hinze breakup mechanism was essentially a result of the forces balance on the drop interface where sufficiently intense eddies deformed the drop to the point of breakup. Risso and Fabre (1998) proposed an additional mechanism where mechanical resonance is suggested to be another contributing factor leading to breakup. They proposed that if the damping time of the oscillations is larger than the time between two separate eddies interacting with the drop, the oscillations might lead to the breakup of the drop.

The above-mentioned studies were mostly focused on developing theoretical descriptions

for the breakup. On the other front of studies on the turbulent breakup phenomenon, the focus is divided into two main categories of experimental and numerical studies. As both approaches are used in this thesis work, it is important to review the most important studies in both approaches.

Experimental breakup studies

Early experimental investigations of drop breakup visualization using high-speed photography were carried out in 1980s (Chin and Han, 1979, 1980). Many of the studies were focused on the impact of different parameters (Weber number, viscosity ratio of the disperse and continuous phase, drop size, etc.) on the breakup characteristics.

Krzeczkowski (1980) identified different breakup morphologies for liquid drops in air and found that breakup morphology and duration depend strongly on the Weber number and to some degree, the viscosity ratio i.e. an increase of 3 orders of magnitude of the viscosity ratio only increased the breakup duration twice. Eastwood et al. (2004) reported significant stretching of drops at low Weber numbers with more prominent stretching for the higher viscosity of the disperse phase. Hančil and Rod (1988) reported an increase in breakup frequency with increasing the mother drop size. Martínez-Bazán et al. (1999) reported that the breakup frequency monotonically increases with the dissipation rate of turbulent kinetic energy.

Andersson and Andersson (2006b) studied the differences of the breakup of drops and bubbles as a good measure of how the viscosity of the disperse phase as an additional stabilizing factor (besides the interfacial tensions) affects the breakup properties. They reported differences in the fragments size distribution (drops tend more towards equal sized fragments) and the number of fragments (bubbles tend more towards binary breakup) while similarities could be observed such as the initial deformations. They also reported that the time scales of the eddies responsible for large deformations leading to breakup are about $1/2 - 2/3$ of the turbulent time scale k/ε and therefore concluded that only the large turbulent eddies contribute to the breakup of both drops and bubbles. In a separate study, Andersson and Andersson (2006a) reported that the eddies with sizes $1 - 3$ times the drop diameter are the most contributing eddies to the breakup.

Solsvik and Jakobsen (2015) observed higher probability of unequal sizes of bubble daughter fragments after breakup in a stirred tank. Also, the probability of binary breakup was higher at low stirring power while more multiple breakup was observed at higher power. Furthermore, achieving a reliable breakup model was not possible due to the difficulty of measuring local turbulent properties of the flow e.g., dissipation rate of turbulent kinetic energy.

Solsvik et al. (2016) defined the terms for the morphology of the drops breakup i.e., "initial breakup", "breakup cascade", and "independent breakup". For the initial breakup, the breakup is considered as finished as the first fragment is observed and for the breakup cascade, the final breakup of intermediate daughter drops is considered as the end of breakup. The independent breakup events describe the breakup events when a daughter drop relaxes into a spherical shape, deforms and breaks up.

Ashar et al. (2018) reported an increase of the drop deformation time with increasing the mother drop size in a stirred tank. They also observed a monotonic increase of breakup probability as well as number of daughter drops by increasing the Weber number. Zhou et al. (2021) observed decreased breakup time by increasing the interfacial tension and drop viscosity. They observed that breakup time was independent of the stirring speed. Zhang et al. (2021) studied a turbulent jet and reported an increase of breakup time up to a certain Weber number, where the breakup time is the longest. Beyond that Weber number, the breakup time decreased. A breakup morphology mapping was proposed based on the Weber number ranges with dominant binary and multiple (non-binary) breakup.

Herø et al. (2020) reported a direct relationship between the drop size and breakup probability inside a turbulent channel. They used the same breakup definition as those of Solsvik et al. (2016). With the "initial" breakup definition, they reported binary breakup events with almost uniform size distribution. For the "cascade" breakup, they reported an increase of the number of daughter drops with increasing the size of the mother drop with a size distribution indicating high probability of very small daughter drops. Vejražka et al. (2018) reported a direct relationship between the number of daughter bubbles and the Weber number. Also the size distribution of the daughter bubbles is controlled by the number of fragments i.e., a U-shaped size distribution was reported for binary breakup meaning that if the bubble breaks into two daughter bubbles, the difference of the sizes of the daughter bubbles tend to be large.

Fewer experimental studies focused on the breakup of drops in the context of geometries similar to high-pressure homogenizers. Galinat et al. (2005, 2007) investigated drop breakup downstream an orifice in a turbulent pipe flow. They found that the number of daughter droplets was directly related to the Weber number. Also, at lower Weber numbers, unequal sized daughter droplets were more dominant while increasing the Weber number increased the probability of symmetrical breakup events. They defined a global Weber number based on the maximum pressure drop over the gap (orifice) and breakup probability was modeled based on this Weber number.

Innings and Trägårdh (2005) studied drop breakup in an HPH scale-up model through taking snapshot images of the drops passing through the gap an breaking up in the outlet chamber. They concluded that breakup only occurs inside the outlet chamber and only limited drop deformations occur in the inlet chamber. In a later study, Innings et al. (2011)

attempted to relate the breakup morphologies observed in their experiments to the classic turbulent breakup mechanisms i.e., TI and TV regimes. Their conclusion was that eddies with sizes smaller to very larger than the drop contribute to the drop breakup suggesting that both TI and TV mechanisms are responsible. However, they suggest that larger eddies deform the drops through velocity gradients while smaller eddies act through inertial pressure fluctuations.

Kelemen et al. (2015b) also reported no observation of breakup in the inlet chamber. Just after the gap (orifice) exit, no deformation was observed for low viscosity ratio ($\mu_d/\mu_c = 2$), while for higher viscosity ratio ($\mu_d/\mu_c = 14$) deformations were observed with neck formation implying probability of binary breakup. Breakup events were only observed after 8 orifice diameters. Further downstream at distances above $20 - 40$ orifice diameters, for low Reynolds numbers (laminar condition inside the orifice), breakup events were observed in the form of Rayleigh instability and binary breakup for the low and high viscosity ratios, respectively. Due to limited resolution, no breakup result was reported for transitional flow regime.

Mutsch et al. (2021) reported the scalability of drop breakup using three different scales of HPH-like geometries. They also reported the turbulence after the gap exit as the main cause of drop breakup. They also investigated the impacts of Reynolds number, viscosity ratio, and drop trajectories on the breakup. They observed earlier breakup positions for higher Reynolds numbers. Also, they observed longer deformation times (longer elongations of drops) for low viscosity ratio. Furthermore, they reported smaller fragments after breakup for the drops closer to the gap walls. However, no impact of the trajectory on the drop size distribution was observed.

Numerical breakup studies

Not only recently, the researchers started using high-fidelity CFD (LES and DNS) to study single drop breakup phenomenon with all of them working on ideal turbulent condition of homogeneous isotropic turbulence.

Karimi and Andersson (2020) used LES to study the drop breakup in a flow-cell with conditions close to homogeneous isotropic turbulence. They validated their results with the experiments in terms of drop breakup properties such as breakup rates and deformation time and showed good agreement between the two approaches. They suggested that higher resolution CFD is required to obtain information regarding the drop-turbulence interactions which could be useful to be incorporated into population balance equations.

The other researchers used DNS for the numerical studies of single drop breakup. Shao et al. (2018) showed that increasing the Weber number leads to smaller drops and higher num-

bers of daughter drops. Komrakova (2019) reported the observation of the same breakup behavior as reported by the experimental work of Solsvik et al. (2016). They also observed another type of breakup event called "burst" breakup which they associated it with high energy levels and large initial size of the drop. Rivière et al. (2021) studied the breakup of bubbles with sub-Hinze scales in turbulent regime. They reported a critical Weber number below which no breakup events are observed with the number of daughter drops with sub-Hinze scales increasing as the Weber number is increased.

Vela-Martín and Avila (2021) studied the interactions of the flow structures with the drops and bubbles. They categorized the flow structures into "inner" and "outer" eddies based on their distance from the drop interface which implies whether they are affected by the drop through surface tension or drop physical properties. They concluded that at low Weber numbers, the breakup is mainly driven by the outer eddies as an energy source while the inner eddies serve as a sink by dissipating the energy they obtain from the drop interface. For higher Weber numbers, inner eddies also contribute to the deformation of the drop. In a later study, Vela-Martín and Avila (2022) proposed that the breakup rate is only dependent on the Weber number and they challenged the understanding of breakup based on Kolmogorov-Hinze by suggesting that the breakup rates persist in sub-Hinze scales.

Håkansson et al. (2022a) attempted to characterize the condition of critical deformation leading to the breakup. Considering a typical binary breakup where a neck is formed between two bulbs, they rejected the possibility of predicting the critical deformation (after which the drop breaks up) based on the total interfacial area. Alternatively, they proposed that the state of critical deformation is reached when the curvature at the neck is higher than that of the smallest bulb as an indication of higher static pressure in the neck leading to a flow inside the drop toward the larger bulb which eventually leads to breakup. Håkansson and Brandt (2022) investigated the drop breakup in HIT with an attempt to connect the findings to the breakup of drops in emulsification devices. They suggested the Weber number to be the deciding factor on the breakup morphology. They also reported a decrease in the initial breakup time (Observation of the first breakup) with increasing the Weber number.

As discussed above, a substantial body of literature provides information on the breakup of droplets in idealized conditions (Håkansson and Brandt, 2022; Komrakova, 2019; Qian et al., 2006; Rivière et al., 2021; Vela-Martín and Avila, 2021, 2022). However, investigations of drop breakup under non-ideal turbulence conditions such as the one in the outlet chamber of a high-pressure homogenizer were limited to experimental studies which have their limitations, particularly in terms of accurately describing the turbulence characteristics of the flow field. The missing link the current thesis work pursued was to investigate how much the previous findings were in agreement for these non-ideal turbulent conditions. Furthermore, by having the vast information of the turbulent properties provided by DNS, a better understanding of the conditions which drive a drop towards breakup in

an industrially-relevant geometry seems achievable.

1.3 Current study's approach

In the current study, both experimental and numerical approaches are used to study the single-phase flow fields as well as deformation and breakup of drops in a high-pressure homogenizer (HPH) scale-up model. First, a scale-up model is designed to establish a similarity between a real HPH and a model (see section 2.1). This is done to provide practically working conditions in the lab i.e., enlarging the drops, reducing the velocities for easier visualization through high-speed photography, etc. As the next step, in **Paper I**, direct numerical simulation (DNS) was used to study the single-phase flow inside the geometry of the designed scale-up model. In **Paper II**, the capabilities of LES and RANS models were investigated to see how much of the information in the benchmark study (DNS) could be captured by these turbulence models as they are more favored in the industry due to less computational cost.

With a DNS flow field converged to statistical steady-state, the injection of the drops as the second phase was possible. The introduction of the second phase into the numerical framework was carried out through the use of a volume of fluid (VOF) method with a highly resolved interface tracking method i.e. method of multi-dimensional tangent of hyperbola for interface capturing (MTHINC) (Ii et al., 2012).

In **Paper III**, the results of the breakup of drops in the HPH valve model were compared to those for an ideal condition of homogeneous isotropic turbulence (HIT). In **Paper IV**, a validation of the DNS-VOF framework for the simulation of the drops breakup was done through experiments. This validation provided the confidence to use the DNS flow field information in the vicinity of the drops, in **Paper V**, to study the underlying physical reason for the turbulent breakup phenomenon.

1.4 Aims and research questions

The long-term aim of this research is to provide the insights needed to optimally design and operate emulsification devices such as high-pressure homogenizers. The aim in this thesis is to build methodologies for studying the turbulent hydrodynamics and breakup in the outlet chamber jets based on DNS-techniques, and to use these to better understand turbulent deformation and breakup of emulsion drops in these devices. The specific research questions are:

- To what extent does the turbulence inside the outlet chamber differ from more idealized homogeneous isotropic turbulence as well as other types of wall jets? And how

does the dissipation rate of turbulent kinetic energy (which is arguably of large importance for understanding breakup but is difficult to obtain) look?

- How well can the less computationally costly CFD-techniques (industry standard) such as RANS-CFD and LES describe the relevant turbulent quantities in such a confined outlet chamber jet?
- What should be RANS-CFD best practice recommendations for modeling HPH outlet chamber jets?
- How different is the turbulent drop breakup in the cases of idealized homogeneous isotropic turbulence and a wall jet in the HPH outlet geometry?
- How well does the in-silico numerical drop breakup technique comply with in-vitro experimental results from high-speed visualizations?
- Where and how does drop breakup in the HPH outlet chamber jet take place?

Chapter 2

2 Experimental methodology

In this chapter, the experimental approach is discussed as one of the two key methods employed in this study. First, section 2.1 discusses the scale-up procedure. Section 2.2 provides more information on the experimental setup components. Finally, section 2.3 describes the procedure of drop visualization including the high-speed photography and image-processing.

2.1 Scale-up model

Designing an experimental scale-up model of an HPH valve was the first step of the project. In designing the model, two homogenizers, including a production- and a pilot-scale machine with capacities $8500 l/h$ and $120 l/h$ were considered as references.

Two main requirements should be considered in a scale-up procedure: i) Experimental and numerical feasibility, and ii) Proper representation of the physics i.e., similarity.

2.1.1 Experimental and numerical feasibility

The first requirement in a successful scale-up is the feasibility of the model in terms of experimental and numerical studies i.e., ensuring that the designed model takes into account the limitations of both experimental and numerical studies that will be performed on the model. For instance, one important parameter to consider in this thesis work was the bulk velocity of the flow in the gap. The limitations of the high-speed camera in terms of frames-per-second and shutter-speed must have been taken into account in deciding the bulk velocity in the gap to ensure that the velocities do not become too high to be captured by the camera. Moreover, the drops to be investigated must be sufficiently large to be captured by the camera which is limited by the resolution of the camera sensor. Furthermore,

the numerical study also sets a number of limitations on designing the scale-up model. One important parameter to consider is the size of the domain which directly affects the computational cost and therefore, care should have been taken in deciding the size of the scale-up model. Moreover, a simple geometry was also an advantage to the DNS setup. A cuboidal domain made it easy to generate uniform grid (mesh) cells with sufficiently small sizes to capture the smallest turbulent scales (Kolmogorov-scales).

2.1.2 Proper representation of the physics

The second requirement in a scale-up procedure is ensuring that the scale-up model properly represents the actual physical phenomenon. In order to do so, geometric, kinematic, and dynamic similarities are desirable between the model and the actual physical phenomenon. Briefly, geometric, kinematic, and dynamic similarities require the corresponding lengths, velocities, and forces to be similar (proportional) in the model and the actual setup, respectively.

Geometric and kinematic similarity

Having geometric similarity is the first step. In this study, the relevant geometric similarity is assumed to be determined by the ratio of the initial drop diameter to the gap height and Kolmogorov length-scale i.e., D_0/h and D_0/η, as these determine the largest i.e., Integral length-scales $L_t \approx 3h$ (Innings and Trägårdh, 2007), and the smallest turbulent scales of the flow. This is the approach also taken by Innings et al. (2011).

Regarding the drop sizes, it should be noted that the larger initial drop sizes are more preferable due to practical reasons as larger drops could be beneficial in terms of visualization in the experiments. According to Innings et al. (2011), in a channel flow, the drops with diameters larger than half of the height of the channel are significantly affected by the walls of the channel. In order to avoid such impacts on the drops, drop sizes smaller than the half channel height are desired. Furthermore, the drop sizes should be large enough for visualization purposes. Such a case is observed in the pilot-scale homogenizer where the ratio of D_0/h is equal to 0.33. Therefore, the geometric similarity is considered to be based on the pilot-scale homogenizer. A scale factor of 50 was considered which led to a gap height and initial drop diameter of $750\mu m$ and $250\mu m$, respectively. The dimensions for all cases are presented in Table 2.1.

Since the gap length only affects the boundary layer, in order to decrease the pressure loss due to the friction along the gap, the gap length is scaled only by a factor of 5 leading to a value of $5mm$. Another argument to reduce the gap length to $5mm$ was to have the same geometrical ratio of l_g/h as that in the production-scale homogenizer. This does not com-

Table 2.1: Geometrical and physical properties of the production- and pilot-scale HPH compared to those of the scale-up model

	Production-scale HPH	**Pilot-scale HPH**	**Scale-up model (Paper I, II, III)**	**Scale-up model (Paper IV, V)**
Geometry				
Gap height (h) [μm]	150	15	750	750
Initial drop diameter (D_0) [μm]	5	5	250	250
Gap length (l_g) [mm]	1	1	5	5
Other information				
Gap bulk velocity (U_g) [m/s]	175	115	16	6.4
Volume flow rate (Q) [l/h]	8500	120	324	129.6
Disperse/Continuous phases properties				
Continuous phase density (ρ_c) [kg/m^3]	1000	1000	1200	1080
Disperse phase density (ρ_d) [kg/m^3]	700	700	700	945
Continuous phase dynamic viscosity (μ_c) [$mPa.s$]	1	1	7	2.44
Disperse phase dynamic viscosity (μ_c) [$mPa.s$]	35	35	35	25.1
Turbulence properties				
Dissipation rate of TKE (ε) [m^2/s^3]	4.5×10^8	1.3×10^9	6.8×10^4	4.4×10^3
Kolmogorov length-scale (η) [μm]	22	17	7.3	7.2
Integral length-scale (L_t) [μm]	450	45	2250	2250
Dimesionless numbers				
Reynolds number (Re)	26000	1700	2057	2120
Drop Reynolds number (Re_d)	875	575	685	708
Weber number (We)	90	180	209 (**Paper I & II**) 1, 5, 96 (**Paper III**)	82 (**Paper IV**) 3 (**Paper V**)
Capillary number (Ca)	0.34	0.49	0.47	0.18
h/η	690	90	102	105
D_0/η	23	30	34	35
D_0/L_t	0.01	0.11	0.11	0.11
δ_{99}/h	0.08	0.98	0.28	0.28
D_0/h	0.03	0.33	0.33	0.33
T_{TI}	1.9	2.6	22	11
T_{TV}	0.03	0.03	0.2	0.1

promise our dynamic similarity criterion, since the ratio of δ_{99}/h, where δ_{99} is the boundary layer thickness, remains in the acceptable range (between the values for the production-scale

and pilot-scale homogenizer). An approximation for this value is provided by Schlichting and Gersten (2000) as:

$$\delta_{99}/h = 5\sqrt{\frac{\nu_c l_g}{h^2 U_g}} \tag{2.1}$$

where ν_c is the kinematic viscosity of the continuous phase. By having the geometric similarity in our case, the streamlines will be similar to the case of pilot-scale and the kinematic similarity will be met as well.

Dynamic similarity

Having a full dynamic similarity between the experimental model and the production/pilot scale homogenizers seems not to be attainable (as also discussed by others, e.g., Innings et al. (2011); Kelemen et al. (2015a)). In the case of dynamic similarity, one should ensure that the most relevant dimensionless numbers (obtained from a dimensional analysis) are equal for the experimental model and the actual case. Different sets of dimensionless numbers have been offered to affect the flow and breakup behaviors in an HPH outlet chamber. To understand the relevance of different dimensionless numbers, we look into the physical interpretations and definitions of each number.

Reynolds number is the measure of the turbulence of the flow field. The definition of Reynolds number is usually different based on the geometry of the problem. In the context of the flow field in an HPH outlet chamber, the Reynolds number is usually defined based on the gap height and gap bulk velocity, as follows:

$$Re = \frac{\rho_c U_g h}{\mu_c} \tag{2.2}$$

As discussed in section 1, according to the Kolmogorov-Hinze theory, the two main drop breakup mechanisms observed in the case of a homogenizer are the turbulent viscous (TV) and turbulent inertial (TI) mechanisms. In TV, the breakup occurs due to the viscous stresses i.e. velocity gradients by the eddies which are larger than the drop. In TI, the forces of the smaller eddies due to local pressure fluctuations which are mainly in the perpendicular direction of the drop interface lead to the breakup of the drops. Since the breakup mechanism is considerably affected by the size of the drops compared to the eddies size, one could use the drop Reynolds number, Re_d (Reynolds number based on the diameter of the drops and the velocity of the flow near the drop interface) to differentiate between these two regimes. The value of unity for Re_d defines the boundary between the TV and TI

mechanisms (Walstra and Smulders, 1998). A value of $Re_d > 1$ could be defined as the indication of TI regime in which the inertial forces are prevalent and values of $Re_d < 1$ could be considered to be the indication for TV regime in which the viscous forces primarily contribute to the breakup of the drops. Re_d could be defined as follows:

$$Re_d = \frac{\rho_c U_g D_0}{\mu_c} \tag{2.3}$$

Re_d is obtained to be in the acceptable range for the experimental model. However, it should be noted that the flow velocity near the drop interface is estimated to be the same as the gap velocity. In order to have an estimation of the probability of the breakup of the drops, a dimensionless number could be defined as the ratio of the destabilizing stresses exerted on the drop to the stabilizing stresses which oppose any deformation. In TI regime, this number is called the Weber number which could be defined as follows:

$$We = \frac{2\rho_c \varepsilon^{2/3} D_0^{5/3}}{\gamma} \tag{2.4}$$

where γ is the interfacial tension at the interface between the two phases. Various studies, either experimentally (Ashar et al., 2018; Galinat et al., 2007; Herø et al., 2020) or numerically (Håkansson and Brandt, 2022; Shao et al., 2018; Vela-Martín and Avila, 2021, 2022), have shown the Weber number to be an important factor determining the characteristics of turbulent drop breakup.

In TV regime, due to the fact that the viscous stresses are the main destabilizing stresses, another number called the capillary number play an important role in the drop breakup (Eastwood et al., 2004; Lemenand et al., 2013; Skartlien et al., 2013) which is defined as follows:

$$Ca = \frac{\mu_c \varepsilon^{1/3} D_0^{1/3}}{2\gamma} \tag{2.5}$$

As indicated in Eq. 2.4 and Eq. 2.5, ε i.e., dissipation rate of turbulent kinetic energy, is an important parameter in determining the breakup behavior and therefore in the scale-up procedure. Due to the highly anisotropic nature of the flow field inside an HPH outlet chamber, determining the value of ε is quite challenging (as discussed in **Paper III**). For this purpose, the estimation proposed by Innings and Trägårdh (2007) is used:

$$\varepsilon = \frac{U_g^3}{80h} \tag{2.6}$$

Scaling of relative time-scales

As suggested by Innings et al. (2011), it is claimed to be theoretically impossible to scale relative time-scales while maintaining the important dimensionless parameters in the acceptable range.

Two important time-scales to be investigated in drop breakup studies are the eddy time-scale (lifetime), $\tau_{\text{eddy}} = \left(\frac{l}{\varepsilon}\right)^{1/3}$, where l is the eddy length scale in the inertial region (approximated to be in the order of the drop size i.e., D_0), and the drop deformation time, $\tau_{\text{def}} = \frac{\mu_d}{\sigma}$, where σ is the external stress applied to the drop, either in TI or TV regime (Innings et al., 2011; Walstra and Smulders, 1998). There are different suggestions in the literature regarding the definition of the drop deformation time (Andersson and Andersson, 2006a; Maaß and Kraume, 2012). But, for the purpose of scaling, the chosen definitions seem to be sufficiently satisfactory.

Defining a dimensionless number as the ratio of these two time-scales (τ_{eddy} and τ_{def}) provides a tool for evaluating whether the eddies are able to break the drops. Based on the breakup regime, two dimensionless numbers are defined as follows, for the turbulent inertial regime:

$$T_{TI} = \frac{\tau_{\text{eddy}}}{\tau_{\text{def}_{TI}}} = \frac{\rho_c \varepsilon^{1/3} D_0^{4/3}}{\mu_d} \tag{2.7}$$

and for the turbulent viscous regime:

$$T_{TV} = \frac{\tau_{\text{eddy}}}{\tau_{\text{def}_{TV}}} = \frac{\mu_c}{\mu_d} \tag{2.8}$$

Small values of these numbers show that the eddy lifetime could be a limiting factor in the breakup of the drops and the eddies do not have sufficient time to interact with the drops.

Researchers have proposed different sets of dimensionless numbers as the most relevant ones for a scaling procedure of an HPH valve geometry. Innings et al. (2011) (which was the basis for the scale-up procedure in the current study) proposed Re, We, Ca, T_{TI}, T_{TV}, as well as geometrical ratios d/h and d/η to be the most relevant dimensionless numbers for a proper scale-up of an HPH valve. More recently, Preiss et al. (2021) carried out a scaling of an HPH valve geometry based on dimensionless numbers Re, We (based on gap bulk velocity, i.e. $We = \frac{\rho_c U_g^2 D_0}{\gamma}$), density ratio ($\frac{\rho_d}{\rho_c}$), viscosity ratio ($\frac{\mu_d}{\mu_c}$), as well as geometrical ratios D_0/h and the ratio of gap height to the outlet chamber width.

A list of important dimensionless numbers used in this study could be found in Table 2.1. Meeting the requirement of having all these numbers to be equal in two cases is not possible. Therefore, we had to consider to make some compromises. In this study, the effort was to have the dimensionless numbers as close as possible to those of the two cases of production- and pilot-scale to provide a case where a high-pressure homogenizer could potentially work. This is achieved by adjusting different parameters such as the flow velocity and the materials properties. Sucrose solution was used as the continuous phase for which the properties were changed by adjusting the sugar content i.e., Brix degree. For the two sets of **Papers I, II, & III** and **Papers IV & V**, two different sucrose solutions with 45% w/w and 25% w/w sugar contents were used, respectively (cf. Table 2.1). The reason for this was to compensate for the limitations of the experimental visualizations (limited frames-per-second which could be captured by the camera) by reducing the flow velocity while keeping the dimensionless numbers in acceptable proximity of those of production- and pilot-scale HPHs.

The values of Re, Re_d, h/η, D_0/L_t, δ_{99}/h, and D_0/h are in the ranges between those of the production- and pilot-scale HPH valves. For the other dimensionless numbers, the attempt was made to get as close as possible to the corresponding values. The most difficult numbers were the time-scales T_{TI} and T_{TV}. As also concluded by others (Innings et al., 2011; Kelemen et al., 2015a), a proper scaling of these time-scales besides other relevant dimensionless numbers is not fully achievable. However, one could justify that since the values are higher, there is no concern about the occurrence of the breakup compared to the reference homogenizers (i.e., the eddies have more time to interact with the drops). Furthermore, as a general comment, the values for the production- and pilot-scale HPH valves are not fixed and the machines are operable with somewhat different conditions (pressure, flow rate, etc.). Therefore, the concern to reach the exact values of dimensionless numbers is not necessary.

2.2 Experimental setup

An overview of the experimental rig is presented in Fig. 2.1. A tank with coil heat-exchanger keeps the water at the room temperature ($T = 20^{\circ}C$) to prevent temperature increases due to the constant pumping of the continuous flow and maintain the required physical properties e.g., viscosity, density, etc. A mechanical pump (Grundfos model CHI 2–60 A-W-G) pumps the continuous flow. The flow rate is adjusted using a frequency converter. Measurement instruments e.g. flow transmitter (Danfoss, Type MAG 1000), temperature transmitter (Therma 1, Electronic Temperature Instruments, Worthing, United Kingdom), and analogue pressure gauge (Alfa Laval Corporate AB, Lund, Sweden) are used to monitor and ensure the safe operation of the setup. The continuous flow goes through the scale-up HPH model and returns to the tank.

Fig. 2.2 shows the flow cell (scale-up HPH) model. The continuous flow comes in from

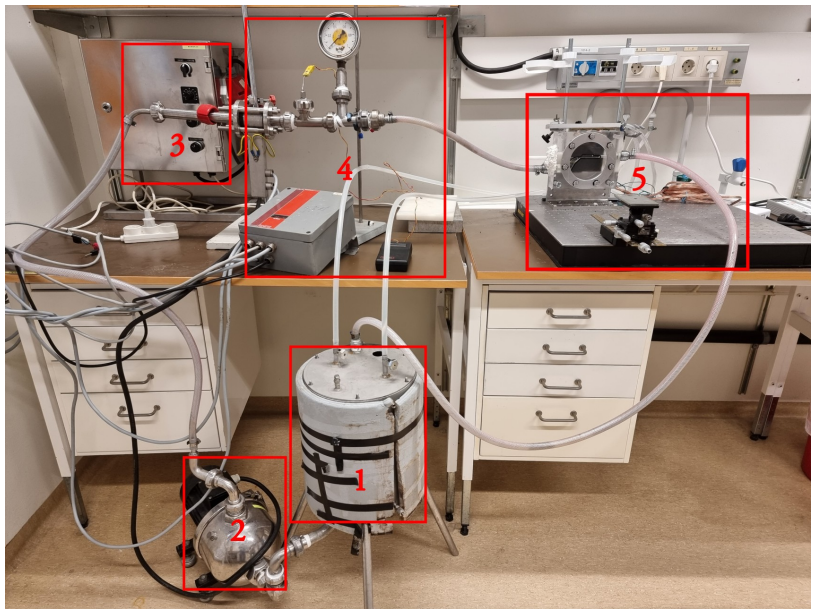

Figure 2.1: Experimental rig including (1) Tank, (2) pump, (3) frequency converter, (4) measurement instruments, (5) optical table, camera, and flow cell (scale-up model)

the left side, entering the inlet chamber and then going through the narrow gap. The oil, i.e., Miglyol 812 (Caesar & Loretz GmbH, CAS No. 73398 − 61 − 5) is injected into the continuous flow using a 27-gauge needle (B. Braun Holding GmbH & Co. KG) at some distance before the gap inlet. To prevent coalescence and carry out a focused study on the breakup phenomenon, a very low fraction of disperse phase (oil) was used (the oil was injected with flow rate 5 ml/min in 7 liters of the continuous phase, corresponding to a maximum of 2% oil-in-water volume fraction for a typical 30-minute experiment session) which minimized the interaction of individual drops and therefore no major coalescence events were observed. Just after the narrow gap, a wall-adherent jet forms inside the outlet chamber and the flow exits from the right side. The whole model is made of acrylic plastic to make is optically accessible from all sides. For the best optical access, a fused quartz double-sided flat glass with flatness $\lambda/20$ at 633 nm (Knight Optical, UK, Ltd, Roebuck Business Park Harrietsham, Kent) is mounted in front of the field of view of interest using a steel ring. An in-house high-intensity lighting system comprising of 4 green LEDs (PT-121-G, Luminus Devices, Inc, Sunnyvale, CA, USA) with a total maximum power of $500\,W$ and a water-cooled aluminum block is mounted on top of the flow cell.

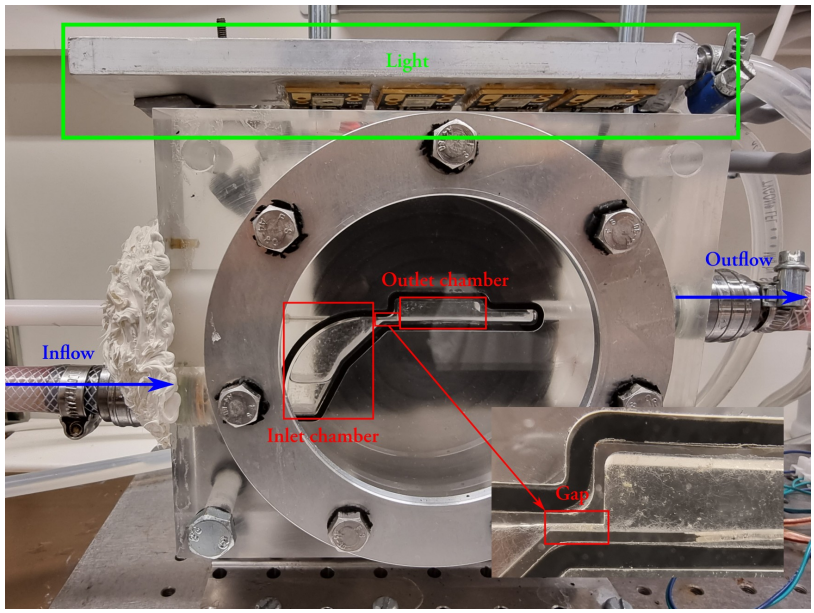

Figure 2.2: Flow cell (scale-up HPH) model

2.3 Drop visualization

The process of drop visualization is explained in two steps in the following sections. First, obtaining the raw images of the drops through high-speed photography is explained in section 2.3.1. In section 2.3.2, the image-processing technique which is performed on the raw images is described.

2.3.1 High-speed photography

High-speed camera

A high-speed camera (Model OS3-V3-S3, Integrated Design Tools Inc., Tallahassee, Florida USA) was used for the collection of drop breakup images at a resolution of 1568 px × 488 px at 18800 frames per second (fps). This leads to a resolution of 24 px per initial drop diameter (D_0) and maximum drop movements (occurring close to the gap exit) of less than $0.5h$ between each pair of subsequent frames.

Lighting, oil staining and filtering

The high-intensity light is crucial for the high-speed photography, but the preliminary tests showed that it is not sufficient. Fig. 2.3a shows a sample image from the preliminary tests with the injection of oil into the flow. As seen in this figure, oil drops are hard to be distinguished. The presence of a relatively large drop at the top of the channel in this figure shows that not all parts of the drop reflect the light which makes it hard to determine the real size of the drop. Furthermore, there is no concrete way of distinguishing oil drops from air bubbles that could exist in the continuous flow in the first stages of turning on the pump. Staining the oil with Nile-red clearly showed an improvement in the captured images. Miglyol 812 was mixed with 146 ppm Nile red (Sigma-Aldrich, CAS No. $7385 - 67 - 3$) overnight and was used as the disperse phase. To account for the impact of the dye on the interfacial tension, which is believed to generally decrease it (Maaß and Kraume, 2012), the interfacial tension was measured using the stained-oil in an equilibrium state through a pendant drop technique (Teclis, Civrieux-d'Azergues, France) and Young-Laplace equation. The value of the interfacial tension was measured to be $\gamma = 7.02$ mN/m. As shown in Fig. 2.3b, the dye-stained oil drops are clearly distinguishable from the surrounding environment.

The reasoning behind choosing a green light was to ensure that the light source has a wavelength far from those of the red color ($620 - 750$ nm) to better take advantage of the distinguishability of Nile red dye. Green light was a clear choice for this purpose with wavelengths $495 - 570$ nm. Another idea was to use an orange long-pass filter to only allow the dye-stained drops to be visible to the camera. However, this idea was concluded to be impractical at a later stage due to the need for lower exposure times. High exposure time i.e., low shutter speed leads to the camera lens being exposed to the light for a longer time leading to artificial elongation of the drops in the images taken. Therefore, low exposure times are favorable to reduce this artificial elongation which in turn results in darker images. Moreover, using an orange filter makes darker images. The superimposed effects of the filter and low exposure resulted in fairly dark images.

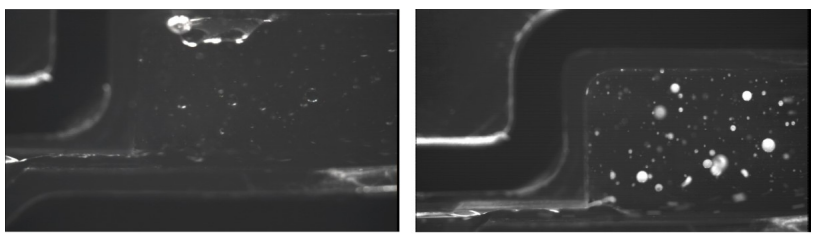

(a) (b)

Figure 2.3: The impact of staining the drops with Nile red dye, (a) Non-stained drops, (b) Nile red stained drops

Injection positioning

Another important aspect for the improvement of the experimental results was to determine the position of the needle tip. As shown in Fig. 2.4a, in the case the needle tip is positioned exactly at the inlet of the gap, a stream of oil is generated instead of spherical drops. However, moving the needle tip further upstream showed significant improvements in that term. As shown in Fig. 2.4b, when the needle tip was positioned at an approximate distance of $8h$ upstream the gap inlet, the injected oil drops had enough time to stabilize into spherical shapes before entering the gap.

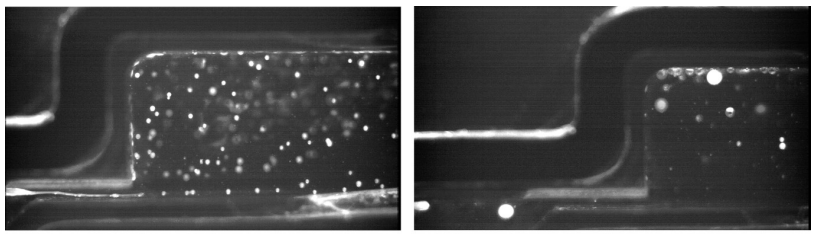

(a) (b)

Figure 2.4: The impact of the position of the needle, (a) Needle at the gap inlet, (b) Needle at 7h before the gap inlet

2.3.2 Image-processing

Image-processing was an important step not only to detect the drops and enhance the quality of the images (drop extraction), but also to quantify the description of the drop breakup events i.e., to extract the drops positions, circularity (defined as $C = \frac{4\pi A}{P^2}$, where A is the drop interfacial area, and P is the perimeter), etc. (feature extraction). The image-processing is described in full details in **Paper IV**, section 2.2.2. A brief summary of the image-processing steps is described here.

Drop extraction

The image-prcoessing was performed through an in-house script written in MATLAB R2019a (MathWorks, Natick, MA). It consisted of a series of filtering, enhancement, and conversion steps. The impact of each step of the image-processing is illustrated in Fig. 2.5. See **Paper IV** for further details on the settings of each filter.

After obtaining the binarized images, MATLAB's built-in function *regionprops* was used to extract the geometrical properties of all of the objects in the images. The delayed injection of individual drops in the experiments made it possible to extract the largest object in each frame as the main drop (since no drop was injected until the previous drop was broken).

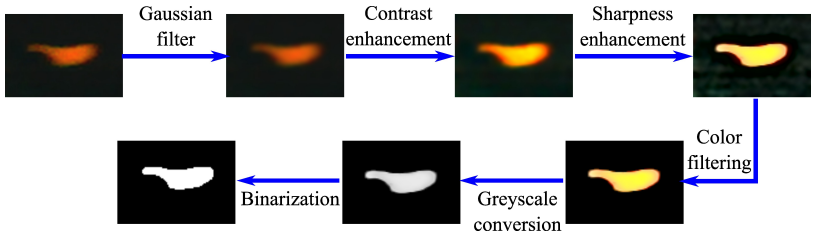

Figure 2.5: The image-processing steps (Reprinted from **Paper IV** with permission).

Drop filtering

In the numerical approach, the conditions such as the drop initial diameter (D_0), and the injection position are set to constant values. However, this is practically impossible to be achieved in the experimental framework. Therefore, before extracting the geometrical features of the experimental drops, we had to ensure that only the drops with as much as possible similar conditions to the numerical setup are detected and analyzed to perform a fair comparison of the numerical and experimental approaches. An important capability that the image-processing provides is the filtration of the drops based on desired attributes. After performing the image-processing on the raw images, three filters are applied on the drops properties to keep the ones closest to the numerical drops and discard the others. Fig. 2.6 provides a summary of the filtering steps applied on the experimental drops.

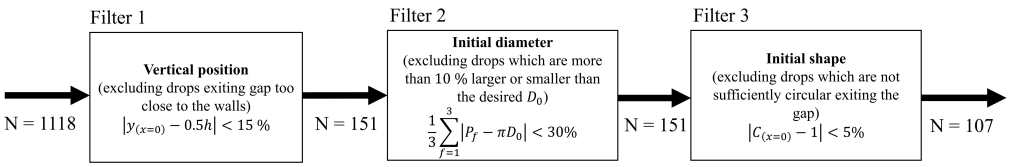

Figure 2.6: The filtering steps applied on the experimental drops (Reprinted from **Paper IV** with permission).

Filter 1 identifies the drops which exit the gap within 15% distance of the middle of the gap ($y_{x=0}$) i.e., where the numerical drops are injected. In the second step, a filtering is applied on the initial diameter of the drops. This is done by ensuring that the mean perimeter of the drops in the first three frames they appear inside the gap is not larger than 30% of the perimeter of the drops with the desired diameter $D_0 = h/3$. In other words, this ensures that the drops will have a maximum 10% difference in the average diameter compared to the numerical drops. The final filter is applied on the circularity of the drops. This filter only passes the drops with a maximum 5% difference in circularity compared to a perfect circle (2D projection of the sphere). 107 out of 1118 drops pass the filtering steps.

Feature extraction

Finally, using MATLAB's built-in function *regionprops*, the most important geometrical features of the filtered drops such as area, centroid, perimeter, etc. are extracted.

Chapter 3

3 Numerical methodology

The numerical simulations, as the second key approach in this study are discussed in this chapter. The domain used in the numerical simulations is described in section 3.1. Direct numerical simulation (DNS), Large-eddy simulation (LES), and Reynolds-averaged Navier-Stokes (RANS) as the three main approaches in simulating the single-phase flow are discussed in section 3.2. The turbulent flow inlet boundary conditions and convergences studies are discussed in sections 3.2.1 and 3.2.2, respectively. Finally, single drop simulations using DNS and a volume of fluid (VOF) scheme for resolving the two-phase interface is explained in section 3.3.

3.1 Numerical domain

The numerical domain is illustrated in Fig. 3.1. The solid lines show the extent of the scale-up model which is used in the numerical studies which is basically the outlet chamber of the HPH model. The other parts (designated with dashed lines) are the parts before and after the outlet chamber which are not included in the numerical domain. These parts include the inlet chamber, the gap, and the flow discharge channel right after the outlet chamber. The green and red planes show the inlet and outlet boundaries of the domain, respectively. The walls of the outlet chamber are designated with gray surfaces. Periodic boundary condition is applied in the spanwise direction to reduce the size of the domain (instead of resolving the entire width of the domain) and a synthetic turbulence generation technique is used at the inlet boundary condition (gap exit), as discussed in section 3.2.1.

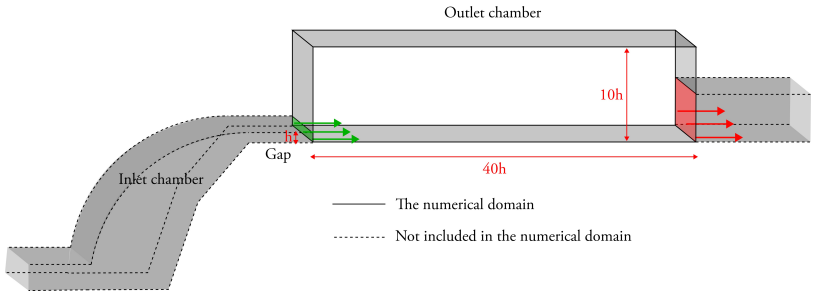

Figure 3.1: Schematic illustration of the numerical study domain.

3.2 Single-phase DNS, LES, and RANS

The fluid flow motion is governed by the mass and momentum conservation i.e., Navier-Stokes equations which are a set of non-linear partial-differential equations (PDEs). For an incompressible flow, the Navier-Stokes equations are as follows (using Einstein notation):

$$\frac{\partial u_i}{\partial x_i} = 0 \tag{3.1}$$

$$\frac{\partial u_j}{\partial t} + \frac{\partial u_i u_j}{\partial x_i} = -\frac{1}{\rho_c}\frac{\partial p}{\partial x_j} + \nu_c \frac{\partial^2 u_j}{\partial x_i \partial x_j} + f_j \tag{3.2}$$

where u and f are velocity and body force vectors, respectively.

These equations are solved numerically through finite-volume method. This could be done through direct numerical solution of Eqs. 3.1 and 3.2 i.e., DNS, or through turbulence models e.g., LES and RANS.

DNS

DNS directly solves Eqs. 3.1 and 3.2 with no simplifications and modeling of turbulent characteristics. However, this comes with a considerable computational cost since it requires a high-resolution grid and small time-steps to capture the smallest turbulent scales i.e., Kolmogorov-scales. The size of the grid used for the simulations in **Papers I, II, & II** was $2400 \times 600 \times 120$ resulting in a total of $172.8M$ grid points. This was slightly increased later for **Papers IV & V** to a grid size of $2560 \times 640 \times 128$, i.e. $\approx 210M$ total grid points.

LES

In LES, the large flow structures are fully resolved while the motions at smaller scales are modeled. Therefore, a coarser grid could be used compared to that in the DNS which in turn reduces the computational cost. To do this, a filtering procedure is carried out on Eqs. 3.1 and 3.2. Such a filtering procedure on variable ψ is generally defined as follows (Pope, 2000):

$$\overline{\psi}\left(\mathbf{x},t\right)=\int G(\mathbf{r},\mathbf{x})\psi(\mathbf{x}-\mathbf{r},t)d\mathbf{r} \tag{3.3}$$

where normalization condition is satisfied by filter G i.e.,:

$$\int G(\mathbf{r},\mathbf{x})d\mathbf{r}=1 \tag{3.4}$$

Applying the filter on Eqs. 3.1 and 3.2 results in:

$$\frac{\partial\overline{u_i}}{\partial x_i}=0 \tag{3.5}$$

$$\frac{\partial\overline{u_j}}{\partial t}+\frac{\partial\overline{u_i u_j}}{\partial x_i}=-\frac{1}{\rho_c}\frac{\partial\overline{p}}{\partial x_j}+\nu_c\frac{\partial^2\overline{u_j}}{\partial x_i\partial x_j}+\overline{f_j} \tag{3.6}$$

The presence of the term $\overline{u_i u_j}$ in Eq. 3.6 is the key difference compared to Eq. 3.2. A tensor analogous to the Reynolds stress tensor is defined called the residual stress tensor:

$$\tau_{ij}^R=\overline{u_i u_j}-\bar{u}_i\bar{u}_j \tag{3.7}$$

τ_{ij}^R could be decomposed into anisotropic and isotropic parts ($\tau_{ij}^r=\tau_{ij}^R-\frac{2}{3}k_r\delta_{ij}$), where k_r is the residual kinetic energy and δ_{ij} is Dirac delta function. The isotropic part of τ_{ij}^R is considered inside a modified filtered pressure i.e., $\bar{p}\equiv\bar{p}+\frac{2}{3}k_r$. Using Eq. 3.7, one can rewrite Eq. 3.6 as follows:

$$\frac{\partial\overline{u_j}}{\partial t}+\frac{\partial\bar{u}_i\bar{u}_j}{\partial x_i}=-\frac{1}{\rho_c}\frac{\partial\overline{p}}{\partial x_j}+\nu_c\frac{\partial^2\overline{u_j}}{\partial x_i\partial x_j}+\overline{f_j}-\frac{\partial\tau_{ij}^r}{\partial x_i} \tag{3.8}$$

Various LES models exist which are different in terms of how they handle τ_{ij}^r i.e., subgrid-scales, to close Eq. 3.8. The dynamic Smagorinsky-Lilly model (Germano et al., 1991; Lilly,

1992) is used for the current study. Furthermore, SIMPLEC was used as the pressure-velocity coupled solver and the pressure and momentum terms discretization was carried out using bounded central differencing scheme. A three-level second-order implicit scheme was used for the time marching. A grid with total size of $1.85M$ grid cells was used. As investigated in **Paper II**, this grid resolution resulted in less than $10-20\%$ modeling of the turbulent kinetic energy in the entire domain which is in line with the guidelines in the literature (Pope, 2000).

RANS

In RANS, an averaging is carried out on Eqs. 3.1 and 3.2 which could be interpreted analogously to what is done in LES. Taking the mean ($\langle\cdots\rangle$) of Eqs. 3.1 and 3.2 results in (Pope, 2000):

$$\frac{\partial\langle u_i\rangle}{\partial x_i} = 0 \tag{3.9}$$

$$\frac{\partial\langle u_j\rangle}{\partial t} + \frac{\partial\langle u_i\rangle\langle u_j\rangle}{\partial x_i} = -\frac{1}{\rho_c}\frac{\partial\langle p\rangle}{\partial x_j} + \nu_c\frac{\partial^2\langle u_j\rangle}{\partial x_i\partial x_j} + \langle f_j\rangle - \frac{\partial\langle u_i'u_j'\rangle}{\partial x_i} \tag{3.10}$$

where $u_i' = u_i - \langle u_i\rangle$ is the velocity fluctuation vector. By defining the mean rate of strain tensor as $\langle S_{ij}\rangle = \frac{1}{2}\left(\frac{\partial\langle u_i\rangle}{\partial x_j} + \frac{\partial\langle u_j\rangle}{\partial x_i}\right)$ and removing the time derivative term, one can rewrite Eq. 3.10 as follows:

$$\frac{\partial\langle u_i\rangle\langle u_j\rangle}{\partial x_i} = \frac{\partial}{\partial x_i}\left[-\frac{\langle p\rangle\delta_{ij}}{\rho_c} + 2\nu_c\langle S_{ij}\rangle - \langle u_i'u_j'\rangle\right] + \langle f_j\rangle \tag{3.11}$$

With the extra unknown terms in Eqs. 3.9 and 3.11 i.e., Reynolds stresses ($\langle u_i'u_j'\rangle$), one should define new equations to close these sets of equations. This is what different RANS models do. RNG $k-\varepsilon$ model (Yakhot et al., 1992) was used with SIMPLE algorithm and second-order scheme for all discretizations.

Since the turbulence is entirely modeled through RANS, the grid size and the computational cost is considerably lower compared to those for the DNS and LES. This of course comes with considerable loss of information compared to the DNS and LES. Furthermore, due to the fact that the computational domain is sufficiently homogeneous in the spanwise direction, as also confirmed by the results of 3D-RANS simulations and comparing them to 2D-RANS, no considerable 3D effect was observed and 2D-RANS was deemed to be sufficient. Furthermore, unsteady RANS (URANS) did not provide any improvement to

the results either (The analyses of 3D effects and unsteadiness were done through comparing the profiles of first- and second-order statistics i.e., velocity, TKE, and dissipation rate of TKE profiles). The grid used for the 2D-RANS simulations had a total of 85000 grid cells.

Fig. 3.2 presents a schematic turbulent energy spectrum illustrating how DNS, LES, and RANS work in different ranges of wavenumbers. DNS resolves every possible scale while RANS models everything. Somewhere in between, LES resolves the scales larger than the corresponding cut-off wavenumber κ_{LES} while modeling the smaller scales. The choice of the cut-off wavenumber κ_{LES} determines how much of the turbulent kinetic energy is resolved by the LES. This is discussed in more detail in **Paper II.**

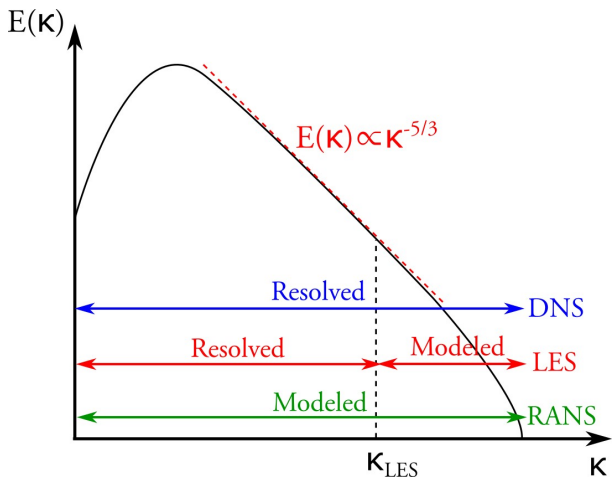

Figure 3.2: Comparison of DNS, LES, RANS in terms of the resolved and modeled wavenumber ranges

3.2.1 Boundary conditions

On the walls of the domain (gray planes in Fig. 3.1), no-slip condition is applied. Periodic boundary condition is applied in the spanwise direction i.e., to the sides of the outlet chamber (planes with no color). The width of the spanwise direction in the numerical study is $2h$ while in the real scale-up model used in the experiments, this is $10h$. The reasoning behind the shorter width in the numerical study was to decrease the computational cost by considering a periodic boundary condition. The investigations regarding the spanwise domain length is discussed in further details in **Paper I**.

In the oulet, for the DNS simulation, a convective outflow boundary condition (Orlanski, 1976) is applied to the streamwise velocity component for better stability and convergence (particularly in the beginning of the simulation). For the LES and RANS, a simple zero flux boundary condition is used since no convergence issues were observed as in the DNS.

Furthermore, preliminary tests showed no significant change in the results close to the outlet. Zero Dirichlet boundary condition is considered for the pressure in the outlet.

DNS inlet boundary condition

Implementation of the inlet boundary condition is a more challenging task due to the need for generating physical turbulence which could be developed in a short distance after the inlet (gap exit). The flow at the gap exit in an HPH valve is typically characterized by relatively high Reynolds number where the turbulent profile is not fully developed due to the shortness of the gap length. Furthermore, the velocity profile is typically skewed (compared to a symmetric channel flow profile) which is mainly due to the asymmetric geometry of the inlet chamber (cf. Fig. 3.1) leading to a "bouncing" effect on the upper wall of the gap.

Different approaches were considered for the purpose of generating flow conditions close to that at an HPH gap exit. Optimally, the flow in the inlet chamber and the gap could have been included in the computational domain. However, this would have considerably increased the computational cost. The other approach would have been to perform PIV measurements on the scale-up model with the same Reynolds number. But, this was not done due to the time and equipment limitations. Instead, the PIV measurements on a similar HPH scale-up model at a different Reynolds number is used (Håkansson et al., 2011). The main idea is to use the velocity and turbulent kinetic energy (TKE) profiles from a PIV measurement at the gap exit in a different scale-up model of a high-pressure homogenizer (with $Re = 27000$ and $U_g = 5.6$ m/s) and scale them for the scale-up model of the current study (with $Re = 2057$ for **Papers I, II, & III** and $Re = 2120$ for **Papers IV & V**), so that: i) the proper velocity and turbulence levels are obtained for the current design, and ii) a viable and physical turbulence is developed inside the outlet chamber.

The scaling of the velocity profile is rather straightforward. The velocity profile is proportionally scaled so that the required bulk velocity is obtained. However, scaling the turbulence through TKE is more challenging. To do so, we related the bulk velocity and shear Reynolds number through the definition of the skin friction coefficient (C_f) (White, 1999) as follows:

$$C_f = \frac{\tau_{wall}}{1/2\rho_c U_g^2} = \frac{u_\tau^2}{1/2 U_g^2} \tag{3.12}$$

where, τ_{wall} is the shear stress at the wall, C_f is the skin friction coefficient, and $u_\tau = \sqrt{\frac{\tau_{wall}}{\rho_c}}$ is the shear velocity. Using this equation, we can relate the quantities between the two flow conditions with different Reynolds numbers.

C_f is calculated using equations below (Dean, 1978):

$$C_f = 0.073 Re_{D_h}^{-0.25} \tag{3.13}$$

for turbulent regime, and:

$$C_f = \frac{12}{Re_{D_h}} \tag{3.14}$$

for laminar regime, where Re_{D_h} is the Reynolds number based on the hydraulic diameter. Laminar and turbulent flows are assumed in the case of $Re = 2120$ and $Re = 27000$, respectively. Using equations 3.13 and 3.14, friction coefficients, C_f, are obtained for each case.

Then, using Eq. 3.12, the shear velocity u_τ is obtained. However, to have comparable cases in terms of friction coefficient, we first need to obtain the bulk velocity in the case of the lower Reynolds number (e.g., $Re = 2120$ as in **Papers IV & V**), in the same channel as that of the PIV measurements (to have the Reynolds numbers based on the same hydraulic diameter). The value of U_g obtained from this assumption is calculated to be 0.43 m/s which then could be used in Eq. 3.12.

The ratio of u_τ to peak RMS velocities were taken from the empirical results of Tsukahara et al. (2005) and Bernardini et al. (2014) for comparable cases of Reynolds numbers which were then used to obtain the velocity fluctuations RMS values (u'_{rms}). A summary of the values of different variables in this process is provided in Table 3.1.

Table 3.1: The values used in the process of scaling the TKE profile at the gap exit (numerical domain inlet) from PIV measurements to the numerical simulations

	Re	Re_{D_h}	C_f	u_τ [m/s]	u'_{rms} [m/s]
PIV measurement	27000	50600	0.0049	0.28	0.782
Numerical study	2120	2830	0.0042	0.02	0.05

Therefore, the scaling factor for the TKE profiles of the two cases is obtained as follows:

$$\frac{k_{Num}}{k_{PIV}} = \left(\frac{0.05}{0.782}\right)^2 = 0.0041 \tag{3.15}$$

where k is the TKE, and indices *PIV* and *Num* represent the values related to the PIV measurement and the values to be used for the scaling purpose in numerical studies.

The next step is to use the TKE profile to generate the synthetic turbulent fluctuations at the inlet. Three different methods were tested for this purpose inside a numerical do-

main only consisting of the gap (cf. Fig. 3.1). Choosing the gap geometry was just a tool for comparing the performance of each turbulence generation method. First, white noises with amplitudes scaled with $\sqrt{\frac{2}{3}k_{Num}}$ were tested (with the assumption of isotropic turbulence). The second attempt was to use sinusoidal noises with tuned amplitudes to result in the closest possible TKE profile. However, the turbulence generated using these methods were not viable and was killed off after a short length downstream the inlet, no matter what the turbulent intensity was. But, the third approach which was the method of anisotropic synthesized turbulent fluctuation (Billson et al., 2003; Davidson and Billson, 2006; Davidson and Peng, 2013) provided promising results where sufficient synthetic turbulence levels at the inlet led to physical turbulent profiles in the downstream positions. The details of the implementation of this method is described in **Paper I**.

LES inlet boundary condition

For the LES, the same PIV-obtained velocity profile was used with the vortex method of Mathey et al. (2006) for the generation of synthetic turbulence at the inlet. The number of vortices was set to the recommended value of $N_c/4$ where N_c is the number of cells at the inlet. As discussed in **Paper II**, this change of method in the generation of synthetic turbulence at the inlet did not seem to change the physics of the problem as the turbulence inside the outlet chamber is dominantly controlled by the interaction of the wall-jet and the vortex above the jet i.e., the shear layer. Furthermore, the fact that the flow regime at the gap exit is in the laminar-transient regime makes another argument for the justification of this change of method from DNS to LES. Velocity and TKE profiles from the PIV are also used at the inlet for the RANS simulations.

3.2.2 Convergence study

The first step in the investigation of the breakup of drops was to generate the steady-state turbulent flow field inside the HPH outlet chamber. To investigate the convergence to a steady-state condition, the rolling average of the streamwise velocity component was calculated at a number of sample points as shown in Fig. 3.3. An instantaneous field of the streamwise velocity component is depicted in the figure to provide a sense of where the sampling points are located. Points 1-3 are located in the main jet body, point 4 is located in the recirculatory vortex just above the inlet (gap exit), and point 5 is located inside the strong vortex at the far point where the jet body ends.

The summation of absolute differences (SAD) was used as a measure of the sufficient window size for the rolling average (Wiktorski and Królak, 2020). Investigating SAD values as a function of window size shows that SAD converges to a constant value beyond a certain

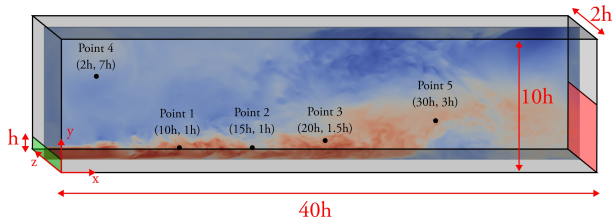

Figure 3.3: Numerical domain with the points where the convergence of the flow field is investigated. All points are located on the plane in the middle of the spanwise length. An instantaneous field of the streamwise velocity component is shown in the middle plane.

window size which is considered as the sufficient window size in performing the rolling average.

The flow field from a previous simulation (with plug flow profile as the inlet boundary condition with the same bulk velocity) was used as the initial flow field. The previous simulation was run for a long physical time of 1s. After rerunning the simulation with the new inlet boundary condition for 30 passage times ($t_{pass} = L_x/U_g$, where L_x is the channel streamwise length), the results of the rolling average procedure are presented in Fig. 3.4 (based on gap time-scale $t_g = h/U_g$), and show a good convergence of the streamwise velocity component at points 1-3 where the values are within 5% range of the final values. However, a steady-state seems to be harder to be achieved for points 4 and 5. The same observation was made even for the previous long simulation time of 1s. This is due to the slower dynamics of the vortices existing in those areas. Visual observations for a sufficiently long simulation showed that these vortices constantly go through a cycle of generation, being discharged through the exit or being dissipated, and regeneration. This process is much slower for the vortex at point 5 and faster for the vortex at point 4. A full description of this phenomenon is illustrated and discussed in **Paper I**.

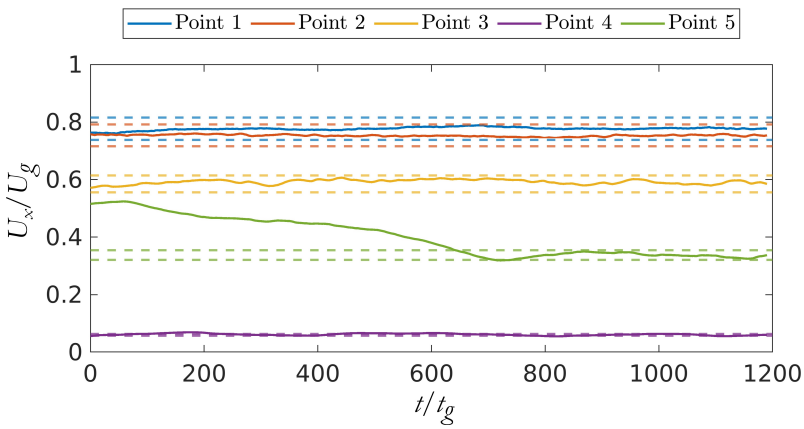

Figure 3.4: Rolling averages of streamwise velocity component at the five sampling points (cf. Fig. 3.3) (Reprinted from **Paper I** with permission.).

A similar procedure was followed for the LES single-phase study for which the details are provided in **Paper II**.

3.3 Two-phase DNS-VOF

3.3.1 Theoretical background

In the two-phase DNS, the flow is still solved based on the Navier-Stokes equations (Eqs. 3.1-3.2), but additional terms and equations should be added to account for the mutual impact of the disperse (drop) and continuous phases. To do so, a volume of fluid (VOF) method is used. A color function $H(\mathbf{x}, t)$ is defined where $H(\mathbf{x}, t) = 1$ if it is inside the disperse phase region; otherwise, $H(\mathbf{x}, t) = 0$. The VOF function, $\phi(\mathbf{x}, t)$, is then defined as the cell volume average of the color function $H(\mathbf{x}, t)$. The transport equation for the VOF function ϕ is then formulated as follows:

$$\frac{\partial \phi}{\partial t} + \frac{\partial u_i H}{\partial x_i} = \phi \frac{\partial u_i}{\partial x_i} \tag{3.16}$$

No changes are made to the mass continuity equation (Eq. 3.1), but the momentum equation (Eq. 3.2) needs some modifications. First, the density and the viscosity should now account for a mixture of the disperse and continuous phases. The new density and viscosity are now defined as:

$$\rho = \phi \rho_d + (1 - \phi)\rho_c \tag{3.17}$$

$$\mu = \phi \mu_d + (1 - \phi)\mu_c \tag{3.18}$$

Furthermore, the interfacial tension should also be considered. This force is defined as $F_i = \gamma \kappa_d n_i \delta$, where γ is the interfacial tension and δ is the 1D delta function at the drop interface approximated by $\delta \approx |\nabla \phi|$. Therefore, the momentum equation is then modified as:

$$\frac{\partial u_j}{\partial t} + \frac{\partial u_i u_j}{\partial x_i} = -\frac{1}{\rho}\frac{\partial p}{\partial x_j} + \nu \frac{\partial^2 u_j}{\partial x_i \partial x_j} + \frac{1}{\rho}\gamma \kappa_d n_i \delta \tag{3.19}$$

It is necessary to first determine the values of the color function $H(\mathbf{x}, t)$, normal vector n_i, and the curvature κ_d to solve the sets of equation 3.1, 3.16, and 3.19. The geometric

reconstruction of the color function $H(\mathbf{x}, t)$ is carried out using the method of multi-dimensional tangent of hyperbola for interface capturing (MTHINC) (Ii et al., 2012). This method and procedure is extensively used and explained in detail in other studies (Ii et al., 2012; Rosti et al., 2019).

3.3.2 Single drop injections

The procedure of the single drop breakup simulations is briefly described in this section. As discussed in **Paper III**, two geometries were used for these simulations: i) The HPH outlet chamber (cf. Fig. 3.1) where the turbulence is characterized as anisotropic and inhomogeneous (case "HPH"), and ii) a cubic domain with length $2\pi[-]$ with periodic boundary conditions on all sides in which homogeneous isotropic turbulence exists (case "ISO"). An in-house DNS-VOF code (Costa, 2018) was used for the numerical simulations which is extensively validated in various studies (Picano et al., 2015; Rosti and Brandt, 2017; Rosti et al., 2019).

For the time steps, a maximum Courant-Friedrichs–Lewy number of 0.25 is used for both cases. For the spatial resolution, 21 and 41 grid cells per initial drop diameter, D_0, were used in the HPH and ISO simulations, respectively. The grid size sensitivity investigations for the two-phase simulations are discussed in **Paper III**, where no significant difference was observed between the two spatial resolutions in terms of breakup morphologies and breakup time.

In the HPH cases, the injection of the drops are done after reaching a steady-state flow field (as discussed in section 3.2.2). Single spherical drops with initial diameters $D_0 = h/3$ are injected (by initializing the VOF field where VOF $= 1$ is set in the space occupied by the drop and VOF $= 0$ elsewhere) at position $(x, y, z) = (0.8h, 0.5h, 1h)$, located downstream the gap exit (cf. Fig. 3.3). The reason for the injection of the drops at this position was to ensure that the synthetic fluctuations generated at the inlet (due to the special inlet boundary condition used, cf. section 3.2.1) do not affect the injected drops. The simulation continues until the drop breakup is observed. Afterwards, the drop is removed from the field through clearing the the VOF field (all VOF values throughout the domain are set to zero). Furthermore, to remove any impact of the drop on the flow field, the single-phase flow is run for at least $180\tau_\eta$, where τ_η is the Kolmogorov time-scales, before another drop is injected again into the flow field.

In the ISO cases, drops with initial size $D_0 = 2[-]$ are injected at the center of the cube after the flow field is reached a steady-state. After the breakup of the drop, the VOF field is cleared and the single-phase flow is run to reach again a steady-state (to eliminate any residual impact of the drop on the flow) for at least $100\tau_\eta$.

The numerical investigations of single drop breakup in the HPH geometry are carried out to be compared to the experiments as well as the numerical ISO cases. This helps us to understand how the breakup in a non-idealized setup (inhomogeneous anisotropic turbulence) differs from that in an idealized setup (homogeneous isotropic turbulence). Consequently, they provide more insight into the breakup phenomenon in emulsification devices.

Chapter 4

4 Summary of results

This chapter serves as a summary of the results of the published papers. First, the results of the single-phase flow simulations are presented in section 4.1. In section 4.2, the results of the drop breakup studies for both the experimental (section 4.2.1) and the numerical (section 4.2.2) drops are presented. In section 4.3, the results are compared in two aspects. In section 4.3.1, the experimental and numerical results are compared. In section 4.3.2, the results of the drop breakup in the homogeneous-isotropic turbulence (HIT) and high-pressure homogenizer (HPH) are compared. Finally, in section 4.4 the impact of the turbulent flow field on the drops is investigated.

4.1 Single-phase flow

The behavior of the flow field inside the outlet chamber of the HPH determines a significant part of the physics controlling the interactions of the flow and the drops which will be injected into the flow field. Therefore, it was crucial to properly characterize the flow field.

This section summarizes the findings of the numerical studies on the single-phase flow and provides comparisons of the DNS, LES, and RANS as well as other similar studies.

4.1.1 Turbulent structures

Fig. 4.1 shows a snapshot of the vortical structures inside the domain visualized in the middle box with Q-criterion iso-surfaces as the visualization tool and colored by the streamwise velocity component normalized by the gap bulk velocity U_g. Behind the 3D visualization of the vortical structures, the normalized vorticity field is plotted as well to provide information regarding the vorticity values. The large vortex is observable in the distance $20h - 35h$. On the left-top corner of the outlet chamber, just above the inlet, where the

slower vortex resides (cf. point 5 in Fig. 3.3), no strong vorticity is observed which explains the slow dynamic behavior of the recirculatory structures appearing in that region.

Another observation is that the instability at the shear layer begins at a distance of about $x = 2.5h$. Stronger and more coherent vortices appear at downstream positions around $x = 7h - 18h$. These strong vortices are expected to interact with the drops in this region and potentially leading to their breakup. This is consistent with the results of the drop breakup positions in section 4.2.

Furthermore, in Fig. 4.1, the vortical structures inside the inner layer of the jet (at positions where $y/h < 0.2$) are also visualized. These structures start to appear after $x = 2h$, but more coherent structures start at positions $x > 8h$ which is consistent with what is observed in other studies of confined jets (Naqavi et al., 2014).

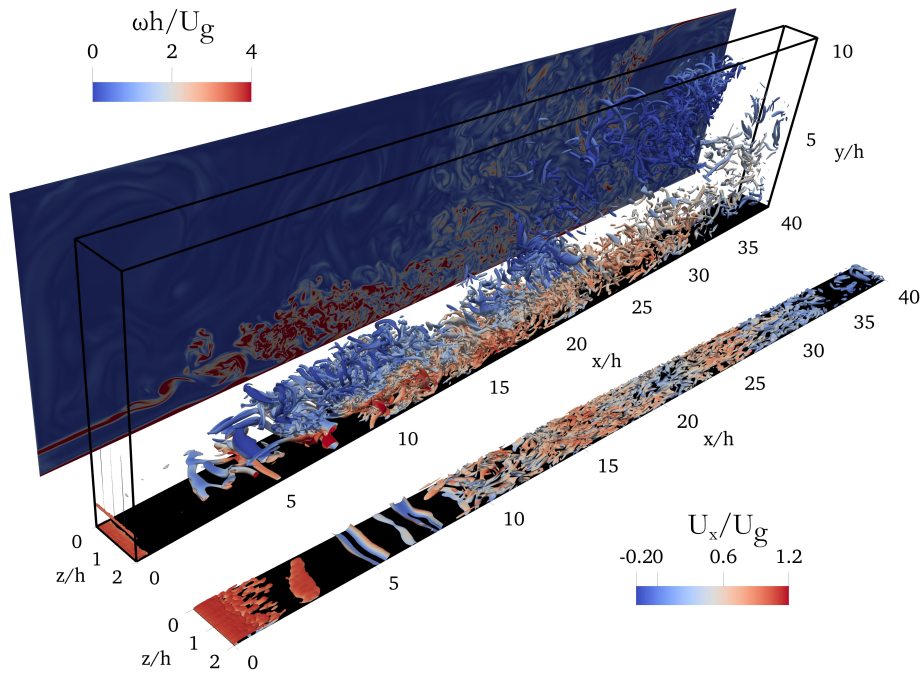

Figure 4.1: Visualization of 3D vortical structures through Q-criterion iso-surfaces colored by the normalized streamwise velocity component (U_x/U_g) (Reprinted from **Paper I** with permission).

4.1.2 General flow field behavior

Large Eddy Simulation (LES) and Reynolds-averaged Navier-Stokes (RANS) are considerably computationally cheaper compared to DNS and therefore, are more favorable in the industry for the simulation of turbulent flows. This, of course, comes with the loss of information in the smaller turbulent scales. Hence, it was important to quantify this loss

of accuracy and evaluate how much of the turbulence information could be captured by either of these turbulence models, having the DNS as a benchmark for validation.

Fig. 4.2 provides a comparison of the averaged (temporally and spatially in spanwise direction) velocity magnitude fields for the DNS, LES, and RANS with the red vectors showing the direction of the local averaged flow. The results show that LES have properly captured the two main vortex structures inside the domain at approximate positions $(x/h, y/h) = (25, 5.5)$ and $(x/h, y/h) = (4, 6)$ with slight differences compared to what DNS results show. RANS has also predicted such structures, but in more stretched shapes with larger differences in terms of the position of the vortex center. This is more prominently evident for the left vortex where RANS shows an approximate position of $(x/h, y/h) = (5, 9)$.

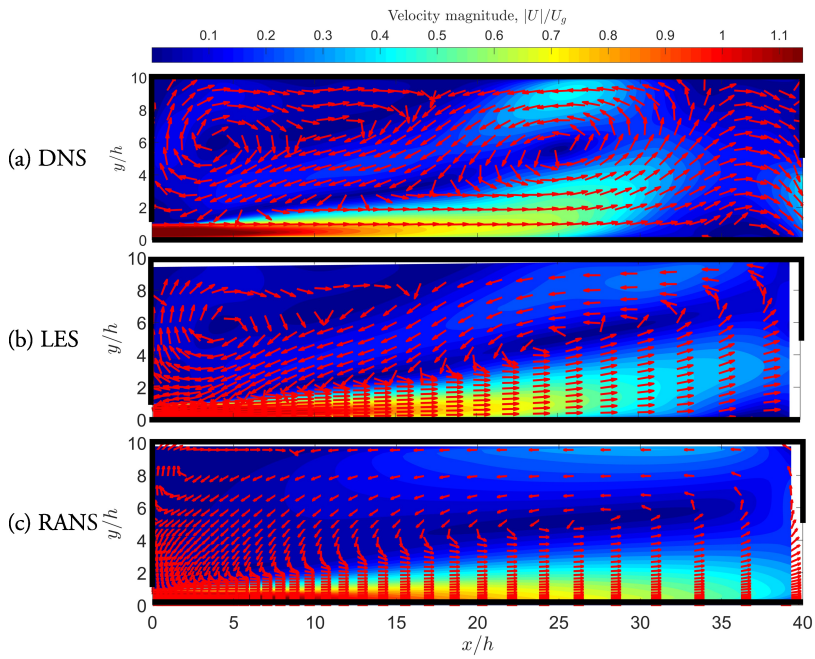

Figure 4.2: Comparison of the averaged (in time and spanwise direction) velocity magnitude field normalized by the gap bulk velocity ($|U|/U_g$) for (a) DNS (Validation data), (b) LES, and (c) RANS. The red vectors show the local direction of the averaged flow field) (Reprinted from **Paper II** with permission).

4.1.3 Wall-jet characteristics

One characteristic of the flow field in the HPH outlet chamber is the confinement of the domain which leads to a somewhat different behavior compared to a non-confined wall-jet. As discussed before, the confinement of the domain creates a recirculatory vortex just above the jet which pushes the jet further towards the wall. To characterize the flow field in the outlet chamber of an HPH, it was important to compare the characteristics of such

a wall-jet to a non-confined setup. To do so, two parameters were studied: i) Jet half-velocity width $y_{1/2}$, where the local streamwise velocity is equal to $0.5U_{max}$, U_{max} being the maximum local jet velocity, and ii) The spreading rate of the jet defined as:

$$S = \frac{dy_{1/2}(x)}{dx} \tag{4.1}$$

Fig. 4.3 illustrates how the jet half-velocity width $y_{1/2}$ develops in the streamwise direction and compares the results of the current study with a number of relevant studies. Also, the spreading rate could be analyzed through the same figure by looking at the slopes of the curves (see Eq. 4.1). For both DNS and LES, $y_{1/2}$ is observed to be monotonically increasing but with different rates. However, for RANS, the spreading rate decreases at further downstream positions closer to the outlet ($x/h > 18$), which again reflects the inability of RANS in accurately predicting the large vortex structures and their interactions with the jet (as discussed in Fig. 4.2). Different spreading rates are identified at three different regions in the streamwise direction: i) $x/h < 8$, ii) $x/h = 8 - 18$, and iii) $x/h > 18$. The values of the spreading rate are provided for the DNS, LES, and RANS in Table 4.1.

Table 4.1: Spreading rates of the jet at different streamwise regions for DNS, LES, and RANS simulations.

	$3 < x/h < 8$	$8 < x/h < 18$	$18 < x/h < 30$
DNS	0.052	0.100	0.260
LES	0.038	0.084	0.196
RANS	0.034	0.083	0.068

A somewhat similar trend is observed for the experimental study of Innings and Trägårdh (2007) on a free jet in a different HPH scale-up model outlet chamber. They reported that the spreading rate doubled at positions $x/h > 8$ compared to the upstream positions ($x/h < 8$).

Ahlman et al. (2007) performed a DNS on a wall-jet with confined geometry. However, they used a co-flow stream above the shear layer to wash the large-scale structures from the domain. Therefore, their case could be considered close to a non-confined wall-jet geometry. Ahlman et al. (2007) reported a constant spreading rate of $S = 0.068$. Compared to the results for the confined wall-jet of the current study, this shows a higher spreading rate at regions $x < 8h$ and lower spreading rate at regions $x > 8h$. Comparing the half-velocity width of the two cases in Fig. 4.3 shows that the jet in the confined case of the current study is at a lower position until it reaches the same width at around $x = 18h$. Beyond this position, the impact of the large vortex is clearly observed as the spreading rate increases with a factor of 2. As it will be discussed later in section 4.2, no drop breakup is observed beyond $x = 18h$ and therefore, no impact is expected by the large vortex beyond this position on the drops.

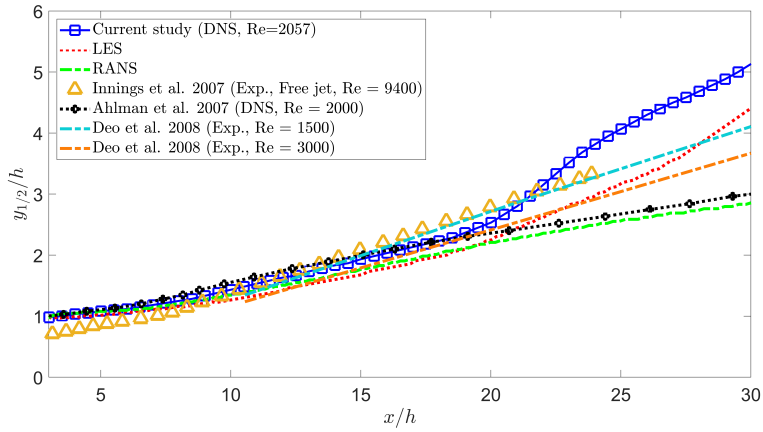

Figure 4.3: Comparison of the jet half-velocity width $y_{1/2}$ in the streamwise direction for the current and similar studies (Adopted and modified from Fig. 10 in **Paper I**).

Furthermore, the experimental studies of Deo et al. (2008) showed how increasing the Reynolds number results in a decrease in the spreading of the jet. The results show that the spreading of the jet in the current study lies between the two cases of Deo et al. (2008) with $Re = 1500$ and $Re = 3000$ which is expected as the Reynolds number of the current study also lies between these two Reynolds numbers. More comparisons with other studies are available in **Paper I**.

4.1.4 Velocity profiles

Fig. 4.4 provides a more detailed analysis by providing the averaged streamwise velocity profiles at positions $x/h = 8, 12, 16$ which are relevant positions for the breakup of drops. At $x/h = 8$, LES shows a good agreement with the DNS, particularly in terms of predicting the backflow vortex structure (represented by negative values in the range $2 < y/h < 7$). However, RANS only predicts a weak backflow (negative values) at $y/h > 7$. Similar observation is also made for the positions $x/h = 12$ and 16. However, focusing more on the jet region i.e., $y/h < 2$ as the more relevant region for the breakup of drops, the LES performance does not seem to be superior to that of the RANS. Except for the jet maximum velocity, RANS actually seem to comply more with the validation data (DNS). Of course, this does not necessarily mean to be a general conclusion, but it appears that RANS has, at least, performed as good as LES in the regions of interest for the breakup of drops in our confined wall-jet setup.

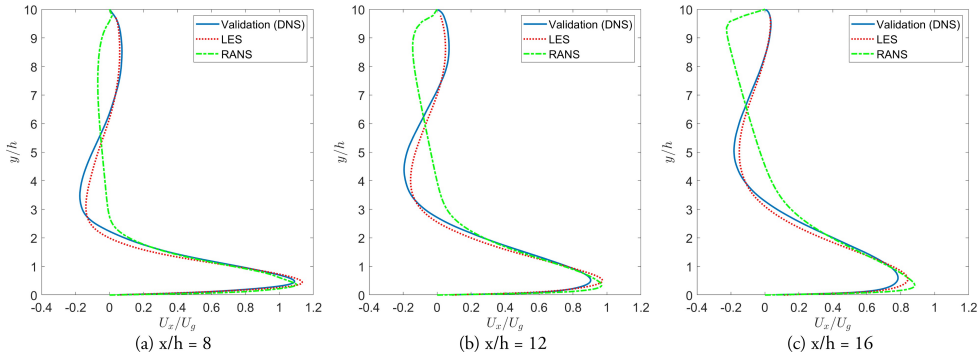

Figure 4.4: Comparison of the averaged streamwise velocity profiles normalized by the gap bulk velocity (U_x/U_g) at three streamwise positions (a) $x/h = 8$, (b) $x/h = 12$, and (c) $x/h = 16$ (Adopted and modified from Fig. 6 in **Paper II**).

4.1.5 Dissipation rate of TKE

The dissipation rate of TKE is another parameter of interest which is of great importance in the study of drop breakup as it is one of the parameters which controls the Weber number (cf. Eq. 2.4). Fig. 4.5 shows the averaged (temporally and spatially in spanwise direction) field of dissipation rate of TKE normalized by the gap bulk velocity and gap height ($\varepsilon/(U_g^3/h)$) for DNS, LES, and RANS. Both LES and RANS (Fig. 4.5b-c) have underpredicted the extent of the dissipative region inside the shear layer compared to that of the validation data of DNS (Fig. 4.5a). In terms of the maximum global value (which occurs for all cases at positions $x/h < 7$), the relative errors are $+4\%$ and -41% for the LES and RANS, respectively.

A more detailed investigation of the dissipation rate of TKE profiles in further downstream positions (more relevant for breakup) is carried out and the results are presented in Fig. 4.6. At $x/h = 8$, two local maxima are observed for all cases, but the one inside the shear layer is the one which will interact with the drops. Moving to further downstream positions, the maximum values decrease, the profiles change towards more uniform values, and LES and RANS results get closer to that of the DNS. In terms of the local maximum dissipation rates, the relative errors for the LES are 13%, 7.8%, and 2.5% at streamwise positions $x/h = 8$, 12, and 16, respectively. The same trend is observed for the RANS, but with relatively larger errors i.e., 41%, 30%, and 10%.

The results show that LES does have a closer prediction to the validation data (DNS), but RANS results are not far from DNS results as well. Considering the limitations of a 2-equation RANS model (particularly with curved streamline which is dominantly present in the flow field of interest) but considerably lower computational cost (0.1% and 0.03% of computational time of LES and DNS, respectively), RANS could be considered as a very fast estimation of the dissipation rates inside the outlet chamber of a typical HPH.

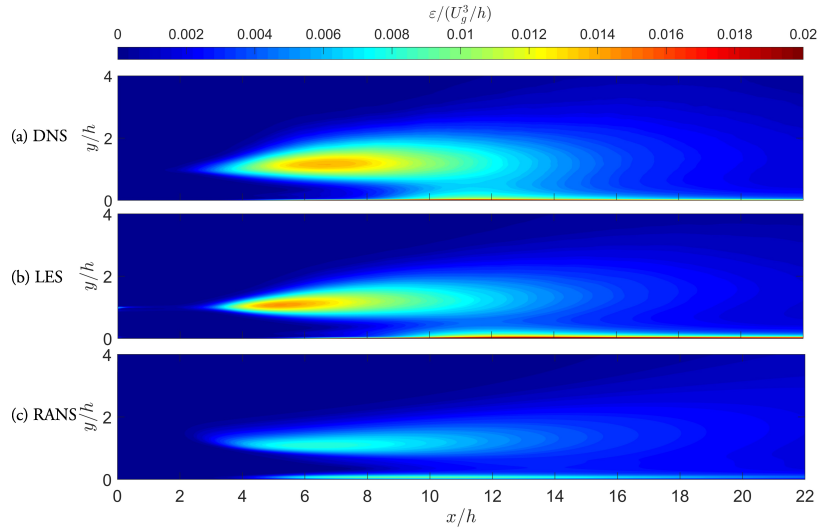

Figure 4.5: Comparison of the averaged dissipation rate of turbulent kinetic energy field normalized by the gap bulk velocity and gap height ($\varepsilon/(U_g^3/h)$) for (a) DNS (Validation data), (b) LES, and (c) RANS (Reprinted from **Paper II** with permission).

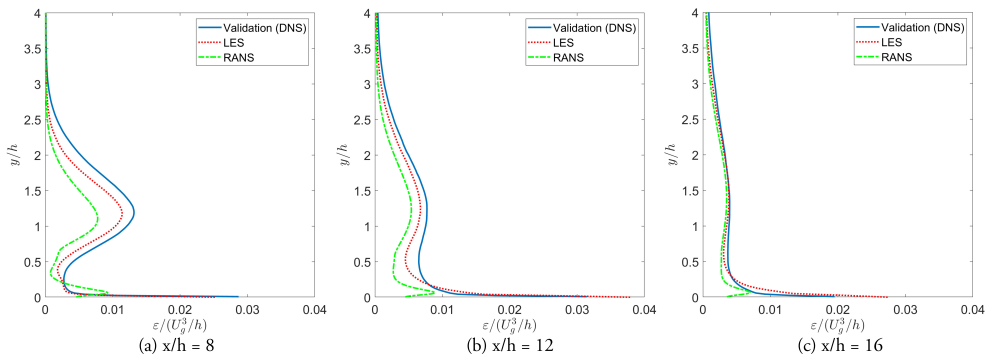

Figure 4.6: Comparison of the averaged dissipation rate of turbulent kinetic energy profiles normalized by the gap bulk velocity and gap height ($\varepsilon/(U_g^3/h)$) at three streamwise positions (a) $x/h = 8$, (b) $x/h = 12$, and (c) $x/h = 16$ (Adopted and modified from Fig. 9 in **Paper II**).

Furthermore, using a characteristic dissipation rate of TKE (values averaged in a rectangular area in the range $0 < x/h < 20$ and $0.5 < y/h < 2.5$) and using it in a population balance equation (PBE) framework showed very close predictions of the Sauter mean diameter (D_{32}) of the fragment size for the LES and RANS with $+24\%$ and $+22\%$ relative errors, respectively, compared to that of the DNS. The details of this investigation is available in section 3.3.3, **Paper II**.

4.2 Single drop breakup

A primary objective of this PhD work was to investigate the turbulent breakup of drops inside the scale-up HPH model (cf. Fig. 3.1). This is carried out through two approaches: i) Experimental approach where high-speed photography was used to visualize the breakup of drops, and ii) Numerical approach where a DNS-VOF framework was used to simulate the turbulent breakup of the drops.

Both approaches have their own limitations. The experimental approach through 2D photography introduces uncertainties regarding the breakup events that might occur in the plane normal to the image plane. The numerical approach also comes with limitations in terms of high computational costs. To reduce this cost, compromises are made in terms of grid resolution which might lead to uncertainties in terms of the exact point and time of the breakup. Therefore, an investigation through the two methods seems to be a promising approach to compensate for these limitations.

The results of this section are investigated at a characteristic Weber number $We = 82$ based on the dissipation rate of TKE definition of Eq. 2.6. In what follows, the results of the experimental and numerical studies are provided in sections 4.2.1 and 4.2.2, respectively.

4.2.1 Experimental drop breakup

The visualization of three sample drops from the experimental approach is provided in Fig. 4.7. In the top-left corner, the trajectories of each drop is plotted on top of the normalized dissipation rate of TKE field (time- and spanwise-averaged) as a tool for providing information regarding the relative location of the drops with respect to the dissipative region inside the shear layer. The dissipation rate field is obtained from the numerical solution of the flow field. In the top-right corner, the circularity of each drop (normalized by the value of the initial circularity i.e., $C_{(x=0)}$) is plotted. The square markers show the last point plotted. The circularities are plotted up to one time-step before the breakup while the trajectories are shown up to the point of breakup. This is to avoid false interpretation of circularity at the instance of breakup since the circularity is calculated for a single drop and not two separated drops. Different instances of the drop visualizations are illustrated at approximate streamwise positions (designated by the position axes). The movement direction of the drops visualizations are similar to the plane of the trajectories plot (from left to right). Due to visualization limitations for larger drops, the red arrows in the latest stages of the drops deformations point to the positions of the drops in those instances. The three drops are chosen to represent different breakup morphologies observed in the experiments.

Starting with the first drop (Drop 1), we observe that the drop does not significantly deform and maintains its spherical shape until about $x/h = 10$. This is also reflected by the

value of circularity staying close to 1 until this position. Beyond this position, the drop starts to stretch in the horizontal direction. Just after $x/h = 12$, the drop relaxes into a relatively spherical shape again, but then gets pulled in the vertical direction. This leads to the formation of two bulbs which are finally separated at the neck formed between them at position $x/h = 14.4$.

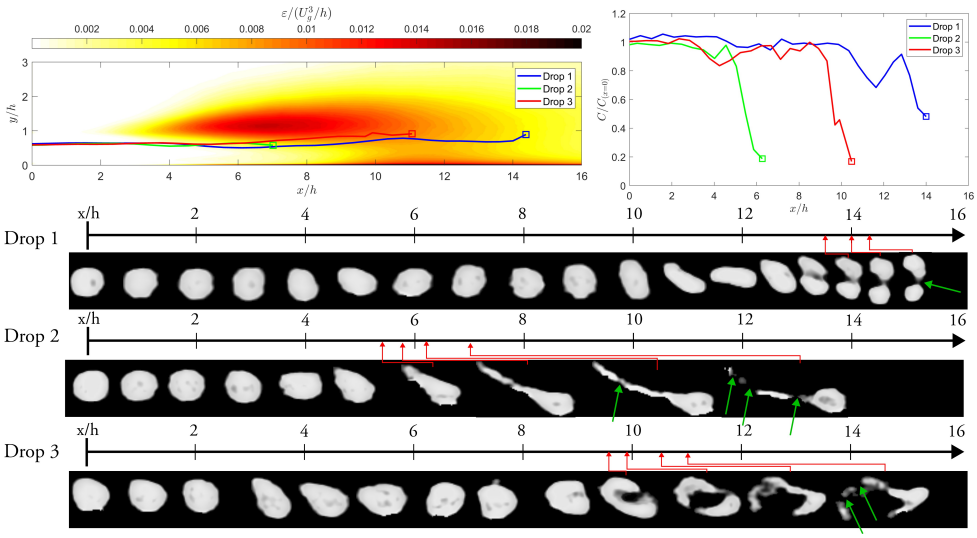

Figure 4.7: Three sample experimental drops with plots of corresponding trajectories on top of the dissipation rate of TKE field (top-left) and circularities (top-right). The green arrows point to the approximate position of the initial breakup. The red arrows show the streamwise position of the drop geometric center for the late stages of drop deformation due to space limitations for visualizing large drops.

Drop 2 also shows a similar behavior, but breaks at an earlier position. No significant deformation is observed up to about $x/h = 4$. But, beyond this position, a rapid stretching of the drop occurs in a distance of $2h$. The left part of the drop stretches into a thread-like shape while the larger portion of the drop forms a bulb on the right. Finally, breakup occurs at $x/h = 7$ inside the thread. At the instance captured after the breakup, various points of breakup is detected, but this seems to be due to the limitation of the camera to capture the exact moment of breakup and therefore, detecting the exact point of initial breakup.

Drop 3 stays spherical for a longer distance up to about $x/h = 9$. A more complex deformation seem to happen which is not quite detected by the measure of circularity i.e., a deformation of the drop is evident at $x/h = 10$ by looking at the visualizations, where a hole seems to form inside the drop, but the circularity stays close to 1. At about $x/h = 10.5$, a more diffused type of deformation morphology is observed at the top-left part of the drop and finally at about $x/h = 11$, the breakup occurs in that region instead of a single point.

4.2.2 Numerical drop breakup

After resolving the single-phase flow inside the HPH outlet chamber, the flow field is ready for the injection of the drops, as a second phase, to investigate the deformation and breakup of the drops in the numerical framework.

Fig. 4.8 provides visualizations of three sample numerical drops. The iso-surfaces of $VOF = 0.5$ are used in all visualizations of the numerical drops to visualize the drop interface. This figure is analogous to Fig. 4.7 for experimental drops with the same information (trajectories on top of the time- and spanwise-averaged dissipation rate of TKE field in the top-left, circularity plots in the top-right, and visualizations of the drop at different instances in the bottom with position axes). Furthermore, the direction and orientation of the drops are in accordance with the trajectories plot which helps with understanding the position and orientation of the drop with respect to the dissipative region of the shear layer.

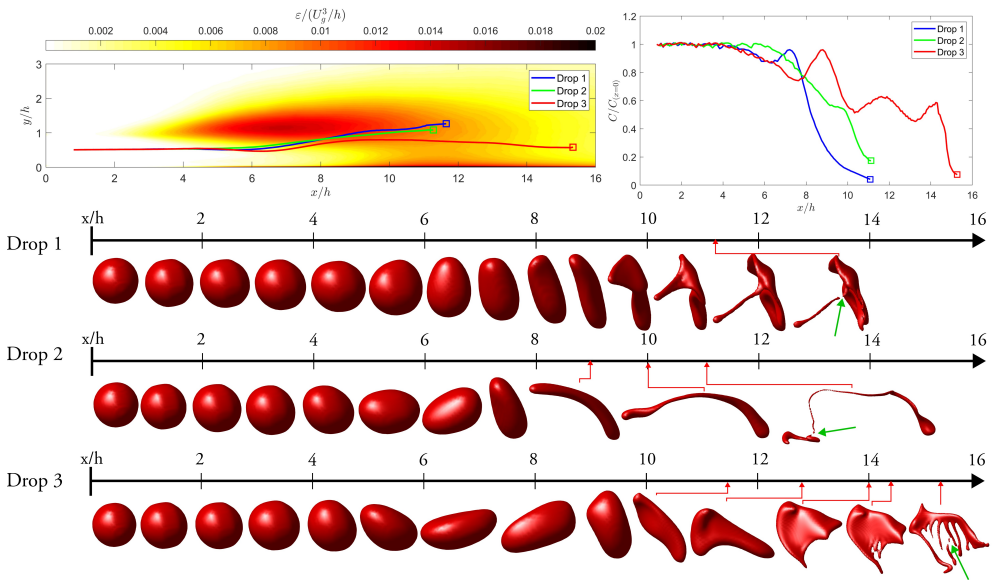

Figure 4.8: Three sample numerical drops with plots of corresponding trajectories on top of the dissipation rate of TKE field (top-left) and circularities (top-right). The green arrows point to the approximate position of the initial breakup. The red arrows show the streamwise position of the drop geometric center for the late stages of drop deformation due to space limitations for visualizing large drops.

Drop 1 keeps its spherical shape until $x/h = 4$. A slight stretching occurs in the horizontal direction which then quickly relaxes into spherical shape and stretches again in the vertical direction. About $x/h = 9.5$, a small neck starts to appear on the left side of the drop which then gets thinner until breakup occurs at a single point in the neck at position $x/h = 11.3$.

Drop 2 shows a monotonous decrease in circularity beyond $x/h = 6$ where the drop starts stretching in the horizontal direction. The long neck/thread gets very thin until it breaks

at a single point at position $x/h = 11$.

Drop 3 shows a more oscillatory behavior in terms of circularity. The drop first starts deforming just after $x/h = 4$. The deformation starts as stretching in the horizontal direction until $x/h = 8$ where the stretching changes in the vertical direction. Then again at about $x/h = 9$ the drop stretching changes to the horizontal direction. Beyond this position, the drop interface deforms into a thin sheet. Finally, at $x/h = 15.3$ the sheet ruptures chaotically with no single point detectable as the initial breakup point.

4.3 Comparisons

This section provides a summary of the comparison studies on the drop breakup investigations. First, section 4.3.1 provides a comparison of the experimental and numerical studies of the drops breakup inside the HPH outlet chamber at a characteristic Weber number of $We = 82$. The experimental and numerical results are compared both qualitatively and quantitatively. This section serves as a summary of the results provided in **Paper IV**.

In section 4.3.2, the results of the numerical drop breakup inside the HPH outlet chamber is compared to the results of the study on drop breakup in an ideal homogeneous isotropic turbulence (HIT) at 3 different characteristic Weber numbers $We = 1, 5$ and 96. This section provides a summary of the results which are published in **Paper III**.

4.3.1 Experimental vs. numerical

Different comparison tools are needed to compare the results of the experimental and numerical studies of drop breakup. Since it is practically impossible to create exactly the same turbulent flow field and therefore exactly the same drop deformation sequences, the results of the two studies are compared both in a qualitative and a statistically quantitative manner.

The first tool is the qualitative comparison of the breakup morphologies observed in the studies. The drops in both studies are manually and individually investigated to identify similarities and differences.

Fig. 4.9 illustrates one of the breakup morphologies observed both in the experiments and the numerical studies. In both cases, the drop is deformed, stretched, and finally broken at a single detectable point. In such a breakup morphology, the extent of stretching and thinning of the drops might be very different, but the common characteristic of this type of morphology is that a single initial breaking point could be detected.

Another type of breakup morphology detected in both the experiments and the numerical studies is presented in Fig. 4.10. In both cases, the drop is deformed and broken in a more

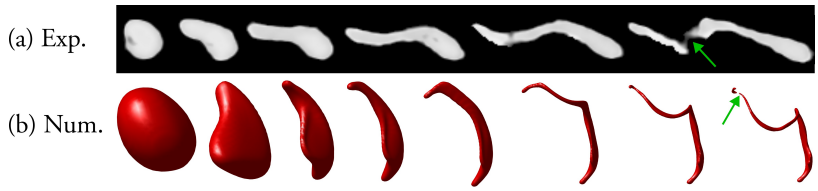

Figure 4.9: Single-point breakup morphology for (a) Experimental drop, and (b) Numerical drop. The green arrows show the initial breakup point.

diffused breaking region rather than a single point. In this type of breakup morphology, it is evident from the numerical cases that the drop (partially or entirely) deforms into a thin sheet and the initial breakup starts as a rupture in that thin sheet. Due to limitations of the experimental approach (both image resolution and the lack of information in the 3rd dimension normal to the visualization plane), it is difficult to have the same observation in the experiments. However, by looking at the snapshots of the drop in the frames after the initial breakup e.g., the last frame in Fig. 4.10a, it is evident that the drop breaks in a chaotic manner at multiple locations where each detached part moves separately after the breakup event.

Figure 4.10: Diffuse breakup morphology for (a) Experimental drop, and (b) Numerical drop

Borderline morphologies are also observed in both approaches as illustrated in Fig. 4.11 where the characteristics of both above-mentioned morphologies are observed in the breakup sequences of the experimental and the numerical drops. In the experimental drop, a diffused region of breakup is formed in the middle of the drop in the sixth frame which is similar to the morphology observed in Fig. 4.10. However, in the subsequent frame, a single point of breakup is observed on the left side of the drop which is similar to the behavior in Fig. 4.9. The same behavior is also observed in the numerical drops with Fig. 4.10b as an example. In the fourth frame, it is observed that a neck is formed on the left side while the other portion of the drop deforms into a thin sheet. These deformations further develop until a single-point breakup occurs in the neck while a sheet rupture (diffused breakup morphology) is observed in the other portion of the drop.

What was discussed in the previous paragraphs showed the similarities of the experimental and numerical approaches in terms of predicting the breakup morphologies. However, differences are also observed. As illustrated in Fig. 4.12, a few drops in the experiments show a type of binary breakup morphology in which two daughter drops with almost the

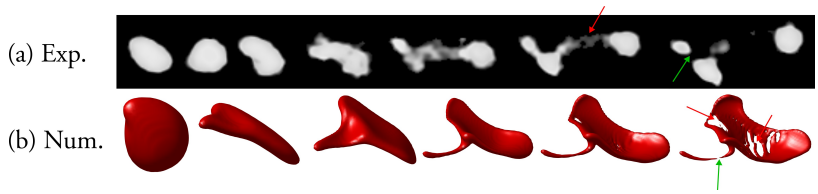

Figure 4.11: Borderline breakup morphology for (a) Experimental drop, and (b) Numerical drop. The green arrows show the single initial breakup point while the red arrows point to the diffused region of breakup.

same size are generated. Although this could also be categorized as a single-point breakup morphology which was also observed in the numerical approach, the daughter drops in the numerical approach are mostly different in size and not comparable to those in a binary breakup.

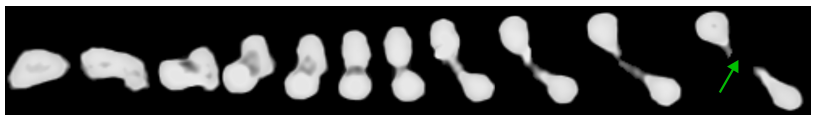

Figure 4.12: Bulb breakup morphology for an experimental drop

A more quantitative approach is also taken to compare the numerical and experimental studies of the drops breakup.

Fig. 4.13 illustrates the trajectories of the drops for the numerical and the experimental approaches. The squares at the end of each trajectory show the corresponding breakup positions. Furthermore, the green rectangles show the extent of the breakup region for all the drops in each of the numerical and the experimental approaches. No significant difference is observed for the breakup positions in the y-direction ($y/h = 0.29 - 2.04$ and $y/h = 0.22 - 2.02$ ranges are observed for the numerical and experimental drops, respectively.). However, in the x-direction, a wider region is observed for the case of experimental drops. The experimental drop breakup events occur at positions $x/h = 5.27 - 18.04$ while the numerical results suggest breakup positions at $x/h = 7.3 - 15.34$.

Fig. 4.14 compares the mean streamwise positions of the numerical and the experimental drops at different circularity levels (designated as x_{C_n} where n is equal to the different circularity values) and at the initial breakup position ($x_{breakup}$). The error bars show the 95% confidence intervals. The circularity level $C = 0.67$ is taken as a measure for the beginning of the substantial deformation of the drops. This level was obtained through manual investigation of the results. By starting at $C = 0.67$ and moving towards higher deformation levels until the breakup, we could get insight into how the drops deformations progress (the beginning of the deformation, how fast the deformations happen, and when the breakup happens) in the two approaches. At all circularity levels and at the breakup, it is observed that the numerical approach predicted later positions compared to those of the experi-

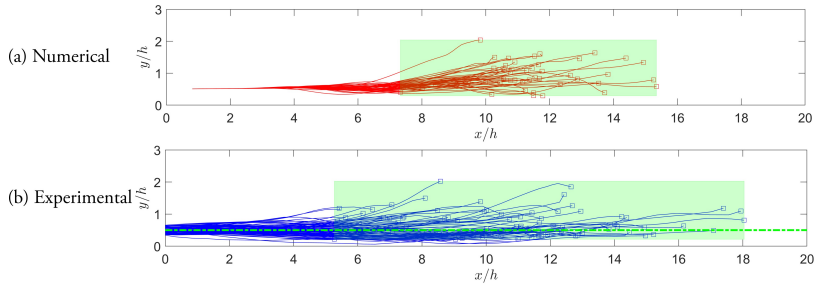

Figure 4.13: Trajectories of (a) Numerical and (b) Experimental drops. The squares show the breakup positions. The green regions show the breakup position spans. The green dashed line in the case of experimental drops show position of the middle of the gap height.

mental approach. However, the 95% confidence intervals are overlapping, implying that there is no statistically significant difference between the two methods at the 5% level.

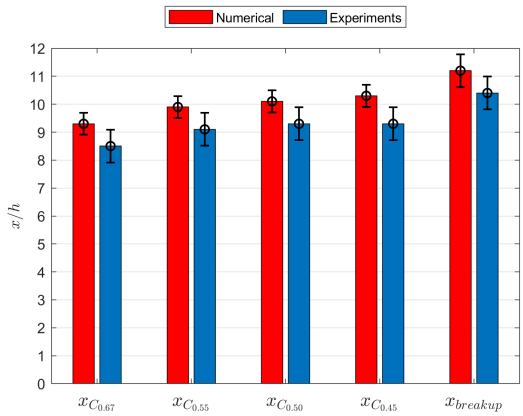

Figure 4.14: The mean streamwise positions for the numerical and experimental drops at different circularity levels (x_{C_n}, where $n = 0.67, 0.55, 0.5$, and 0.45) and at the breakup position ($x_{breakup}$) with the error bars showing the 95% confidence intervals (Reprinted from **Paper IV** with permission).

A better understanding of the distribution of the breakup positions is provided through the PDF of the breakup positions as illustrated in Fig. 4.15. This figure shows that in both the numerical and the experimental approaches, the most likely breakup position is at range $x/h = 10 - 12$. However, a difference is also observed. In the experiments, breakup events are observed in the ranges as early and as late as $x/h = 4 - 6$ and $x/h = 16 - 20$, respectively. This is not so for the numerical drops.

Another difference between the two datasets is in terms of breakup probability. All the numerical drops (51 drops) break resulting in a breakup probability of 100% with 95% confidence interval $[93 - 100\%]$. However, 82% of the experimental drops (88 out of 107) are broken (with 95% confidence interval $[74 - 89\%]$).

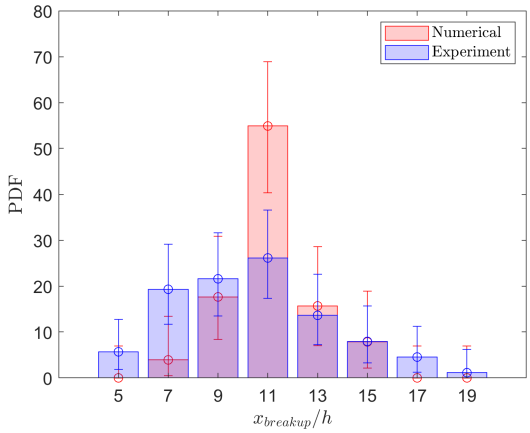

Figure 4.15: PDF of the breakup positions for the numerical and experimental drops. The error bars show the 95% confidence intervals (Reprinted from **Paper IV** with permission).

In summary, the numerical and the experimental approaches are generally in good agreement in terms of predicting the morphologies and mean breakup positions. However, differences are also observed and the possible underlying reasons for these differences should be addressed.

The first hypothesis for the observed differences was the uncertainties in terms of the Weber number in the experiments. While the physical properties are set as constant inputs in the numerical simulations, uncertainties exist in the real world i.e., experiments. Using the method of the propagation of uncertainties on Eq. 2.4 (as discussed in details in **Paper IV**, section 2.4) showed that there is a $\pm 16\%$ uncertainty in the value of the Weber number compared to the numerical simulations i.e., Weber number could be varying in the range $[69 - 96]$. However, performing simulations with three Weber numbers 69, 82, and 96 and comparing the results in terms of breakup morphologies and positions showed no significant difference. Therefore, the hypothesis that the differences might be due to the uncertainties of the Weber number is rejected.

The second hypothesis was that the loss of information in the 2D imaging in the experiments might lead to the loss of information in the 3rd dimension (the plane normal to the imaging plane) and result in some difference between the numerical and experimental results. To test this hypothesis, the numerical results were investigated in both 2D and 3D (2D investigation of the numerical results included performing the same image-processing procedure as that of the experimental approach on the projection of the drops images on the 2D plane). Although investigating the drops deformation in 2D might arguably lead to difficulties in determining the exact morphology of the breakup, only small differences were observed in terms of breakup position (a $0.1h$ difference in the mean values of breakup position). Therefore, this is not expected to considerably affect the main conclusions of the

study.

The third hypothesis was that the slight differences in terms of the injection points and the initial circularity of the drops could lead to further differences observed between the two datasets. Although the filtering process in the image-processing (cf. section 2.3.2) ensures that the initial injection positions and circularities of the experimental drops are not far from those of the numerical drops, slight differences (introduced by the permissible errors as an input to the filtration process) might still lead to differences in the final results. This was inevitable since we had to find a balance between using narrower filters (to get closer to the numerical drops initial states) and having fewer drops for the statistical analyses. Fig. 4.16 provides a clear image of how the difference in the trajectories of the drops affects the breakup positions. The experimental drops are divided into three groups: The drops which break early ($x/h < 8$), the drops breaking late ($x/h > 14$), and the drops which do not break at all. The normalized dissipation rate of TKE field (time- and spanwise-averaged) is also plotted to provide information regarding the position of the high-dissipation regions with respect to the trajectories. It is evident in Fig. 4.16a that when the drops pass through the highly dissipative shear layer, the breakup at an early position inside the shear layer is almost certain. On the other hand, as suggested by Figs. 4.16b-c, when the drops bypass this region, they either break at much later stages or do not break at all (the trajectories in Fig. 4.16c are cut due to the entrance of another drop in the domain. But, the drops are manually inspected and ensured that they do not break until they exit the field of view). Therefore, differences in the injection points of the drops affect the trajectories and consequently the breakup positions.

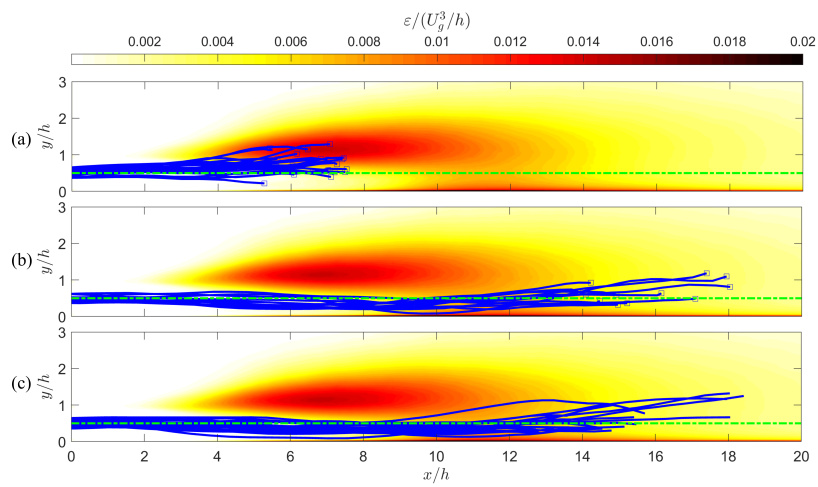

Figure 4.16: The trajectories of the experimental drops on top of the time- and spanwise-averaged dissipation rate of TKE field normalized by U_g^3/h, divided into three groups: (a) drops with early breakup positions ($x/h < 8$), (b) drops with late breakup positions ($x/h > 14$), and (c) drops not breaking (Reprinted from **Paper II** with permission).

Fig. 4.17 provides a more statistical view on the impact of the initial injection position

and circularity. Fig. 4.17a compares the PDF of the breakup positions of the experimental drops based on their injection position and compares that to those of the numerical study. The results show that the drops injected closer to the gap centerline (green bars), where the numerical drops are injected, leads to narrower breakup position distribution i.e., closer to the numerical drops distribution. Furthermore, as the injection points get farther from the gap centerline (red bars), the breakup distribution gets skewed more towards left i.e., earlier breakup positions are observed.

An analogous investigation is carried out on the initial circularity values. More skewness to the left (higher probability for earlier breakup positions) is observed for the red bars representing larger initial circularities while more spherical drops (green bars) have a generally closer distribution to the numerical drops distribution.

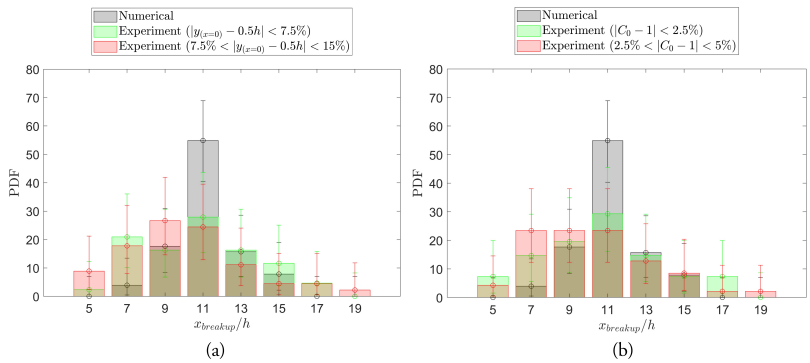

Figure 4.17: PDF of the streamwise breakup positions for the experimental drops categorized based on (a) injection point position, and (b) initial circularity. The PDF of the streamwise breakup positions for the numerical study is provided for comparison. The error bars show the 95% confidence intervals (Adopted and modified from Fig. 17 and Fig. 18 in **Paper IV**)

Therefore, as suggested by these findings, the initial state of the drop at the time of injection seems to be able to explain part of the differences observed between the numerical and experimental results.

The last hypothesis that might explain the differences of the numerical and experimental results is that the assumptions made for the interfacial tension in the numerical approach are possibly not taking into account all the physics of the breakup phenomenon. A simplistic model is used in the numerical approach concerning the dynamics of the surface-active species. In this study, the interfacial tension on the surface of the drop is assumed to be constant in time and over the surface of the drop. This implies an assumption of instant emulsifier distribution over the drop interface (Håkansson and Nilsson, 2023). This is not true in reality in two main perspectives. First, one could argue that from the time the drop detaches from the injection needle until it breaks, the emulsifier species do not have enough time to spread entirely on the drop interface. If this is true, it actually implies larger interfacial tension in the experimental drops which should lead to statistically later breakup

positions. However, the results support the opposite i.e., the experimental drops show an earlier mean breakup position compared to the DNS drops. The second argument is that drop deformation leads to spatial gradients of interfacial tensions which in turn leads to Marangoni effects (flow driving stresses). Furthermore, local differences of interfacial tension react differently to the local turbulent structures in terms of local deformations. Overall, these effects are not expected to change the results in terms of breakup positions, but they could provide an explanation in terms of minor differences in the breakup probabilities.

Despite the minor differences observed in the experimental and the numerical results, we find the combination of both of these approaches to be a promising framework. Both the experimental and numerical approaches have their own limitations. In the experiments, the camera shutter speed, frames-per-second, etc., as well as 2D representation of the 3D drops introduce limitations to the problem. In the numerical approach, the computational costs limit the turbulence levels to a medium range (higher Reynolds numbers need higher resolution which in turn increases the computational cost). While in industrial applications, high turbulence levels are typically observed. Overall, since the limitations of the two approaches do not considerably overlap, the combination of the two approaches seemed to provide a robust framework in studying the turbulent drop breakup phenomenon.

4.3.2 HIT vs. HPH

The majority of the studies on drop breakup in the literature are carried out on ideal turbulence setups e.g. homogeneous isotropic turbulence (HIT) (Håkansson and Brandt, 2022; Komrakova, 2019; Qian et al., 2006; Rivière et al., 2021; Vela-Martín and Avila, 2021, 2022). Therefore, it was interesting to compare the results of such an ideal condition with those of the industrially-relevant geometry of an emulsification device (HPH) to see the main differences and similarities.

The results were compared for the cases (called ISO and HPH from now on) for three different Weber numbers: i) $We = 96$, ii) $We = 5$, and iii) $We = 1$. As Weber number is directly related to the drop diameter (cf. Eq. 2.4), one way of interpreting the different cases is through the drop sizes they represent i.e., $We = 96$ represents the largest drops which are easier to break and $We = 1$ represents the smallest drops which are hard to break. The dissipation rate of TKE (ε) used for the calculation of the Weber number is defined as the temporally and spatially averaged value across the domain for the ISO case and the temporally and spatially (in spanwise direction) averaged value at a reference point (on the jet centerline at $x/h = 8$) for the HPH case.

To make the study of the breakup more relevant in an industrial point of view, the term "first effective breakup" was defined. This term is used to describe breakup events in which

a daughter drop is detached with a volume of at least 2% of that of the mother drop. Otherwise, the breakup is defined as "initial breakup".

Fig. 4.18 illustrates one sample drop for each Weber number and each case of ISO (a) and HPH (b) (out of 7 cases studied for each resulting in a total of 42 cases) at the instance of the first effective breakup. Similar breakup morphologies are observed for all cases. Starting with the largest Weber number ($We = 96$), the breakup morphology of both cases could be described as chaotic where the drop is deformed in many directions. At the lower Weber number $We = 5$, formation of a neck with larger portions of the drop on the two sides is observed with the breakup happening in the neck. At the lowest Weber number ($We = 1$), the dominant observation is that there is almost no tendency of the drops to breakup. Only one case out of 7 cases in the HPH drops resulted in breakup. The drops in the other cases only showed slight deformations and relaxing back to the stable spherical shape.

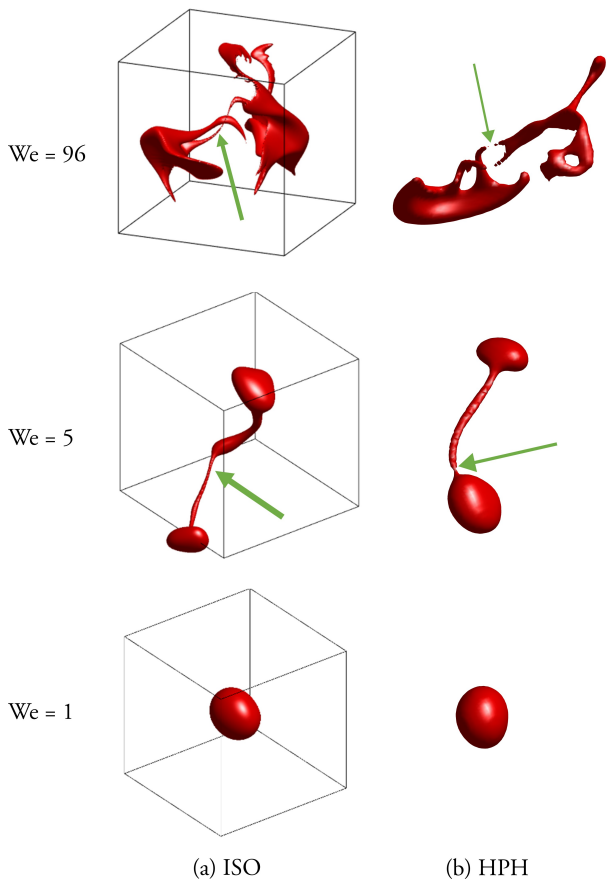

Figure 4.18: Drops at the instance of the first effective breakup at $We = 96$, $We = 5$, and $We = 1$ for (a) ISO case, and (b) HPH case.

Fig. 4.19 shows the drop total interfacial area variations with time for each case at the

different Weber numbers. A commonly observed difference between the two sets of cases is that in the ISO cases, the drops start to deform immediately from the beginning, while no deformation is observed for the HPH cases until they reach a specific time (corresponding to the positions at which the dissipative region in the shear layer is present). Also, another observation is that the values of the maximum interfacial area generally increase with the Weber number in both the ISO and the HPH cases e.g., maximum values of A/A_0 at $We = 96$ are in the ranges $[2.1 - 3.4]$ and $[2.4 - 3.3]$ for the HPH and the ISO cases, respectively, while these are $[1.5 - 2.4]$ and $[1.3 - 1.9]$ at $We = 5$.

At $We = 96$, as observed for almost all cases, an initial breakup (a detachment of less than 2% volume) occurs before reaching the first effective breakup which is another indication of the chaotic deformation of the drops at this high Weber number for both cases. The interfacial areas at which breakup happens are comparable for the two sets of cases. A difference between the two cases at this Weber number is that the area variations of the ISO cases increase monotonically with an almost constant slope (variation rate) until the first effective breakup happens. However, these variations for the HPH drops start slowly and then get faster (with some cases even relaxing again to lower interfacial area e.g., cases A and G) until the breakup happens.

At $We = 5$ for the ISO cases, there is no monotonic increase in interfacial area over time, as there were for $We = 96$. This implies that the deformations of the drops are not as intense as those at $We = 96$. Therefore, drops have more time to go through deformation and relaxation periods and finally breakup. However, there is no substantial difference between the HPH cases in terms of the breakup time implying that the shear layer position and the anisotropic characteristics of the flow field in the HPH play the decisive role on when the breakup occurs. A difference observed at this Weber number is that in the majority of the cases (except for cases C and D in the HPH), the initial and the first effective breakup coincide. This is another indication of the chaotic behavior of the drops at $We = 96$ where the explosive breakup behavior leads to very small detachments while this is not observed for lower Weber numbers.

At the lowest Weber number ($We = 1$), the behavior of the drops is more different between the ISO and HPH settings. For the ISO cases, oscillatory behavior is observed for all drops in which the interfacial area steadily increases, but no breakup occurs even after a long time ($t/\tau_\eta = 108$). On the other hand, for the drops in the HPH case, the drops go through similar deformation/relaxation periods. But, after a certain time, no further significant deformations are observed implying that the drops have passed the high-dissipation region of the shear layer and no further chance of large deformations leading to breakup exists. Only one case (E) goes through a larger relative increase of 30% in the interfacial area, and this is the only drop that breaks at this Weber number.

Table 4.2 reports a summary of the first effective breakup times (Mean $\pm$ Standard devi-

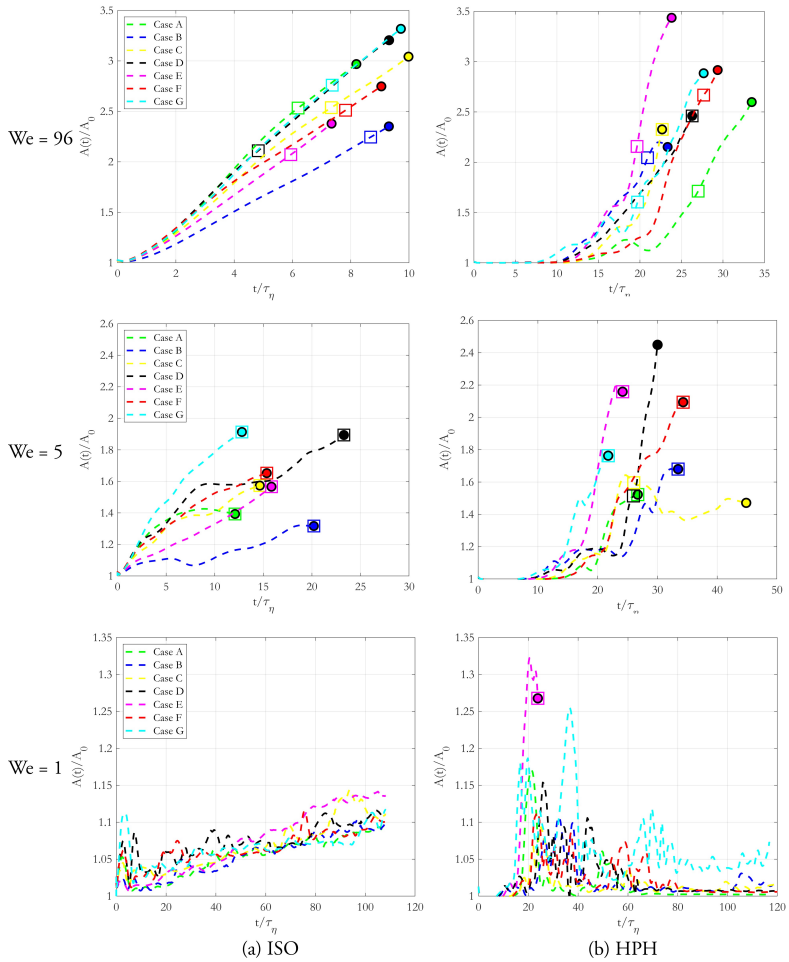

Figure 4.19: Total interfacial area variations at $We = 96$, $We = 5$, and $We = 1$ for (a) ISO cases, and (b) HPH cases. The square and circle markers show the initial and the first effective breakup positions, respectively (Adopted and modified from Figs. 8, 11, 14 in **Paper III**)

ation) for each case and Weber number. For the ISO cases, a clear trend is observed where the breakup times decrease with increasing the Weber number. This trend is also observed for individual cases starting from the same flow realizations but at different Weber numbers. However, no substantial decrease is observed in the breakup time for the HPH cases as the Weber number increases. Even for some individual cases e.g., case G, the drop breakup occurs at an earlier time for the lower Weber number $We = 5$ compared to $We = 96$. This indicates that, due to the inhomogeneity of the flow field in the HPH cases, correlations of the breakup time and the Weber number do not appear to be generally held as those in the ISO cases.

Table 4.2: The normalized first effective breakup times (t_B/τ_η) reported as (Mean $\pm$ Standard deviation) for each case and Weber number.

	$We = 1$	$We = 5$	$We = 96$
ISO	> 100	16.3 ± 4	9.5 ± 1.3
HPH	> 116 (Case E: 23.8)	30.8 ± 7.7	27.7 ± 3.9

4.4 Investigations of turbulence impact on drop breakup

By building confidence on the results of the DNS-VOF simulations by validating them through the experiments, a vast information is now available on the flow field turbulent characteristics, with the dissipation rate of TKE field being of particular interest due to its key role in Kolmogorov-Hinze drop breakup analyses framework (Walstra and Smulders, 1998) as well as suggestions by other studies in the context of drop breakup in high-pressure homogenizers (Guan et al., 2020; Maindarkar et al., 2015; Mohr, 1987; Raikar et al., 2011).

As a first step, a number of simulations were done on different Weber numbers to find the Weber number at which somewhat close percentages of both cases of drops breaking and not breaking are observed (All Weber numbers are characteristic Weber numbers based on ε value of Eq. 2.6, unless stated otherwise). This would give us a good study case to investigate why, at the same Weber number, breakup occurs in some flow realizations and not in others. Preliminary investigations over a wider range of Weber numbers indicated $We = 3$ to be a good representative of such a case where breakup events were observed for 15 out of a total of 25 drops. More details on these preliminary investigations are found in **Paper V**.

4.4.1 Breakup morphologies

One interesting observation at $We = 3$ is that for all cases where breakup occurs, the observed breakup morphology is the single-point breakup (cf. Fig 4.12) with bulb-neck deformation and breakup occurring somewhere in the neck. Fig. 4.20 illustrates the visualization of the drops with the same flow realization at the time of initial breakup (the final state of the drop for the case of $We = 1$ where no breakup is observed), but at different Weber numbers. At $We = 3$, bulb-neck breakup morphology is observed. At the slightly higher $We = 5$, still the same morphology (single point breakup) is observed but with considerable differences in the size of the portions of the bulbs formed at each side of the neck. Further increasing the Weber number leads to more chaotic breakup morphologies. At $We = 20$, the initial breakup point starts inside the sheet formed at the upper-left part of the drop and at $We = 60$, this behavior is observed in a much more pronounced fashion indicating a diffuse breakup morphology (cf. Fig. 4.10). This clearly shows the Weber number to be an important factor in determining the breakup morphology. However, the

fact that not all drops break at some Weber numbers e.g. $We = 3$, shows that other factors such as the local and instantaneous turbulent properties are also important which will be discussed later in this section.

Furthermore, a general decreasing trend is observed for the breakup times with increasing the Weber number. But, this does not happen monotonically (A decrease is observed in breakup time from $We = 3$ to $We = 5$, but an increase is observed again from $We = 5$ to $We = 10$). This is in agreement with the discussions of breakup time in HPH cases in section 4.3.2 as well as breakup morphology analyses in homogeneous isotropic turbulence (Håkansson et al., 2022b).

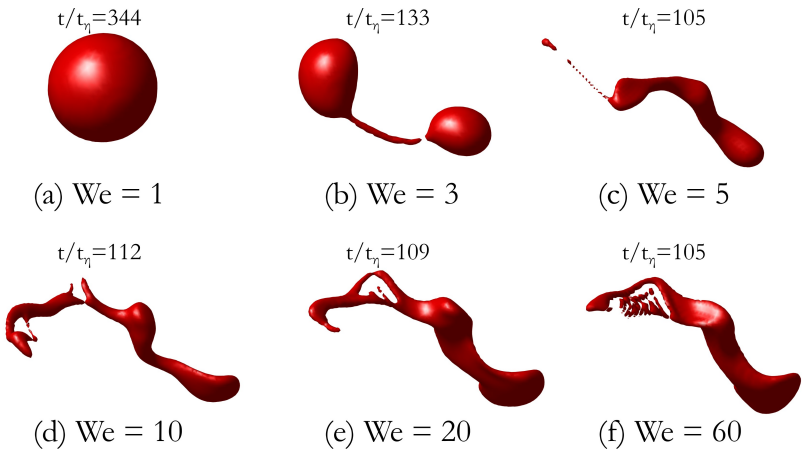

Figure 4.20: Drops visualizations at different Weber numbers at the time of initial breakup (with similar HPH settings as that of **Paper IV**). The initial breakup time normalized by the Kolmogorov time-scale t_η is presented for each case (except for $We = 1$ for which the final state of the drop and the corresponding time in the simulation is presented).

4.4.2 Critical Weber number

Finding a critical Weber number above which breakup is definite has always been of great interest in the literature on the breakup phenomenon (Duan et al., 2003; Rivière et al., 2021; Walstra and Smulders, 1998; Wierzba, 1990). In the Kolmogorov-Hinze framework, the critical Weber number is a global quantity that describes the largest surviving drop. In this study, we are investigating whether the same line of reasoning can be applied locally and instantaneously. It has been suggested (Perlekar et al., 2012) that the concept of a critical Weber number can be applied locally as an indication of when the local turbulent structures surrounding a drop are sufficiently energetic to break it.

Fig. 4.21 shows the local maximum Weber number on the surface of the drops ($We_{s_{max}}$), based on the maximum instantaneous dissipation rate of TKE on the drop interface i.e., $\varepsilon_{s_{max}}$, where drop interface is identified as the regions where 0.45 <VOF< 0.55) along

their trajectories in streamwise direction, for all flow realizations.

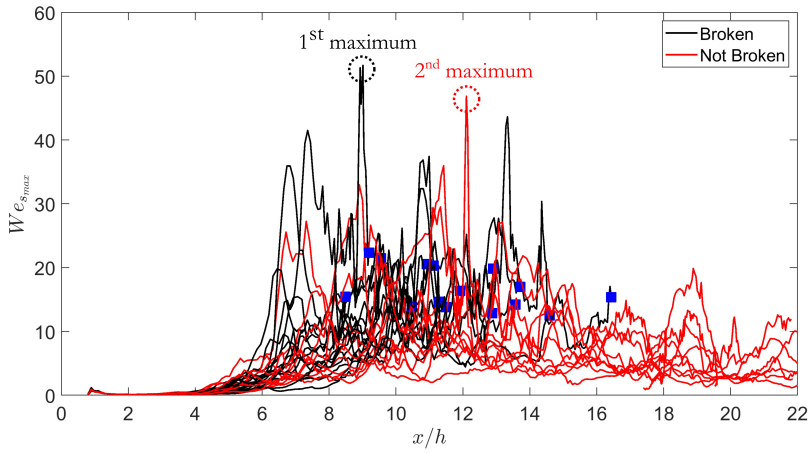

Figure 4.21: Drop interface maximum Weber number along drop trajectories in streamwise direction. Black and red curves show the drops which break and do not break, respectively. Solid blue square marks show the positions of initial breakup for the corresponding curves.

As shown in this figure, up to about $x = 4$, all drops have very low (< 1) local Weber numbers. Above this position, $We_{s_{max}}$ increases, indicating increased external stresses, leading to a number of drops breaking (breakup positions denoted by solid blue squares) and others leaving the high-Weber region ($x/h \approx 6 - 15$) without breaking. Beyond this region, no further breakup is expected as there will be no significant turbulence to interact with the drops.

An important observation in Fig. 4.21 is that no threshold (critical) value could be identified above which breakup definitely occurs. The maximum values of $We_{s_{max}}$ for the cases of breaking and not-breaking drops are 34 ± 11 and 25 ± 11 (Mean $\pm$ standard deviation), respectively, implying that the cases that do not break, experience statistically lower maximum $We_{s_{max}}$ values along their trajectories (peak values in the figure). However, further investigations of the cases breaking and not breaking show that peak values as low as $We_{s_{max}} = 22$ have led to breakup while peak values as high as $We_{s_{max}} = 47$ did not result in breakup (As seen in the figure, the second maximum value of $We_{s_{max}}$ among all drops occurs for a drop which do not break). This shows that the criterion of a critical $We_{s_{max}}$ value is not deterministic in predicting drop breakup. As suggested by Perlekar et al. (2012), high values of $We_{s_{max}}$ could be interpreted as an indication of large drop deformations, but the observations in the cases studied in this thesis work do not support a general conclusion about the existence of a critical Weber number which determines breakup events.

The result in Fig. 4.21 has been repeated by replacing $We_{s_{max}}$ with Weber numbers based on different measures of the local dissipation rate (volume-averaged and maximum ε values inside a sphere with different diameters, $1.5 - 3D_0$, surrounding the drop). However,

regardless of how the local Weber number is defined, it is unable to provide a simple deterministic or statistical criterion for predicting drop breakup.

4.4.3 Turbulence-drop interactions

The impact of the local dissipation rate of TKE field on the drop is investigated in this section. Simultaneous visualizations of both the drop interface and the local dissipation rate of TKE, ε (both through showing local values on the drop interface and using 3D iso-surfaces, as will be discussed) was the technique to show the interactions of the drop and ε local field.

Local dissipative regions and critical deformation

Fig. 4.22 shows one example of the interactions of the ε field and the drop ($We = 3$). In Fig. 4.22a, the drop interface (VOF$=0.5$ iso-surface) is visualized where the surface is colored by the local values of the dissipation rate of TKE ($\ln(\varepsilon[m^2/s^3])$). Note that at the concave region of the drop, which appears to have just occurred, the local ε is relatively high. This suggests that the local ε plays a role in controlling the local deformation. This is more clearly observed in 4.22b where $\ln(\varepsilon[m^2/s^3]) = 10.8$ (Corresponding to a local $We = 7.5$) iso-surfaces are visualized and colored by the local relative velocities of the turbulent structure (with slightly different angle of view for better visualization). This is a method of illustrating the position and size of the regions of the fluid which are expected to contribute to the drop deformation with high turbulent stress. The relative velocity at each point is calculated with respect to the velocity of the drop centroid and it is used as the color of the iso-surfaces in this figure (with negative and positive values showing the regions moving away from and towards the drop centroid, respectively). It is observed that at the concavity of the deformed drop, high ε values exist with iso-surface shapes compatible with the concave drop interface. The other observation is that the ε iso-surfaces responsible for this deformation pattern is relatively stationary with respect to the drop (low relative velocities). This is a typical behavior observed in various cases, indicating that these high-dissipative regions have sufficiently long times to interact with the drop and deform it.

Fig. 4.23 illustrates the results for a case which does not lead to breakup. The development of the drop deformation is illustrated in three different snapshots (from left to right) where the drop interface colored by the local ε (Fig. 4.23a) and $\ln(\varepsilon[m^2/s^3]) = 10$ (Corresponding to a local $We = 4.4$) iso-surfaces around the drop, colored by U_{rel}/U_g (Fig. 4.23b) are provided for each snapshot (with slightly different angles of view for better visualization). In the first snapshot, high ε values are observed. This is also confirmed by the relatively stationary high-ε iso-surfaces close to the drop interface which are aligned compatibly with the drop stretching direction. This leads to more stretching and formation of a neck in the

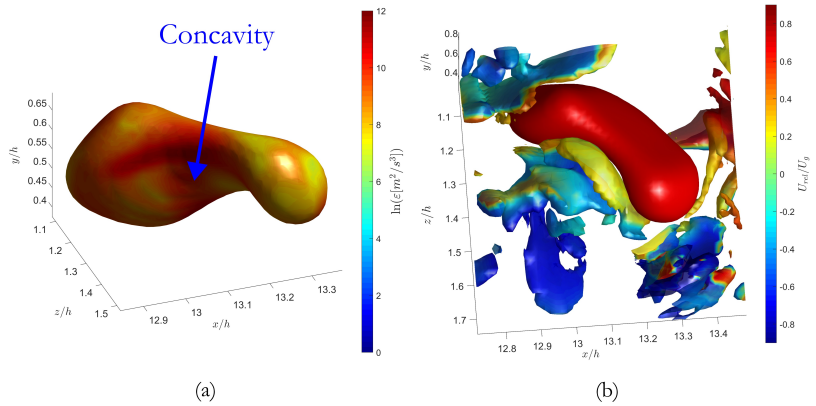

Figure 4.22: (a) drop interface (VOF= 0.5 iso-surface) colored by the local dissipation rate of TKE ($\ln(\varepsilon[m^2/s^3])$), (b) $\ln(\varepsilon[m^2/s^3]) = 10.8$ iso-surfaces around the drop, colored by the normalized local relative velocity with respect to the drop centroid (U_{rel}/U_g)

drop (in the second snapshot). However, no high-ε region is available anymore to further stretch the neck to its critically deformed state, defined as the deformation which renders the internal flow in the drop to become destabilizing (Håkansson et al., 2022a). Finally, the drop exits the high-dissipative region and relaxes back to its stable spherical shape.

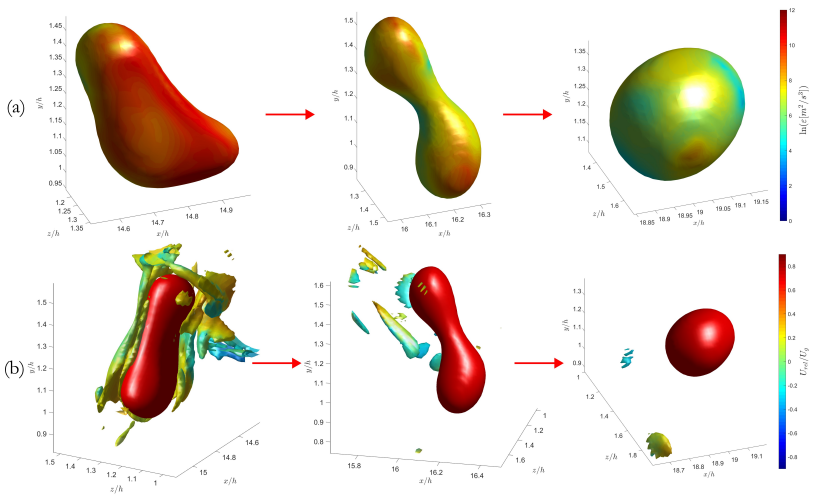

Figure 4.23: Development of the drop deformation for a case with no breakup (a) drop interface (VOF= 0.5 iso-surface) colored by the local dissipation rate of TKE ($\ln(\varepsilon[m^2/s^3])$), (b) $\ln(\varepsilon[m^2/s^3]) = 10$ iso-surfaces around the drop, colored by the normalized local relative velocity with respect to the drop centroid (U_{rel}/U_g)

Local dissipative regions and breakup behavior in the neck

Another observation from the studied cases is that the local ε values on the surface of the drop at the critically deformed state seem to provide clues about the position of the initial breakup in the neck. Two different sets of cases are observed in which high ε values are locally either: i) concentrated in one or several disconnected regions, or ii) distributed in a larger region. Fig. 4.24 shows two sample drops for case (i). In Fig. 4.24a, high ε values are observed on the left part of the neck where the breakup occurs in the next snapshot. In Fig. 4.24b, high ε values are observed on both ends of the neck while medium local ε values exist in the middle. In the next snapshot, breakup occurs at those high ε regions.

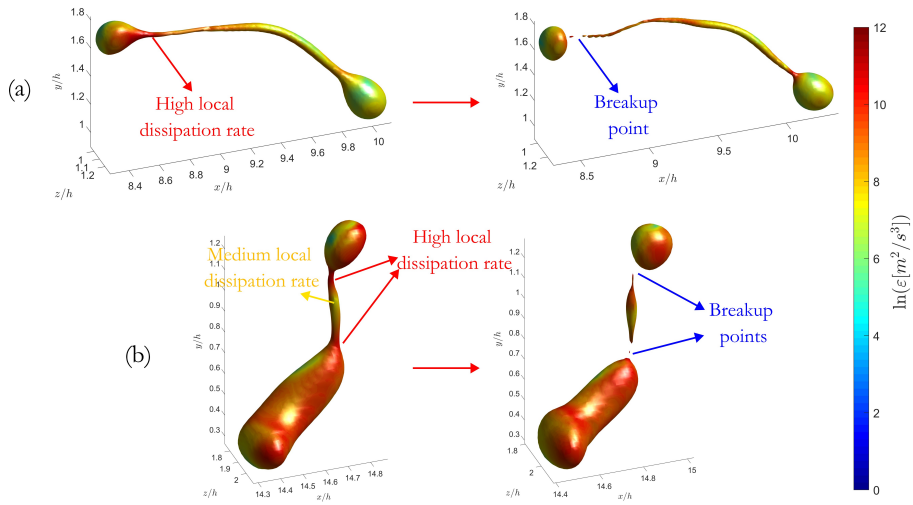

Figure 4.24: Impact of concentrated local high ε regions on the initial breakup point for two drop samples. The figures on the left show the snapshots just before the breakup where high local ε values are denoted by the red arrows. The figures on the right show the instance of initial breakup with the blue arrows pointing to the approximate positions of initial breakup

Fig. 4.25 provides two sample drops for case (ii). In both sample drops, the high ε values are observed in a larger area in the neck. In Fig. 4.25a, high ε values are found in the half of the neck area on the left, while in 4.25b, the whole neck is under high ε values. In both cases, breakup occurs not in a single point, but within the whole region where high ε was observed. How the neck breaks influences the shapes of the daughter drops and their size distribution which is still debated as discussed in the literature, mostly investigated through population balance equations (PBE). This study shows the influence of the local flow conditions in that regard. Furthermore, how the initial breakup takes place affects the developments of breakup cascade (Komrakova, 2019).

As a final remark, it should be noted that as discussed in **Paper III**, the spatial resolution of the simulations is sufficiently high for the study of the initial breakup. However, as the drop deforms to the point that the neck is thinned beyond the state of critical deformation,

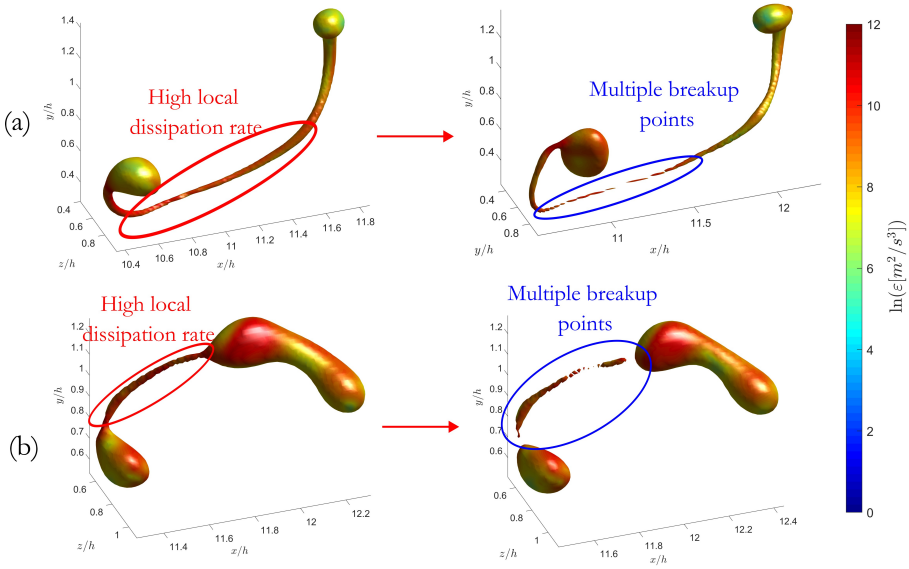

Figure 4.25: Impact of distributed local high ε regions on the initial breakup point for two drop samples. The figures on the left show the snapshots just before the breakup where high local ε values are denoted by the red ovals. The figures on the right show the instance of initial breakup with the blue ovals showing the approximate regions of initial breakup

we start to get very few grid cells across the neck. This issue could be somewhat alleviated by considerably increasing the resolution around the neck, but could not be completely resolved (As there will always be few points in the neck close to the time of breakup). However, since the initial breakup is the main interest in this study, this limitation does not compromise the results. Although, no concrete conclusions could be made regarding the exact points of breakup, further development of the drop breakup and the movements of the detached portions of the drop provide the proof regarding the occurrence of the breakup as well as its approximate position.

Chapter 5

5 Contributions, implications, and conclusions

This chapter provides a brief image regarding the contributions of this thesis work to the field of turbulent drop breakup inside high-pressure homogenizers, its relevance to the industrial applications, and its main conclusions.

5.1 Contributions

The contributions of each publication resulted from this study are summarized as follows:

- **Paper I:** Before this study, the state-of-the-art in studying the flow field inside an HPH outlet chamber geometry was using either PIV (Innings and Trägårdh, 2007; Håkansson et al., 2011; Kelemen et al., 2015a; Preiss et al., 2021) or RANS/LES CFD (Bagkeris et al., 2020; Floury et al., 2004; Håkansson et al., 2012; Kleinig and Middelberg, 1997; Taghinia et al., 2016). In this paper, a detailed description of the flow field characteristics inside an emulsification device scale-up model was achieved using direct numerical simulation (DNS) which provided flow field and turbulence properties to the smallest scales of length and time (Kolmogorov-scales) which is not achievable by any experimental or any other CFD tool. This has not been done before in any emulsification or similar devices.
- **Paper II:** Having a benchmark study (DNS), turbulence models (LES and RANS) were utilized to investigate how much of the flow field characteristics in the scale-up HPH model they can successfully predict and capture. Before this, the state-of-the-art was validating RANS CFD results with PIV measurements which could not accurately describe turbulent characteristics of the flow field, most importantly, the dissipation rate of TKE field. Therefore, no information was available regarding the accuracy of turbulence models. This was important in an industrial point of view to see to what extent the predictions of these models are close to the DNS results.

- **Paper III:** This paper compares the characteristics of the breakup phenomenon in the scale-up HPH model and in a homogeneous isotropic turbulence (HIT) condition. Before this study, numerical studies were mostly focused on ideal conditions such as HIT (Håkansson and Brandt, 2022; Håkansson et al., 2022a; Komrakova, 2019; Rivière et al., 2021; Shao et al., 2018; Vela-Martín and Avila, 2021, 2022) or shear flows (Rosti et al., 2019). However, no studies investigated more industrially relevant or application oriented flow in emulsification or similar devices. This study was an important task to investigate the similarities and differences between those ideal conditions and the flow setup in the emulsification device geometry. This provided an insight on how much these conditions are relatable and therefore, how much of the knowledge gained in the ideal conditions could be used to study the more industrially relevant setups. This will be discussed further in 5.3.

- **Paper IV:** As the first time, a powerful numerical tool i.e. DNS-VOF framework, was used to study the turbulent drop breakup phenomenon in an emulsification device model (HPH valve). Before this study, various experimental (Galinat et al., 2007; Kelemen et al., 2015b; La Forgia et al., 2021; Maaß and Kraume, 2012; Preiss et al., 2022; Solsvik and Jakobsen, 2015) and numerical studies (Håkansson and Brandt, 2022; Komrakova, 2019; Rivière et al., 2021; Shao et al., 2018; Vela-Martín and Avila, 2022) had investigated the turbulent drop breakup phenomenon. However, no study compared the results of the two approaches. Furthermore, like any numerical tool, a validation of the results was needed through experiments. The validation was performed successfully and this built credibility in using this numerical tool for studying breakup under conditions similar to those in an HPH valve outlet chamber. Moreover, this provided unprecedented information regarding the flow surrounding the drops, the most important being the dissipation rate of TKE field within Kolmogorov-scale resolution.

- **Paper V:** The interactions of the local turbulence and the drop were investigated inside the high-pressure homogenizer outlet chamber scale-up model to describe the direct impact of the local turbulent structures on the deformation behavior of the drops for the first time, in an industrially relevant geometry. Before this study, there was a lack of information on the local turbulence in such devices since most studies were either focused on idealized turbulent conditions (HIT) (Håkansson and Brandt, 2022; Karimi and Andersson, 2020; Komrakova, 2019; Qian et al., 2006; Rivière et al., 2021; Vela-Martín and Avila, 2021, 2022) or were based on experiments (Budde et al., 2002; Galinat et al., 2005; Kelemen et al., 2015b; Innings and Trägårdh, 2005; Stang et al., 2001) which did not allow for the accurate description of the local turbulent properties.

5.2 Industrial relevance

Paper I provided a clearer image of the flow and turbulence characteristics inside an HPH outlet chamber down to Kolmogorov-scales which could not have been obtained before using industrially-favored CFD tools. In addition to the resolution of the data, DNS provided a confidence in the description of the general flow behavior. **Paper II** addressed an industrially-relevant question regarding the CFD representation of the flow field in the HPH outlet chamber i.e., how close could we get to reality (DNS) using industrial CFD tools (RANS/LES). **Paper III** started looking at the drop breakup in the HPH outlet chamber and compared that to the ideal conditions more favored in the academic literature i.e., homogeneous isotropic turbulence (HIT). Understanding the similarities and differences between the two provided more clarity on how much of the vast information available in the literature regarding HIT could be used and extended to the conditions closer to real industrial application of an HPH outlet chamber. **Paper IV** provided a focused study on the drop breakup in the HPH outlet chamber. One clear deduction of this study was the impact of the drop trajectories and high-dissipation regions on the breakup position of the drops. Therefore, improved designs leading to wider high-dissipation regions or directing the drops towards these regions could be a way to improve drops breakup probabilities. Finally, in **Paper V**, further analysis of the local turbulent properties close to the drops provided more understanding of the impact of the flow on breakup which could be beneficial in designing more efficient emulsification machines.

5.3 Conclusions

In this section, we conclude by returning to the questions posed in section 1.4 and answer each through the findings of the publications of this thesis work.

- To what extent does the turbulence inside the outlet chamber differ from more idealized homogeneous isotropic turbulence as well as other types of wall jets? And how does the dissipation rate of turbulent kinetic energy (which is arguably of large importance for understanding breakup but is difficult to obtain) look?

Paper I provided the answer to this question. First, the scale-up model proved to be successfully mimicking the general flow conditions in an industrial-level high-pressure homogenizer valve. The main flow characteristics were the presence of a wall-adherent jet and the confinement of the flow leading to a recirculatory backflow above the jet. Furthermore, similarities and differences of the confined geometry of the study were compared to those of non-confined or more ideal jet flow setups. The turbulent characteristics of the flow such as the dissipation rate of TKE field was fully described and the anisotropic behavior

of the flow field was observed which is the main difference compared to the flow field in an idealized homogeneous isotropic turbulence.

- How well can the less computationally costly CFD-techniques (industry standard) such as RANS-CFD and LES describe the relevant turbulent quantities in such a confined outlet chamber jet?

In **Paper II**, the predictions of the turbulence models i.e., LES and RANS were compared to that of the validation study (DNS). The results showed that both these models were able to predict the general behavior of the time-averaged velocity fields with LES having a closer prediction to the DNS results in the regions of slow vortex structures (cf. Fig. 4.2). LES also provided a more accurate prediction of the dissipation rate of TKE values as an important parameter for drop breakup studies, both globally (Fig. 4.5 and locally (Fig. 4.6). However, the predictions of RANS in the regions relevant for drop breakup are acceptably close to those of the LES and DNS (Fig. 4.6b-c). Nevertheless, even RANS showed to be a better prediction tool than other alternatives such as empirical estimations e.g., Eq. 2.6. Overall, RANS showed to be a fast and relevant approach for the estimation of velocity and dissipation rate values. For more local accuracy of the values, one should use LES.

- What should be RANS-CFD best practice recommendations for modeling HPH outlet chamber jets?

Paper II provided a set of best practice recommendations for modeling HPH outlet chamber flow fields. The results of this paper showed that a mesh-independent axisymmetrical 2D RNG $k - \varepsilon$ model could be a good methodology in modeling the outlet chamber of an HPH valve.

- How different is the turbulent drop breakup in the cases of idealized homogeneous isotropic turbulence and a wall jet in the HPH outlet geometry?

Paper III showed that in terms of breakup morphologies, similarities were observed at the same Weber numbers (Fig. 4.18). At $We = 96$, a more chaotic morphology i.e., sheet-rupture was observed. At the mid-range $We = 5$, neck-bulb breakup morphology was more dominant. At the lowest Weber number, $We = 1$, oscillation/relaxation periods were observed with no breakup event except for a single case in the HPH case. For this single case, it is deemed that the impact of the anisotropic turbulence at the shear layer was too intense which caused the drop to critically deform to the extent that it could not relax back to the spherical shape anymore and broke up. For none of the isotropic cases, such a large deformation was observed (cf. Fig. 4.19).

In terms of breakup times, isotropic cases showed a decrease in the breakup times as the Weber number was increased. Overall, the Weber number showed to be an important parameter in both cases, considerably affecting the breakup morphology. However, the inhomogeneous anisotropic turbulence in HPH proved to add more complexity to the breakup time and position i.e., the position of the dissipative shear layer region (where the flow is highly inhomogeneous and anisotropic) is the parameter determining when the breakup events occurs in the HPH cases.

Since working with the ideal isotropic system comes with benefits in terms of convenience and computational costs, a combination of both of these methods seem to be a promising approach. Also, since a considerable amount of data exists in the literature on idealized isotropic conditions, this study showed that one could incorporate those results into the more industrially relevant turbulent fields such as emulsification devices.

- How well does the in-silico numerical drop breakup technique comply with in-vitro experimental results from high-speed visualizations?

The results of **Paper IV** showed a good agreement between the experiments and the numerical study in terms of both the breakup morphologies and breakup positions.

- Where and how does drop breakup in the HPH outlet chamber jet take place?

As the results of **Paper IV** showed, both the experiments and numerical approaches predicted the highest probability of breakup positions to be in the range $x/h = [10, 12]$. Furthermore, two main breakup morphologies were observed in both approaches: i) single breakup point (cf. Fig. 4.9, mostly represented in the form of neck-bulb deformation), and ii) diffuse breakup (cf. Fig. 4.10, mostly represented in the form of sheet-rupture deformation). Also, borderline cases with the characteristics of both morphologies are observed in both approaches (cf. Fig. 4.11). Furthermore, the average positions of the initial breakup and positions at different circularity levels agree well for both cases (cf. Fig. 4.14).

Chapter 6

6 Future outlook

In this thesis work, an HPH scale-up model with a simple (cuboidal) geometry was designed in which the flow field behavior and drop breakup phenomenon were investigated. To further understand how flow field and geometry influences breakup, it would be interesting to conduct these studies over a range of geometries. These geometries do not necessarily need to be complex, but different in terms of the position of the gap exit leading to different jet flows e.g., free jet, delayed attachment of the jet to the wall, etc. The behavior of the flow field as well as drop breakup could be then studied and compared to the geometry of the current thesis work. Furthermore, the performance of RANS and LES models could also be investigated again on these new geometries to have a more general conclusion on the performance of these industrially favored CFD tools in high-pressure homogenizer valves. Furthermore, due to more advances of computational capacities and the opportunities of using more efficient parallel programming (e.g., GPU parallelization), studies could also be carried out on more complex geometries. Furthermore, this could also be an opportunity to work with higher Reynolds numbers which is typically the case in industrial HPH valves. From a numerical point of view, higher Reynolds number leads to smaller turbulent scales and therefore a need for higher numerical grid resolution and computational capacity.

As discussed in section 5, a more physical interpretation of the interfacial tension could incorporate the underlying physics of the kinetics of the surface active agents. As recently discussed in the literature (Håkansson and Nilsson, 2023), emulsifier kinetics not only can influence the breakup time, but the breakup mechanism as well. Such a model could consider the interfacial tension as a function of time and space (on the drop interface) and therefore take into account the differences in the relevant time-scales (Innings et al., 2011; Tcholakova et al., 2004; Walstra and Smulders, 1998) e.g., deformation time-scale as well as emulsifier diffusion and adsorption time-scales. As discussed by Håkansson et al. (2022a), the differences in these time-scales lead to different scenarios. If the deformation time-scale is lower than the other two (fast drop deformation), then the emulsifier agents do not have

time to either spread or be adsorbed from the surrounding environment. Therefore, an interfacial tension gradient is created on the surface leading to positions on the drop interface to be more susceptible to critical deformation and breakup. However, if the diffusion (leading to spreading of the emulsifier on the surface) is faster than the deformation and adsorption, the interfacial tension gradient leads to a Marangoni flow from high to low emulsifier concentrations acting as a stabilizing factor which pulls the drop together, preventing further deformation and breakup. Finally, the case in which the adsorption is faster than the other two mechanisms, is theoretically similar to the ideal assumption of constant interfacial tension over time and drop interface. As a result of proper implementation of these scenarios, the probability of the drop breakup will not only depend on the position of the drop in the turbulent field, but also on the exact position on the drop interface which is under the impact of specific turbulent eddies.

In the experimental framework, improvements could be made to improve the understanding of drop deformation and breakup and therefore, providing better validation data. One obvious improvement could be the camera performance in terms of resolution, lens, shutter speed, and frame-per-second. High-resolution images enhance quantitative interpretation of the images and therefore decrease the errors. A better lens could considerably improve the depth-of-field and therefore keeping the images of entire drops sufficiently sharp to avoid misinterpretations of the drop size and deformations. One parameter of the lens which could help in this term is the focal length. Smaller lens aperture size (opening) i.e., larger f-numbers on the lens, is another parameter; however, the latter leads to less light reaching the camera sensor and therefore, darker images. To mitigate that effect, one should use a more intense light setup. Higher shutter speed on the camera helps to avoid long exposures of the drop image to the camera sensor and artificial elongations of the drop images which could be misinterpreted as drop deformation. Higher frame-per-second could increase the number of images during the critical deformation stage of the drops which is usually very fast. Furthermore, as suggested and done by Masuk et al. (2021) and Qi et al. (2022), using multiple cameras in different directions could provide information of the drop in 3D dimensions and therefore, remove the uncertainties and loss of information in the dimension normal to the 2D-imaging plane.

References

Ahlman, D., Brethouwer, G., and Johansson, A. V. (2007). Direct numerical simulation of a plane turbulent wall-jet including scalar mixing. *Physics of Fluids*, 19(6):065102.

Andersson, R. and Andersson, B. (2006a). Modeling the breakup of fluid particles in turbulent flows. *AIChE Journal*, 52(6):2031–2038.

Andersson, R. and Andersson, B. (2006b). On the breakup of fluid particles in turbulent flows. *AIChE Journal*, 52(6):2020–2030.

Ashar, M., Arlov, D., Carlsson, F., Innings, F., and Andersson, R. (2018). Single droplet breakup in a rotor-stator mixer. *Chemical Engineering Science*, 181:186–198.

Bagkeris, I., Michael, V., Prosser, R., and Kowalski, A. (2020). Large–eddy simulation in a Sonolator high–pressure homogeniser. *Chemical Engineering Science*, 215:115441.

Baldyga, J. and Podgórska, W. (1998). Drop break-up in intermittent turbulence: Maximum stable and transient sizes of drops. *The Canadian Journal of Chemical Engineering*, 76(3):456–470.

Becker, P. J., Puel, F., Dubbelboer, A., Janssen, J., and Sheibat-Othman, N. (2014). Coupled population balance–CFD simulation of droplet breakup in a high pressure homogenizer. *Computers & Chemical Engineering*, 68:140–150.

Bernardini, M., Pirozzoli, S., and Orlandi, P. (2014). Velocity statistics in turbulent channel flow up to. *Journal of Fluid Mechanics*, 742:171–191.

Billson, M., Eriksson, L.-E., and Davidson, L. (2003). Jet Noise Prediction Using Stochastic Turbulence Modeling. In *9th AIAA/CEAS Aeroacoustics Conference and Exhibit*, Hilton Head, South Carolina. American Institute of Aeronautics and Astronautics.

Budde, C., Schaffner, D., and Walzel, P. (2002). Drop Breakup in Liquid-Liquid Dispersions at an Orifice Plate Observed in a Large-Scale Model. *Chemical Engineering & Technology*, 25(12):1164–1167.

Bylund, G. (2003). Dairy Processing Handbook. Lund, Sweden: Tetra Pak Processing Systems AB.

Calabrese, R. V., Chang, T. P. K., and Dang, P. T. (1986). Drop breakup in turbulent stirred-tank contactors. Part I: Effect of dispersed-phase viscosity. *AIChE Journal*, 32(4):657–666.

Casoli, P., Vacca, A., and Berta, G. L. (2010). A numerical procedure for predicting the performance of high pressure homogenizing valves. *Simulation Modelling Practice and Theory*, 18(2):125–138.

Chin, H. B. and Han, C. D. (1979). Studies on Droplet Deformation and Breakup. I. Droplet Deformation in Extensional Flow. *Journal of Rheology*, 23(5):557–590.

Chin, H. B. and Han, C. D. (1980). Studies on Droplet Deformation and Breakup. II. Breakup of a Droplet in Nonuniform Shear Flow. *Journal of Rheology*, 24(1):1–37.

Costa, P. (2018). A FFT-based finite-difference solver for massively-parallel direct numerical simulations of turbulent flows. *Computers & Mathematics with Applications*, 76(8):1853–1862.

Davidson, L. and Billson, M. (2006). Hybrid LES-RANS using synthesized turbulent fluctuations for forcing in the interface region. *International Journal of Heat and Fluid Flow*, 27(6):1028–1042.

Davidson, L. and Peng, S.-H. (2013). Embedded Large-Eddy Simulation Using the Partially Averaged Navier–Stokes Model. *AIAA Journal*, 51(5):1066–1079.

Davies, J. (1985). Drop sizes of emulsions related to turbulent energy dissipation rates. *Chemical Engineering Science*, 40(5):839–842.

Dean, R. B. (1978). Reynolds Number Dependence of Skin Friction and Other Bulk Flow Variables in Two-Dimensional Rectangular Duct Flow. *Journal of Fluids Engineering*, 100(2):215–223.

Deo, R. C., Mi, J., and Nathan, G. J. (2008). The influence of Reynolds number on a plane jet. *Physics of Fluids*, 20(7):075108.

Duan, R.-Q., Koshizuka, S., and Oka, Y. (2003). Numerical and Theoretical Investigation of Effect of Density Ratio on the Critical Weber Number of Droplet Breakup. *Journal of Nuclear Science and Technology*, 40(7):501–508.

Dubbelboer, A., Janssen, J., Hoogland, H., Mudaliar, A., Maindarkar, S., Zondervan, E., and Meuldijk, J. (2014). Population balances combined with Computational Fluid Dynamics: A modeling approach for dispersive mixing in a high pressure homogenizer. *Chemical Engineering Science*, 117:376–388.

Eastwood, C. D., Armi, L., and Lasheras, J. C. (2004). The breakup of immiscible fluids in turbulent flows. *Journal of Fluid Mechanics*, 502:309–333.

Floury, J., Bellettre, J., Legrand, J., and Desrumaux, A. (2004). Analysis of a new type of high pressure homogeniser. A study of the flow pattern. *Chemical Engineering Science*, 59(4):843–853.

Galinat, S., Garrido Torres, L., Masbernat, O., Guiraud, P., Risso, F., Dalmazzone, C., and Noik, C. (2007). Breakup of a drop in a liquid–liquid pipe flow through an orifice. *AIChE Journal*, 53(1):56–68.

Galinat, S., Masbernat, O., Guiraud, P., Dalmazzone, C., and Noı¨k, C. (2005). Drop break-up in turbulent pipe flow downstream of a restriction. *Chemical Engineering Science*, 60(23):6511–6528.

Germano, M., Piomelli, U., Moin, P., and Cabot, W. H. (1991). A dynamic subgrid-scale eddy viscosity model. *Physics of Fluids A: Fluid Dynamics*, 3(7):1760–1765.

Gothsch, T., Richter, C., Beinert, S., Schilcher, C., Schilde, C., Büttgenbach, S., and Kwade, A. (2016). Effect of cavitation on dispersion and emulsification process in high-pressure microsystems (HPMS). *Chemical Engineering Science*, 144:239–248.

Guan, X., Yang, N., and Nigam, K. D. (2020). Prediction of Droplet Size Distribution for High Pressure Homogenizers with Heterogeneous Turbulent Dissipation Rate. *Industrial & Engineering Chemistry Research*, 59(9):4020–4032.

Hančil, V. and Rod, V. (1988). Break-up of a drop in a stirred tank. *Chemical Engineering and Processing: Process Intensification*, 23(3):189–193.

Herø, E. H., La Forgia, N., Solsvik, J., and Jakobsen, H. A. (2020). Single drop breakage in turbulent flow: Statistical data analysis. *Chemical Engineering Science: X*, 8:100082.

Hinze, J. O. (1955). Fundamentals of the hydrodynamic mechanism of splitting in dispersion processes. *AIChE Journal*, 1(3):289–295.

Håkansson, A. (2021a). The Role of Stochastic Time-Variations in Turbulent Stresses When Predicting Drop Breakup—A Review of Modelling Approaches. *Processes*, 9(11):1904.

Håkansson, A. (2021b). The Role of Stochastic Time-Variations in Turbulent Stresses When Predicting Drop Breakup—A Review of Modelling Approaches. *Processes*, 9(11):1904.

Håkansson, A., Andersson, R., Mortensen, H.-H., and Innings, F. (2017). Experimental investigations of turbulent fragmenting stresses in a rotor-stator mixer. Part 2. Probability distributions of instantaneous stresses. *Chemical Engineering Science*, 171:638–649.

Håkansson, A. and Brandt, L. (2022). Deformation and initial breakup morphology of viscous emulsion drops in isotropic homogeneous turbulence with relevance for emulsification devices. *Chemical Engineering Science*, 253:117599.

Håkansson, A., Crialesi-Esposito, M., Nilsson, L., and Brandt, L. (2022a). A criterion for when an emulsion drop undergoing turbulent deformation has reached a critically deformed state. *Colloids and Surfaces A: Physicochemical and Engineering Aspects*, 648:129213.

Håkansson, A., Fuchs, L., Innings, F., Revstedt, J., Trägårdh, C., and Bergenståhl, B. (2011). High resolution experimental measurement of turbulent flow field in a high pressure homogenizer model and its implications on turbulent drop fragmentation. *Chemical Engineering Science*, 66(8):1790–1801.

Håkansson, A., Fuchs, L., Innings, F., Revstedt, J., Trägårdh, C., and Bergenståhl, B. (2012). Experimental validation of k–ε RANS-CFD on a high-pressure homogenizer valve. *Chemical Engineering Science*, 71:264–273.

Håkansson, A., Innings, F., Trägårdh, C., and Bergenståhl, B. (2013). A high-pressure homogenization emulsification model—Improved emulsifier transport and hydrodynamic coupling. *Chemical Engineering Science*, 91:44–53.

Håkansson, A. and Nilsson, L. (2023). Emulsifier adsorption kinetics influences drop deformation and breakup in turbulent emulsification. *Soft Matter*, page 10.1039.D3SM01213A.

Håkansson, A., Olad, P., and Innings, F. (2022b). Identification and Mapping of Three Distinct Breakup Morphologies in the Turbulent Inertial Regime of Emulsification—Effect of Weber Number and Viscosity Ratio. *Processes*, 10(11):2204.

Ii, S., Sugiyama, K., Takeuchi, S., Takagi, S., Matsumoto, Y., and Xiao, F. (2012). An interface capturing method with a continuous function: The THINC method with multi-dimensional reconstruction. *Journal of Computational Physics*, 231(5):2328–2358.

Innings, F., Fuchs, L., and Trägårdh, C. (2011). Theoretical and experimental analyses of drop deformation and break-up in a scale model of a high-pressure homogenizer. *Journal of Food Engineering*, 103(1):21–28.

Innings, F. and Trägårdh, C. (2005). Visualization of the Drop Deformation and Break-Up Process in a High Pressure Homogenizer. *Chemical Engineering & Technology*, 28(8):882–891.

Innings, F. and Trägårdh, C. (2007). Analysis of the flow field in a high-pressure homogenizer. *Experimental Thermal and Fluid Science*, 32(2):345–354.

Jiang, B., Shi, Y., Lin, G., Kong, D., and Du, J. (2019). Nanoemulsion prepared by homogenizer☒The CFD model research. *Journal of Food Engineering*, 241:105–115.

Karimi, M. and Andersson, R. (2018). An exploratory study on fluid particles breakup rate models for the entire spectrum of turbulent energy. *Chemical Engineering Science*, 192:850–863.

Karimi, M. and Andersson, R. (2020). Stochastic simulation of droplet breakup in turbulence. *Chemical Engineering Journal*, 380:122502.

Kelemen, K., Crowther, F. E., Cierpka, C., Hecht, L. L., Kähler, C. J., and Schuchmann, H. P. (2015a). Investigations on the characterization of laminar and transitional flow conditions after high pressure homogenization orifices. *Microfluidics and Nanofluidics*, 18(4):599–612.

Kelemen, K., Gepperth, S., Koch, R., Bauer, H.-J., and Schuchmann, H. P. (2015b). On the visualization of droplet deformation and breakup during high-pressure homogenization. *Microfluidics and Nanofluidics*, 19(5):1139–1158.

Kelly, W. J. and Muske, K. R. (2004). Optimal operation of high-pressure homogenization for intracellular product recovery. *Bioprocess and Biosystems Engineering*, 27(1):25–37.

Kleinig, A. R. and Middelberg, A. P. (1996). The correlation of cell disruption with homogenizer valve pressure gradient determined by computational fluid dynamics. *Chemical Engineering Science*, 51(23):5103–5110.

Kleinig, A. R. and Middelberg, A. P. J. (1997). Numerical and experimental study of a homogenizer impinging jet. *AIChE Journal*, 43(4):1100–1107.

Kolmogorov, A. (1949). On the breakage of drops in a turbulent flow. *Dokl. Akad. Navk. SSSR*, 66:825–828.

Komrakova, A. E. (2019). Single drop breakup in turbulent flow. *The Canadian Journal of Chemical Engineering*, 97(10):2727–2739.

Krzeczkowski, S. A. (1980). Measurement of liquid droplet disintegration mechanisms. *International Journal of Multiphase Flow*, 6(3):227–239.

Köhler, K., Aguilar, F., Schubert, H., Hensel, A., Schubert, K., and Schuchmann, H. (2008). Design of a Microstructured System for the Homogenization of Dairy Products at High Fat Content Part II: Influence of Process Parameters. *Chemical Engineering & Technology*, 31(12):1863–1868.

La Forgia, N., Herø, E. H., and Jakobsen, H. A. (2021). High-speed image processing of fluid particle breakage in turbulent flow. *Chemical Engineering Science: X*, 12:100117.

Lemenand, T., Dupont, P., Valle, D. D., and Peerhossaini, H. (2013). Comparative efficiency of shear, elongation and turbulent droplet breakup mechanisms: Review and application. *Chemical Engineering Research and Design*, 91(12):2587–2600.

Lilly, D. K. (1992). A proposed modification of the Germano subgrid-scale closure method. *Physics of Fluids A: Fluid Dynamics*, 4(3):633–635.

Lobo, L., Svereika, A., and Nair, M. (2002). Coalescence during Emulsification. *Journal of Colloid and Interface Science*, 253(2):409–418.

Loo, C., Slatter, W., and Powell, R. (1950). A Study of the Cavitation Effect in the Homogenization of Dairy Products. *Journal of Dairy Science*, 33(10):692–702.

Maaß, S. and Kraume, M. (2012). Determination of breakage rates using single drop experiments. *Chemical Engineering Science*, 70:146–164.

Maindarkar, S. N., Hoogland, H., and Henson, M. A. (2015). Predicting the combined effects of oil and surfactant concentrations on the drop size distributions of homogenized emulsions. *Colloids and Surfaces A: Physicochemical and Engineering Aspects*, 467:18–30.

Martínez-Bazán, C., Montañés, J. L., and Lasheras, J. C. (1999). On the breakup of an air bubble injected into a fully developed turbulent flow. Part 1. Breakup frequency. *Journal of Fluid Mechanics*, 401:157–182.

Masuk, A. U. M., Salibindla, A. K. R., and Ni, R. (2021). Simultaneous measurements of deforming Hinze-scale bubbles with surrounding turbulence. *Journal of Fluid Mechanics*, 910:A21.

Mathey, F., Cokljat, D., Bertoglio, J. P., and Sergent, E. (2006). Assessment of the vortex method for Large Eddy Simulation inlet conditions. *Progress in Computational Fluid Dynamics, An International Journal*, 6(1/2/3):58.

McClements, D. J. (2016). *Food emulsions: principles, practices, and techniques*. CRC Press, Taylor & Francis Group, Boca Raton, third edition edition. OCLC: ocn907205079.

Miller, J., Rogowski, M., and Kelly, W. (2002). Using a cfd model to understand the fluid dynamics promoting *E. coli* breakage in a high□pressure homogenizer. *Biotechnology Progress*, 18(5):1060–1067.

Mohr, K.-H. (1987). High-pressure homogenization. Part I. Liquid-liquid dispersion in turbulence fields of high energy density. *Journal of Food Engineering*, 6(3):177–186.

Mutsch, B., Preiss, F. J., Dagenbach, T., Karbstein, H. P., and Kähler, C. J. (2021). Scaling of Droplet Breakup in High-Pressure Homogenizer Orifices. Part II: Visualization of the Turbulent Droplet Breakup. *ChemEngineering*, 5(2):31.

Naqavi, I. Z., Tucker, P. G., and Liu, Y. (2014). Large-eddy simulation of the interaction of wall jets with external stream. *International Journal of Heat and Fluid Flow*, 50:431–444.

Narsimhan, G. and Goel, P. (2001). Drop Coalescence during Emulsion Formation in a High-Pressure Homogenizer for Tetradecane-in-Water Emulsion Stabilized by Sodium Dodecyl Sulfate. *Journal of Colloid and Interface Science*, 238(2):420–432.

Orlanski, I. (1976). A simple boundary condition for unbounded hyperbolic flows. *Journal of Computational Physics*, 21(3):251–269.

Pang, H. and Ngaile, G. (2021). Modeling of a valve-type low-pressure homogenizer for oil-in-water emulsions. *Chemical Engineering and Processing - Process Intensification*, 160:108249.

Perlekar, P., Biferale, L., Sbragaglia, M., Srivastava, S., and Toschi, F. (2012). Droplet size distribution in homogeneous isotropic turbulence. *Physics of Fluids*, 24(6):065101.

Picano, F., Breugem, W.-P., and Brandt, L. (2015). Turbulent channel flow of dense suspensions of neutrally buoyant spheres. *Journal of Fluid Mechanics*, 764:463–487.

Pope, S. B. (2000). *Turbulent Flows*. Cambridge University Press, 1 edition.

Preiss, F. J., Hetz, M., and Karbstein, H. P. (2022). Does Cavitation Affect Droplet Breakup in High-Pressure Homogenization? Insights into Local Effects. *Chemie Ingenieur Technik*, 94(3):374–384.

Preiss, F. J., Mutsch, B., Kähler, C. J., and Karbstein, H. P. (2021). Scaling of Droplet Breakup in High-Pressure Homogenizer Orifices. Part I: Comparison of Velocity Profiles in Scaled Coaxial Orifices. *ChemEngineering*, 5(1):7.

Qi, Y., Tan, S., Corbitt, N., Urbanik, C., Salibindla, A. K. R., and Ni, R. (2022). Fragmentation in turbulence by small eddies. *Nature Communications*, 13(1):469.

Qian, D., McLaughlin, J. B., Sankaranarayanan, K., Sundaresan, S., and Kontomaris, K. (2006). Simulation of bubble breakup dynamics in homogeneous turbulence. *Chemical Engineering Communications*, 193(8):1038–1063.

Raikar, N. B., Bhatia, S. R., Malone, M. F., McClements, D. J., Almeida-Rivera, C., Bongers, P., and Henson, M. A. (2010). Prediction of emulsion drop size distributions with population balance equation models of multiple drop breakage. *Colloids and Surfaces A: Physicochemical and Engineering Aspects*, 361(1-3):96–108.

Raikar, N. B., Bhatia, S. R., Malone, M. F., McClements, D. J., and Henson, M. A. (2011). Predicting the Effect of the Homogenization Pressure on Emulsion Drop-Size Distributions. *Industrial & Engineering Chemistry Research*, 50(10):6089–6100.

Rayner, M. and Dejmek, P. (2015). *Engineering Aspects of Food Emulsification and Homogenization*. Contemporary Food Engineering. CRC Press.

Risso, F. and Fabre, J. (1998). Oscillations and breakup of a bubble immersed in a turbulent field. *Journal of Fluid Mechanics*, 372:323–355.

Rivière, A., Mostert, W., Perrard, S., and Deike, L. (2021). Sub-Hinze scale bubble production in turbulent bubble break-up. *Journal of Fluid Mechanics*, 917:A40.

Rosti, M. E. and Brandt, L. (2017). Numerical simulation of turbulent channel flow over a viscous hyper-elastic wall. *Journal of Fluid Mechanics*, 830:708–735.

Rosti, M. E., De Vita, F., and Brandt, L. (2019). Numerical simulations of emulsions in shear flows. *Acta Mechanica*, 230(2):667–682.

Schlender, M., Spengler, A., and Schuchmann, H. P. (2015). High-pressure emulsion formation in cylindrical coaxial orifices: Influence of cavitation induced pattern on oil drop size. *International Journal of Multiphase Flow*, 74:84–95.

Schlichting, H. and Gersten, K. (2000). *Boundary-Layer Theory*. Springer Berlin Heidelberg, Berlin, Heidelberg.

Shao, C., Luo, K., Yang, Y., and Fan, J. (2018). Direct numerical simulation of droplet breakup in homogeneous isotropic turbulence: The effect of the Weber number. *International Journal of Multiphase Flow*, 107:263–274.

Skartlien, R., Sollum, E., and Schumann, H. (2013). Droplet size distributions in turbulent emulsions: Breakup criteria and surfactant effects from direct numerical simulations. *The Journal of Chemical Physics*, 139(17):174901.

Solsvik, J. and Jakobsen, H. A. (2015). Single Air Bubble Breakup Experiments in Stirred Water Tank. *International Journal of Chemical Reactor Engineering*, 13(4):477–491.

Solsvik, J., Maaß, S., and Jakobsen, H. A. (2016). Definition of the Single Drop Breakup Event. *Industrial & Engineering Chemistry Research*, 55(10):2872–2882.

Stang, M., Schuchmann, H., and Schubert, H. (2001). Emulsification in High-Pressure Homogenizers. *Engineering in Life Sciences*, 1(4):151.

Steiner, H., Teppner, R., Brenn, G., Vankova, N., Tcholakova, S., and Denkov, N. (2006). Numerical simulation and experimental study of emulsification in a narrow-gap homogenizer. *Chemical Engineering Science*, 61(17):5841–5855.

Stevenson, M. J. and Chen, X. D. (1997). Visualization of the flow patterns in a high-pressure homogenizing valve using a CFD package. *Journal of Food Engineering*, 33(1-2):151–165.

Taghinia, J., Rahman, M., Tse, T. K., and Siikonen, T. (2016). CFD modeling of homogenizer valve: A comparative study. *Chemical Engineering Research and Design*, 106:327–336.

Taisne, L., Walstra, P., and Cabane, B. (1996). Transfer of Oil between Emulsion Droplets. *Journal of Colloid and Interface Science*, 184(2):378–390.

Tcholakova, S., Denkov, N. D., and Danner, T. (2004). Role of Surfactant Type and Concentration for the Mean Drop Size during Emulsification in Turbulent Flow. *Langmuir*, 20(18):7444–7458.

Tcholakova, S., Denkov, N. D., and Lips, A. (2008). Comparison of solid particles, globular proteins and surfactants as emulsifiers. *Physical Chemistry Chemical Physics*, 10(12):1608.

Trout, G. (1950). *Homogenized Milk: Review and Guide*. Memoir (Michigan State University. Agricultural Experiment Station). Michigan State College Press.

Tsukahara, T., Seki, Y., Kawamura, H., and Tochio, D. (2005). Dns of turbulent channel flow at very low reynolds numbers. In *Proceeding of Fourth International Symposium on Turbulence and Shear Flow Phenomena*, pages 935–940, Marriot Hotel, Williamsburg, Virginia. Begellhouse.

Vankova, N., Tcholakova, S., Denkov, N. D., Ivanov, I. B., Vulchev, V. D., and Danner, T. (2007). Emulsification in turbulent flow. *Journal of Colloid and Interface Science*, 312(2):363–380.

Vejražka, J., Zedníková, M., and Stanovský, P. (2018). Experiments on breakup of bubbles in a turbulent flow. *AIChE Journal*, 64(2):740–757.

Vela-Martín, A. and Avila, M. (2021). Deformation of drops by outer eddies in turbulence. *Journal of Fluid Mechanics*, 929:A38.

Vela-Martín, A. and Avila, M. (2022). Memoryless drop breakup in turbulence. *Science Advances*, 8(50):eabp9561.

Walstra, P. (1993). Principles of emulsion formation. *Chemical Engineering Science*, 48(2):333–349.

Walstra, P. and Smulders, P. E. (1998). Chapter 2. Emulsion Formation. In Binks, B. P., editor, *Modern Aspects of Emulsion Science*, pages 56–99. Royal Society of Chemistry, Cambridge.

White, F. (1999). *Fluid Mechanics*. McGraw-Hill International Editions. WCB/McGraw-Hill.

Wierzba, A. (1990). Deformation and breakup of liquid drops in a gas stream at nearly critical Weber numbers. *Experiments in Fluids*, 9(1-2):59–64.

Wiktorski, T. and Królak, A. (2020). Extended approach to sum of absolute differences method for improved identification of periods in biomedical time series. *MethodsX*, 7:101094.

Yakhot, V., Orszag, S. A., Thangam, S., Gatski, T. B., and Speziale, C. G. (1992). Development of turbulence models for shear flows by a double expansion technique. *Physics of Fluids A: Fluid Dynamics*, 4(7):1510–1520.

Zhang, J., Gao, Y., Gong, B., Li, Y., and Wu, J. (2021). Experimental investigation on single droplet deformation and breakup in a concave wall jet. *Chemical Engineering & Technology*, 44(2):238–247.

Zhou, H., Yu, X., Wang, B., Jing, S., Lan, W., and Li, S. (2021). Experimental study on drop breakup time and breakup rate with drop swarms in a stirred tank. *AIChE Journal*, 67(1).

Scientific publications

Author contributions

Co-authors are abbreviated as follows:
Peyman Olad (PO), Andreas Håkansson (AH), Fredrik Innings (FI), Luca Brandt (LB), Marco Crialesi Esposito (ME).

Paper I: A direct numerical simulation investigation of the one-phase flow in a simplified emulsification device

The candidate (PO) designed the HPH scale-up model, designed the CAD model and provided the drawings required by the workshop to manufacture the physical model. Also, PO implemented the required modifications on the DNS code e.g., the synthetic turbulence inlet condition, parallel (MPI) post-processing, etc. PO performed the simulations, post-processed the results, and wrote the first draft of the manuscript under the supervision of AH, FI, and LB. ME and LB provided the DNS code. Conceptualization was jointly done by FI and AH. Funding acquisition and resources were provided by AH. PO, AH, FI, LB, and ME were involved in the revision and editing of the manuscript.

Paper II: Towards best practice recommendations for turbulence modelling of high-pressure homogenizer outlet chambers – Numerical validation using DNS data

The candidate (PO) performed the simulations, post-processed the results, and wrote the first draft of the manuscript under the supervision of AH, FI, and LB. ME and LB provided the DNS code. Conceptualization was jointly done by FI and AH. Funding acquisition and resources were provided by AH. PO, AH, FI, LB, and ME were involved in the revision and editing of the manuscript.

Paper III: Comparison of turbulent drop breakup in an emulsification device and homogeneous isotropic turbulence: Insights from numerical experiments

The candidate (PO) performed the simulations, post-processing, and analysis of the results of the HPH cases. AH performed the simulations, post-processing, and analysis of the results of the ISO cases. PO wrote the first draft of the manuscript under the supervision of AH. ME and LB provided the DNS code. Conceptualization was jointly done by PO, FI, and AH. Funding acquisition and resources were provided by AH. PO, AH, LB, and ME were involved in the revision and editing of the manuscript.

Paper IV: Turbulent drop breakup in a simplified high-pressure homogenizer geometry: A comparison of experimental high-speed visualization and numerical experiments based on DNS and interface tracking

The candidate (PO) performed the simulations, post-processed and analyzed the results, and wrote the first draft of the manuscript under the supervision of AH. Conceptualization was jointly done by PO, FI, and AH. Funding acquisition, and resources were provided by AH. PO and AH were involved in the revision and editing of the manuscript.

Paper V: Single drop turbulent breakup in the anisotropic turbulence inside a high-pressure homogenizer scale-up model

The candidate (PO) performed the simulations, post-processed and analyzed the results, and wrote the first draft of the manuscript under the supervision of AH. Conceptualization was jointly done by PO and AH. Funding acquisition, and resources were provided by AH. PO and AH were involved in the revision and editing of the manuscript.